

STELLAR CORE COLLAPSE: NUMERICAL MODEL AND INFALL EPOCH¹

STEPHEN W. BRUENN

Florida Atlantic University, Boca Raton

Received 1984 April 30; accepted 1985 February 6

ABSTRACT

A numerical model based on hydrodynamics coupled to radiation transport of all neutrino types is developed for calculating stellar core collapse. General relativistic hydrodynamic equations for spherically symmetric systems including neutrino flow are obtained and presented in a form paralleling the adiabatic equations of May and White (1967). A multigroup, flux-limited diffusion scheme, used to evolve ν_e 's, $\bar{\nu}_e$'s, and ν_μ and ν_τ pairs independently, is derived from the neutrino Boltzmann equation. Expressions for the zeroth and first Legendre moments of all important neutrino interactions are derived from the standard model of electroweak interactions. Numerical values are obtained from these expressions (by numerical integration when necessary) during core-collapse calculations. An implicit numerical scheme for directly solving the neutrino equations, including the neutrino-electron scattering and neutrino thermal production terms, is presented. This scheme includes a consistent treatment of neutrino-matter decoupling in the neutrino transparent regimes. At the present time, the equation of state of Lamb *et al.* (1978, 1981) up to nuclear density, and that of Friedman and Pandharipande (1981) above nucleon density, are incorporated in the numerical model.

The numerical scheme referred to above is used to follow the collapse of the $1.398 M_\odot$ “iron” core of the $10 M_\odot$ stellar model evolved from the main sequence by Weaver and Woosley (1980a). A detailed description of the evolution of the model up to core turnaround is presented here. Succeeding papers will describe the further evolution of this model and the evolution of other models. A key result of this calculation is the extent of the core deleptonization during infall ($Y \sim 0.30$ near the core center to ~ 0.34 at the inner-core edge). This trapped lepton fraction at core turnaround is substantially lower than that obtained in recent calculations by others. The major factor responsible for this greater core deleptonization in comparison with other less detailed calculations is the use here of more accurate neutrino-electron scattering and transport algorithms. In comparison with the equally detailed calculations of Bowers and Wilson (1982a), the difference appears to reside in the equations of state used, particularly as regards the nuclear mass number and the abundance of free protons. Preliminary results obtained using the “Munich” equation of state (Wolff 1983) gave results very similar to the ones reported here. On the other hand, results obtained in a calculation using the Bowers and Wilson (1982a, b) equation of state were very different, but very similar to those reported by Bowers and Wilson (1982b), i.e., a considerably higher trapped lepton fraction at core turnaround.

The implication of a lower trapped electron fraction is that very extreme initial conditions will be required in order for the shock formed at core turnaround to be able to propagate outward and eject matter in a prompt manner.

Subject headings: dense matter — neutrinos — stars: collapsed — stars: interior

I. INTRODUCTION

The idea that the large increase in gravitational binding energy ($\sim 10^{53}$ ergs) that accompanies the collapse of a stellar core to a neutron star powers the ejection of the envelope in a supernova-like explosion ($\sim 10^{51}$ ergs released) originated with Baade and Zwicky (1934) and was considerably developed by Hoyle and Fowler (1960) and Fowler and Hoyle (1964). In the two decades since the last of these papers, much observational and theoretical work has made the idea that Type II supernovae arise from the core collapse of massive stars nothing if not compelling. Recent stellar evolutionary calculations of nonrotating stars massive enough to undergo nondegenerate carbon burning but not so massive that the pair instability

arises ($\sim 8 M_\odot \leq M \leq 70 M_\odot$) all show an evolution to a similar configuration consisting of a degenerate iron core and an overlying “onion skin” mantle of successively lighter elements (Arnett 1977a; Barkat 1977; Weaver, Zimmerman, and Woosley 1978; Nomoto *et al.* 1979; Sugimoto and Nomoto 1980; Weaver and Woosley 1980a, b; Woosley, Weaver, and Taam 1980; Miyaji *et al.* 1980; Sparks and Endal 1980; Weaver, Axelrod, and Woosley 1980; Nomoto 1982; Weaver, Woosley, and Fuller 1982; Nomoto 1983). (The advanced evolution of stars in the mass range $8 M_\odot \leq M \leq 10 M_\odot$ may be different in that burning stages after carbon can occur under electron degenerate conditions.) The iron core ultimately implodes as the result of a dynamical instability brought on by electron captures if the core has a very low entropy or by partial photodissociation of iron if the core has a higher entropy.

¹Supported in part by National Science Foundation grant AST-8111709.

If extensive mass loss does not take place prior to core collapse, the evolutionary calculations show the core at the onset of dynamic instability to be embedded in an extended red giant with an almost constant density of $10^{-8} \text{ g cm}^{-3}$ throughout a large mass fraction, and a radius $> 3 \times 10^{13}$ (Weaver, Zimmerman, and Woosley 1978; Weaver and Woosley 1980a, b; Sparks and Endal 1980; Woosley, Weaver, and Taam 1980). This is just the structure which appears to be required to explain the widths of Type II supernova light curves. In fact, the impulsive release of about 10^{51} ergs of energy in the interior by whatever mechanism produces an optical display in good agreement with observed Type II supernova light curves (Grasberg, Imshennik, and Nadyozhin 1971; Chevalier 1976; Arnett and Falk 1976; Falk and Arnett 1973, 1977; Arnett 1980; Weaver, Zimmerman, and Woosley 1978; Weaver and Woosley 1980a, b) and a velocity flow in good agreement with observed expansion velocities (Arnett and Falk 1976; Falk and Arnett 1977; Falk 1978). That the energy release for Type II supernovae is due to core collapse for at least some cases can be inferred from the absence of the effects of the subsequent decay of ^{56}Co from the large amount of ^{56}Ni ($\sim 0.7 M_{\odot}$) that would be manufactured if the energy release were the result of a thermonuclear explosion (Arnett 1982b). The width of the light curve in time (~ 100 days after maximum for a decrease by two e -folds) indicates a diffusive radiant energy release through a massive envelope ($\sim 8 M_{\odot}$) (Arnett 1981, 1982b). Recent modeling of the late stellar evolutionary phases of massive stars coupled with large nuclear reaction network calculations shows that the disruption of these massive stars, resulting from a sudden energy release within, can account (within a factor of 2) for the abundance of elements between oxygen and the iron peak elements (Arnett and Schramm 1973; Arnett 1978; Weaver and Woosley 1980b; Woosley and Weaver 1981, 1982).

The fundamental theoretical problem is to understand how gravitational energy released in the implosion of the core is transferred to the material outside the core sufficiently rapidly to expel it. The early numerical calculations (Colgate and White 1966; Arnett 1967; Schwartz 1967; Wilson 1971, 1974, 1976; Wilson *et al.* 1975; Bruenn 1975) explored the suggestion that neutrinos emitted by the collapsing core would deposit enough energy (Colgate and White 1966) or momentum (Schramm and Arnett 1975) in the outer layers to cause an explosion. The numerical results were inconclusive, but by the mid-1970s the theoretical expectations were changing. The realization of the importance of properly including the effects of neutrino degeneracy in the collapsing core and the discovery of weak neutral currents with the consequence of higher neutrino opacities led to the recognition that most of the neutrinos would be trapped in the collapsing core (Sato 1975a, b; Mazurek 1975, 1976; see also the review by Wheeler 1981). The possibility of mass ejection by neutrino energy or momentum deposition began to appear quite slim indeed (Bruenn, Arnett, and Schramm 1977).

A synergism of analytical and numerical work beginning in the late 1970s has led to a new collapse scenario. The basic conceptual framework is as follows: The large entropy increase required to dissociate nuclei coupled with the inability

to generate much entropy during the collapse because of neutrino trapping and the rapid establishment of β -equilibrium thereafter leads to the conclusion that the low initial entropy, s , of the core ($\sim 1 k \text{ nucleon}^{-1}$) will remain low during the collapse, and nuclei will remain largely bound (Mazurek, Lattimer, and Brown 1979; Bethe *et al.* 1979). As elaborated by Bethe *et al.* (1979) and Brown, Bethe, and Baym (1982), the existence of the ionic species as bound nuclei results in the pressure being dominated by the relativistic electrons (and also, above trapping densities, by electron-type neutrinos). The effective adiabatic index, Γ_E , is therefore close to $4/3$ during the collapse, being slightly less owing to electron captures before the establishment of β -equilibrium, and from Coulomb effects at higher densities. The collapse therefore proceeds nearly adiabatically to nuclear density before it begins to be halted by a stiffening of the equation of state. With s constant and $\Gamma_E \leq 4/3$, the generalization by Yahil and Lattimer (1982) and Yahil (1983) of the self-similar solutions for stellar collapse given by Goldreich and Weber (1980) is applicable as a description of the hydrodynamics of this phase of the collapse. According to this theory, the collapsing core divides into two self-similar collapsing regions: an approximately homologously collapsing inner core (velocity \propto radius) and an outer core collapsing supersonically at roughly half the free-fall velocity. The division between the inner and outer cores occurs at the point of minimum velocity. The mass of the inner core decreases with time, the rate of decrease being greater for smaller effective Γ , and therefore greater for larger amounts of electron capture.

The collapse is halted near nuclear density ($\rho_{\text{nuc}} \approx 2.7 \times 10^{14} \text{ g cm}^{-3}$), where nuclear degeneracy effects cause Γ_E to rise above $4/3$. Pressure signals generated in the interior owing to the stiffened equation of state converge near the edge of the inner core where the logarithmic derivative of the density is greatest, and a pressure discontinuity, i.e., shock wave, begins to form there. The shock quickly strengthens as material with a high specific kinetic energy passes through it, and begins to move outward.

This shock is vital in most currently proposed explosion mechanisms. Whether or not an explosion occurs depends on the initial strength of the shock and how much of the core lies outside the mass shell of its formation, i.e., the mass of the outer core. Brown, Bethe, and Baym (1982) have shown that the kinetic energy of the inner core is quickly transferred to the shock. By examining the binding energy of the inner core before and after this energy transfer, Yahil and Lattimer (1982) have obtained an approximate expression for the initial shock energy. According to this expression, the shock energy increases with Y_e as $(Y_e)^{10/3}$, where Y_e is the final electron abundance fraction. If the initial shock energy is too low and/or the outer core is too massive, then the expectation, confirmed by numerical results, is that the outward propagation of the shock will eventually stall. The shock will then become an accretion shock, no matter will be expelled in a prompt manner, and, unless the shock is reinvigorated at a later time, a black hole will eventually be formed. An analytical investigation of the shock energetics by Mazurek (1982) and Cooperstein, Bethe, and Brown (1984) indicates that the

major obstacle to the shock successfully propagating through the outer core and ejecting matter is the energy required to completely dissociate the nuclei passing through it. That a "successful" shock must be strong enough to dissociate nuclei completely, instead of into α -particles, for example, has also been argued by Mazurek (1982) and Burrows and Lattimer (1983), but has recently been questioned by Cooperstein, Bethe, and Brown (1984). Another obstacle presented by the outer core is the ram pressure due to its infall. Both the mass of the outer core and the ram pressure it presents to the shock increase with decreasing Γ_e and, therefore, with decreasing final Y_e . An additional impediment to the successful propagation of the shock is the electron-capture-induced pressure reduction in the region immediately behind the shock when it bursts through the neutrinosphere (Burrows and Mazurek 1982).

What emerges from all this is the critical role played by the amount of electron capture during collapse, or, equivalently, the core deleptonization. As a prime determinant of the initial shock strength and of the mass and ram pressure of the outer core, the amount of electron capture could be the most important factor in determining whether or not the shock can propagate out in a prompt manner and eject mass. Attempts to determine the decrease in Y_e analytically have been made by Bethe *et al.* (1979), Brown, Bethe, and Baym (1982), and Brown (1982), the latter two references indicating a final value for Y_e of about 0.35 for typical initial conditions. This is probably too much electron capture for an explosion to occur (cf. Burrows and Lattimer 1983), but detailed numerical calculations are needed for a more accurate determination of the change in Y_e .

A number of numerical collapse calculations of nonrotating stellar cores have recently been performed (Van Riper and Lattimer 1981; Van Riper 1982; Mazurek, Cooperstein, and Kahana 1980, 1982; Hillebrandt and Müller 1981; Bludman, Lichtenstadt, and Hayden 1982; Wilson 1980; Bowers and Wilson 1982b; Hillebrandt 1982a, b, 1983; Arnett 1982a). These have all confirmed the conceptual framework of core collapse sketched above. Again, what emerges is the critical role played by the change, ΔY_e , in the value of Y_e during the collapse, or, equivalently, the deleptonization, ΔY_l . The deleptonization is determined by the complex mix of physical processes occurring during the collapse and the characteristics of the precollapse stellar core, most particularly its entropy. Lower entropy cores suffer less deleptonization during collapse because the free proton abundance, on which the electron capture is superallowed, decreases very rapidly with decreasing entropy.

How much deleptonization occurs during collapse for a given precollapse model? A precise answer seems to require an elaborate numerical calculation. It therefore appears that a detailed numerical calculation of core collapse, with particular attention paid to computing the neutrino interactions and transport accurately, together with a detailed analysis of the results is one of the components needed for further progress in developing the relationship between core collapse and supernovae. As reviewed above, much work, both analytical and numerical, has already been done. The numerical calculations

performed so far, many of which were pioneering works, have nonetheless suffered from one or more limitations, the most important ones being (1) the treatment of neutrino transport (e.g., conduction approximations or leakage schemes); (2) in calculations employing multigroup neutrino transport, the use of a numerical scheme (e.g., Fokker-Planck or thermal relaxation schemes) to approximate neutrino-electron scattering that may not be accurate in all the important regimes encountered during core collapse; (3) the mass zoning (e.g., one-zone calculations); and (4) in several cases the equation of state.

This paper is the first in a series of papers presenting results of numerical calculations of the core collapse of massive stars. In this paper, the infall stage of the core evolution is described. In succeeding papers the core turnaround and prompt (50 ms) shock propagation, the late-time evolution of the core (0.5–1 s), and the results for alternative initial core models will be described.

The numerical model (i.e., initial model, input physics, and numerical techniques) was formulated with the intention of overcoming the above limitations, and is described in detail in the next section and in the appendices. The features of the numerical model include a realistic initial model and equation of state; general relativistic hydrodynamics; independent treatment of ν_e 's, $\bar{\nu}_e$'s, and ν_μ and ν_τ pairs; multigroup flux-limited diffusion; direct solution of the electron scattering and thermal production terms; evaluation of exact neutrino interaction expressions (by numerical integration, if necessary); and a consistent treatment of the effects of matter compression and expansion on the neutrinos, including the transparent cutoff. The attempt in this paper will be to examine carefully the deleptonization occurring during the collapse, and to make a detailed comparison of the numerical results for the collapse and shock propagation phases with the conceptual framework outlined above. A shortcoming of the numerical model is the use of a pseudoviscosity for the treatment of shock waves. This will not affect the collapse phase of the calculation, but the calculation of the shock propagation and associated neutrino radiation might be distorted. The actual shock-wave thickness is expected to be microscopic (Bruenn, Buchler, and Yueh 1978b). Precollapse stellar models in the $8\text{--}10 M_\odot$ range exhibit an enormous drop in density at the core-envelope boundary (Hillebrandt 1983 and references therein), and an accurate treatment of shock propagation in these cases might require different numerical techniques.

The plan of this paper is as follows. In § II a brief description of the numerical model will be given (a more complete account is left to the appendices); § III concerns itself with a detailed description of the core infall; and § IV gives a summary of the results. Appendix A provides a description of the multigroup flux-limited diffusion scheme and the neutrino-matter momentum and energy transfer terms. Appendix B describes the numerical techniques used for solving the diffusion equations and the change in the neutrino distributions due to matter compression and expansion. Appendix C presents derivations of the neutrino absorption, production, and scattering terms, including a derivation of the pair annihilation rates in a form suitable for use with a multigroup calculation. A brief description of the hydrody-

namics scheme is given in Appendix D, and a summary of the more important tests for the various components of the computer code is given in Appendix E.

II. THE NUMERICAL MODEL

a) Equation of State

One of the most important ingredients in a numerical study of gravitational collapse is the equation of state. Accurate values of μ_p and $\mu_n - \mu_p$ are needed to determine, respectively, the free proton abundance ($\propto e^{\beta\mu_p}$), and therefore the rate of electron capture on free protons, and the binding of protons to nuclei and therefore the rate of electron capture on nuclei. A realistic inclusion of nuclear partition functions is necessary to determine more accurately the temperature during collapse, which, in turn, sensitively affects the free proton abundance. Accurate values of the nuclear dissociation energy are needed to follow the propagation of the shock. Finally, accurate values of the adiabatic index $\Gamma_1 = (\partial \ln p / \partial \ln \rho)_s$ are needed because of the critical role played by its deviation from the critical value for neutral stability in determining the mass of the inner core and, therefore, the initial energy of the shock and the distance from the center of its formation.

The equation of state used here consisted of a table in (ρ, T, Y_e) -space with 5 entries per decade in density ρ , 20 per decade in temperature T , and steps of 0.05 in the electron fraction Y_e . At each entry point the following quantities were stored: the pressure, the total energy per baryon, the entropy per baryon, and the derivatives of these quantities with respect to ρ , T , and Y_e ; the chemical potentials μ_n , μ_p , and μ_e ; the mass fractions X_p , X_n , and X_A (and by inference X_α); and the values of A and Z for the typical heavy nucleus. At any given point in (ρ, T, Y_e) -space the above quantities were evaluated by logarithmic interpolation between the eight nearest table entries. In the case of one or more negative entries for a given quantity, an appropriate positive constant was added to each of the entries, and then subtracted from the interpolation.

The table entries between 6.65×10^7 and 2.65×10^{14} g cm $^{-3}$ were taken from the results of the finite-temperature liquid drop model of Lamb *et al.* (1978, 1981; see also the review by Lattimer 1981). The components in the model consist of free (outside) neutrons and protons, ${}^4\text{He}$, a typical heavy nucleus, and a uniform distribution of relativistic electrons. The nuclear energy includes terms for bulk, surface, Coulomb (including lattice effects), and translational energies. The interactions among the nucleons (both inside and outside the nucleus) were obtained from a temperature-independent Skyrme interaction, temperature-dependent effects being implicitly incorporated through the Fermi distribution of interacting nucleons.

Above the density $\rho = 2.65 \times 10^{14}$ g cm $^{-3}$, the pressure and energies in the table were taken from the hot nuclear equation of state of Friedman and Pandharipande (1981), scaled so that P and E at $\rho = 2.65 \times 10^{14}$ g cm $^{-3}$ were continuous. Above nuclear density this equation of state is characterized by a value between 2.4 and 3.2 for the adiabatic index Γ_1 .

One of the ways in which the self-consistency of the numerical calculation was checked was to monitor the total

gravitational energy plus the total energy of the neutrinos leaving the computational grid during the calculation (see Appendix E). In order to avoid potential inconsistencies in the energy bookkeeping resulting from the different equation of state used above 2.65×10^{14} g cm $^{-3}$, the local matter energy above this density was computed by integrating the work done on the matter.

The thermodynamic consistency of the equation of state tables was checked by computing from them a variety of quantities thermodynamically related to each other.

b) Neutrino Interactions

The neutrino interactions included in the numerical model are listed in Table 1, together with the section in Appendix C where the corresponding rates and their first two Legendre moments are derived. The "standard theory" of electroweak interactions as proposed by Weinberg (1967, 1972) and Salam (1969) was used in the calculation of these rates. The Weinberg angle has been given the value $\sin^2 \theta_W = 0.23$ (Hung and Sakurai 1981) for the numerical calculations. A brief description of these rates is given here. (In Table 1 and in the following discussion, an unsubscripted ν will denote a neutrino or antineutrino of any type.)

In the derivation of the rates for processes 1–5 (i.e., ν_e absorption on neutrons and nuclei, $\bar{\nu}_e$ absorption on protons, ν scattering on nucleons and nuclei) the simplifying assumptions were made that nuclear recoil and the effect of nucleon or nuclear thermal motions could be neglected, although nucleon phase-space restrictions were included for processes 1, 2, and 4 (see Fig. 34). Yueh and Buchler (1976b) have included recoil and thermal motions of the nucleons and nuclei in the calculation of these rates, but their evaluation requires numerical integration. Furthermore, inclusion of nuclear recoil in neutrino-nucleon or neutrino-nucleus scattering would result in the scattering being slightly nonconservative. This would greatly complicate the numerical treatment of these processes in a multienergy zone calculation, requiring a Fokker-Planck algorithm. To justify the neglect of nuclear thermal motions and recoil, we note first that Yueh and Buchler (1976b) have compared their general rates with the simplified rates and found the two to be in excellent agreement except under conditions of extremely high electron

TABLE 1
NEUTRINO INTERACTIONS INCLUDED IN THE NUMERICAL MODEL

Neutrino Interaction	Rate Derivation (Appendix C)
1. $\nu_e + n \rightleftharpoons e + p$	§ I
2. $\bar{\nu}_e + p \rightleftharpoons e^+ + n$	§ II
3. $\nu_e + A \rightleftharpoons e + A'$	§ III
4. $\nu + N \rightleftharpoons \nu + N$	§ IV
5. $\nu + A \rightleftharpoons \nu + A$	§ V
6. $\nu + e \rightleftharpoons \nu + e$	§ VI
7. $e + e^+ \rightleftharpoons \nu + \bar{\nu}$	§ VII

NOTE.—Particles are represented as follows: n = free neutrons, p = free protons, N = free neutrons or protons, A = nuclei, ν_e = electron-type neutrinos, ν = any type of neutrino, $\bar{\nu}$ = antiparticle of particle ν , e = electrons, e^+ = positrons.

degeneracy ($\mu_e/kT > 10^3$), where the deviation was as much as a factor of 2. These extremes in electron degeneracy are not encountered in typical core collapse trajectories, where μ_e/kT is typically of the order of 10. Second, a study using Monte Carlo techniques of the neutrino thermalization by the slightly nonconservative scattering of neutrinos on nucleons and nuclei (Tubbs 1979) has shown that thermalization by these processes is unimportant in comparison with neutrino-electron scattering (NES) except at very high densities ($\rho > 4 \times 10^{12} \text{ g cm}^{-3}$). The results presented in § III indicate, however, that by the time the matter has been compressed to densities $4 \times 10^{12} \text{ g cm}^{-3}$ the neutrinos have already become nearly equilibrated with the matter by NES.

For the case of processes 6 and 7 (NES and the pair annihilation process), expressions for the zeroth and first moments of the scattering functions for NES and of the absorption and production functions for the pair annihilation process were obtained assuming only that the electrons are highly relativistic.

A summary of the neutrino interaction rates used in the core-collapse calculation is as follows:

Interaction 1: $\nu_e + n \rightleftharpoons e + p$.—Nucleon recoil and thermal motions were neglected; the phase-space restrictions of all final particles were included. The ν_e absorptivity and emissivity are given by equations (C13) and (C15), respectively.

Interaction 2: $\bar{\nu}_e + p \rightleftharpoons e^+ + n$.—Same restrictions as for interaction 1. The $\bar{\nu}_e$ absorptivity and emissivity are given by equations (C19) and (C20), respectively.

Interaction 3: $\nu_e + A \rightleftharpoons e + A'$.—The Fuller, Fowler, and Newman (1982) nuclear-spin-summed matrix element estimate for the $1f_{7/2} \rightarrow 1f_{5/2}$ Gamow-Teller (GT) resonance was used in the computation of this rate. Complete blocking was assumed if $N > 40$ (Fuller 1982). This should underestimate the amount of electron capture on heavy nuclei during collapse because of the neglect of first-forbidden capture for $N > 40$. The daughter nucleus was assumed to be formed at an excitation energy of 3 MeV for any nucleus (Bethe *et al.* 1979; Fuller, Fowler, and Newman 1982). Nuclear recoil and thermal motions were neglected. The ν_e absorptivity and emissivity are given by equations (C29) and (C27), respectively.

Interaction 4: $\nu + N \rightleftharpoons \bar{\nu} + N$ (where $N =$ neutron or proton).—Nucleon recoil and thermal motions were neglected, but the phase-space restrictions of all final particles were included. The process is therefore assumed to be exactly conservative, and terms bilinear in the neutrino occupation distribution cancel. The neutron axial vector form factor was included, increasing the ν -neutron scattering rate by about 40% over that of other published rates, and making it anisotropic. The zeroth and first moments of the scattering functions are given by equations (C38) and (C39), respectively.

Interaction 5: $\nu + A \rightleftharpoons \bar{\nu} + A$.—Nuclear recoil and thermal motions were neglected. Both isoscalar and isovector coupling to nuclei in the Fermi mode were included. The zeroth and first moments of the scattering functions are given by equations (C44) and (C45), respectively.

Interaction 6: $\nu + e \rightleftharpoons \bar{\nu} + e$.—The scattering functions were computed assuming only that the electrons are extremely relativistic, and the zeroth and first moments of the scattering functions were obtained. Each moment $\Phi_{I,\text{NES}}^{\{p\}}$ is given by an

expression of the form

$$\Phi_{I,\text{NES}}^{\{in\}} = \alpha_1^2 h_I^{\{in\}}(\omega, \omega') + \alpha_2^2 h_I^{\{in\}}(\omega, \omega') \quad (2.1)$$

(see eq. [C50]), where α_1 and α_2 are respectively $C_V + C_A$ and $C_V - C_A$ for the ν_e 's, and $C_V - C_A$ and $C_V + C_A$ for the $\bar{\nu}_e$'s. The antiparticles of the ν_μ 's and ν_τ 's are not treated separately from the ν_μ 's and ν_τ 's themselves, so a particle-antiparticle average of α_1^2 and α_2^2 was used in this case, which leads to a value of $(C_V^2 + C_A^2 - 2C_V - 2C_A + 2)^{1/2}$ for both α_1 and α_2 . The terms $h_I^{\{in\}}$ and $h_I^{\{in\}}$ each involve an integration of the electron energy over the interval $\max(0, \omega' - \omega)$ to ∞ , where ω and ω' are the initial and final neutrino energies, respectively. For a given initial and final neutrino energy, each term was obtained as follows:

1. A 4-point Gauss-Legendre integration from $\omega' - \omega$ to $\mu_e + \omega' - \omega$, and an 8-point Gauss-Laguerre integration from $\mu_e + \omega' - \omega$ to ∞ if $\omega' > \omega$, $\mu_e > 0$.

2. A 4-point Gauss-Legendre integration from 0 to μ_e , and an 8-point Gauss-Laguerre integration from μ_e to ∞ if $\omega > \omega'$, $\mu_e > 0$.

The case in which $\mu_e < 0$ is never encountered. The zeroth and first moments of the scattering functions are given by equation (C50).

Interaction 7: $e + ^+ e \rightleftharpoons \nu + \bar{\nu}$.—The absorption and production functions were computed assuming only that the electrons are extremely relativistic, and the zeroth and first moments of the absorption and production functions were obtained. As in the case of neutrino-electron scattering, each moment $\Phi_{I,\text{TP}}^{\{p\}}$ (the subscript TP denotes thermal production) is given by an expression of the form

$$\Phi_{I,\text{TP}}^{\{p\}} = \alpha_1^2 j_I^{\{p\}}(\omega, \omega') + \alpha_2^2 j_I^{\{p\}}(\omega, \omega') \quad (2.2)$$

(see eqs. [C62] and [C63]), where α_1 and α_2 have the same values for ν_e 's, $\bar{\nu}_e$'s, and ν_μ and ν_τ pairs, respectively, as specified above for neutrino-electron scattering. The terms $j_I^{\{p\}}$ and $j_I^{\{p\}}$ each involve an integration of the electron energy over the interval 0 to $\omega + \omega'$, where ω and ω' are the energies of the neutrino and antineutrino, respectively. For given neutrino and antineutrino energies, each term was evaluated by a 4-point Gauss-Legendre integration over each of the three intervals $0 < E_e < \omega$, $\omega < E_e < \omega'$, $\omega' < E_e < \omega + \omega'$, or the intervals with $\omega \rightleftharpoons \omega'$ if $\omega > \omega'$, provided that the value of μ_e did not lie in any of these intervals. Otherwise, the interval containing μ_e was integrated by a 4-point Gauss-Legendre integration from the beginning of the interval to μ_e , and by another from μ_e to the end of the interval. The zeroth and first moments of the absorption and production functions are given by equations (C66)–(C74).

c) Neutrino Transport

Neutrino transport is another very important component of a core-collapse calculation, since it determines the amount of deleptonization that occurs during the collapse. An increase in the deleptonization during collapse results in an increase in

the amount of electron capture and a greater deviation of the effective adiabatic index, $\Gamma_E = (\ln p / \ln \rho)_{\text{comoving}}$, below the adiabatic index Γ_1 . It is the effective adiabatic index that directly characterizes the hydrodynamics during infall. Greater deleptonization therefore reduces the size of the inner core, decreases the initial strength of the shock, and increases the amount of matter and the corresponding ram pressure through which the shock must propagate.

In the calculations described here the neutrinos were transported by means of a multigroup flux-limited diffusion approximation (MGFLDA) derived from the neutrino Boltzmann equation. The details of the derivation of this scheme and the numerical method of its solution are presented in Appendices A and B, respectively. Electron-type neutrinos (ν_e 's), electron-type antineutrinos ($\bar{\nu}_e$'s), and muon and tau-type neutrino pairs (ν_τ 's) (collectively referred to as thermal neutrinos) were transported independently. For each of these three neutrino fields, 10 energy zones were used, increasing in geometric steps from 4 to 220 MeV.

In most cases, the neutrino mean free paths vary inversely with the square of the neutrino energy. The rate of neutrino transport is therefore a sensitive function of the neutrino energy distribution in the important semitransparent regime which lies between 10^{11} and 10^{12} g cm $^{-3}$. Since neutrino-electron scattering (NES) is the most effective neutrino thermalizer in this density range, the numerical treatment of NES must be accurate. To accomplish this, the NES source terms were included directly in the MGFLDA. These terms strongly couple all neutrino energy zones at any given mass zone, and considerations of numerical stability therefore require a much less efficient numerical procedure for their solution than the Fokker-Planck or thermal relaxation schemes that have traditionally been used with multienergy zone calculations. Although it is inefficient, the method of numerically computing NES used here gives results that compare well with the Monte Carlo simulations of NES by Tubbs *et al.* (1980). The comparisons are given in Appendix E.

The production of all neutrino types by the pair annihilation process is another process that must be handled accurately, because it is the dominant source of neutrinos in the shock wave formed as a result of the core bounce. As with NES, the source terms for this process were therefore included directly in the MGFLDA. These terms couple the energy zones of a given neutrino field with those of the corresponding antineutrino field for any given mass zone, and appropriate precautions must be taken in their numerical solution to avoid instabilities. The details of the numerical procedure for solution are described in Appendix B.

To derive the MGFLDA, the first two moments of the neutrino Boltzmann transport equation (BTE), written to order v/c in the fluid frame, are obtained, and the time derivative of the first moment of the neutrino occupation distribution is set to zero to obtain a diffusion equation. The incorporation of an appropriate flux limiter extends the applicability of this diffusion equation to neutrino-transparent regimes. The velocity terms result in a neutrino-matter coupling that makes the neutrinos behave like a $\Gamma_1 = 4/3$ gas under matter compression or expansion. This neutrino-matter coupling, arising only from the low-order moments of the BTE, is incorrect in the neutrino-transparent regime, just as is the diffusion equation

itself without the flux limiter. The correct procedure for decoupling the neutrinos from the matter in the neutrino-transparent regime is discovered by demanding equality in magnitude between the work done by the compressing or expanding matter on the neutrinos and the work done by the neutrinos on the matter. Appendix A gives the details of the analysis. Appendix B describes the numerical scheme devised to compute the change in the neutrino occupation distribution under matter compression or expansion. It correctly satisfies neutrino number conservation, the $\Gamma_1 = 4/3$ neutrino energy behavior, the Pauli exclusion principle, and the neutrino-matter decoupling in neutrino-transparent regimes.

d) Hydrodynamics

An explicit, general-relativistic (GR) scheme was used to compute the hydrodynamics of the core. Measures of GR effects, such as $P/\rho c^2$ and R_S/R (R_S is the Schwarzschild radius), tend to be small during the stages of core collapse considered here. At core bounce for our standard model, as an example, $P/\rho c^2$ and R_S/R had maximum values, respectively, of 0.044 at the center and 0.15 at a Lagrangian point enclosing a rest mass of about $0.5 M_\odot$. Despite the smallness of these measures of GR effects, they should not be neglected, since the hydrodynamics can be sensitively influenced by them. To be more specific, the critical adiabatic index for a relativistic polytrope is not $4/3$ but $4/3 + 2.78P/\rho c^2$, and the departure of a core from neutral stability should be measured by the deviation of the actual "adiabatic" exponent from the critical adiabatic exponent given by the latter expression. Including GR effects, therefore, should influence the hydrodynamics in essentially the same way as a process which lowers the effective adiabatic exponent Γ_E by a few percent. The self-similar solutions for hydrodynamic collapse (Yahil and Lattimer 1982; Yahil 1983) show that the effect on the outcome of the hydrodynamics of lowering Γ_E by a few percent is not negligible.

Some details of the GR hydrodynamic scheme used here are given in Appendix D. The basic equations are similar to those given by May and White (1967) except for the inclusion here of terms arising from the off-diagonal elements of the stress-energy tensor, due to neutrino transport. These additional terms, however, are small during all stages of the collapse considered here. The initial model consisted of 48 mass zones. Rezoning was carried out after core bounce in order to maintain at least five mass shells per decade in density (except across the shock front). Some rezoning of the inner core was also carried out at this time as well. Rezoning and rezoning were accomplished in a way that conserved the total gravitational mass of the core.

e) Initial Model

Most of the core-collapse calculations described here began with the $1.385 M_\odot$ "Fe"-core of a $10 M_\odot$ stellar model that had been evolved from the main sequence to the onset of core collapse by Weaver and Woosley (1980a). The configuration and composition of this core at $t = 0$, which is the time arbitrarily chosen for the beginning of our core-collapse calcu-

lations, are shown in Figures 1 and 2, respectively. Because the model was already collapsing, nothing was done artificially to induce the collapse. A silicon shell enclosed the $1.385 M_{\odot}$ of iron peak elements, and a few zones of this silicon shell were included so that the outer boundary condition would not significantly affect the hydrodynamics of the core.

Several problems arose with our use of the Weaver-Woosley model. Because our equation of state was different from that used by Weaver and Woosley, their data were not entirely consistent with it, and some slight adjustments of the data were required. The densities, pressures, velocities, electron fractions, and rest masses were taken directly from the data.

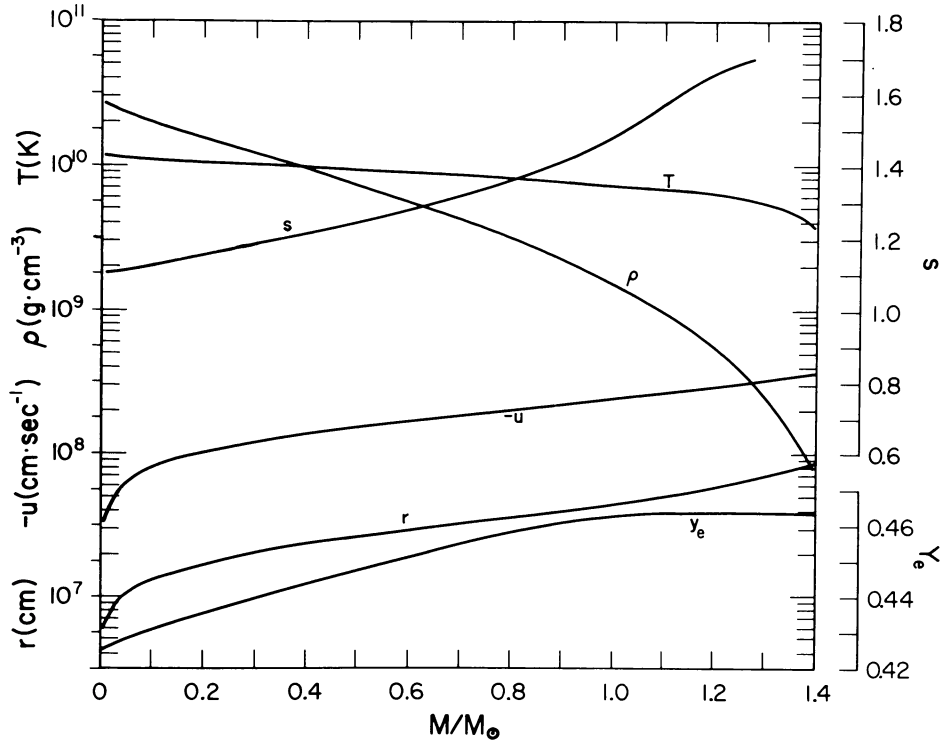


FIG. 1.—The initial (immediate precollapse) configuration of the standard model. Shown as a function of the enclosed rest mass are (left ordinate) the radius r (i.e., circumference/ 2π), the velocity u , the density ρ , the temperature T , and (right ordinate) the electron fraction Y_e , and the entropy per baryon s divided by the Boltzmann constant.

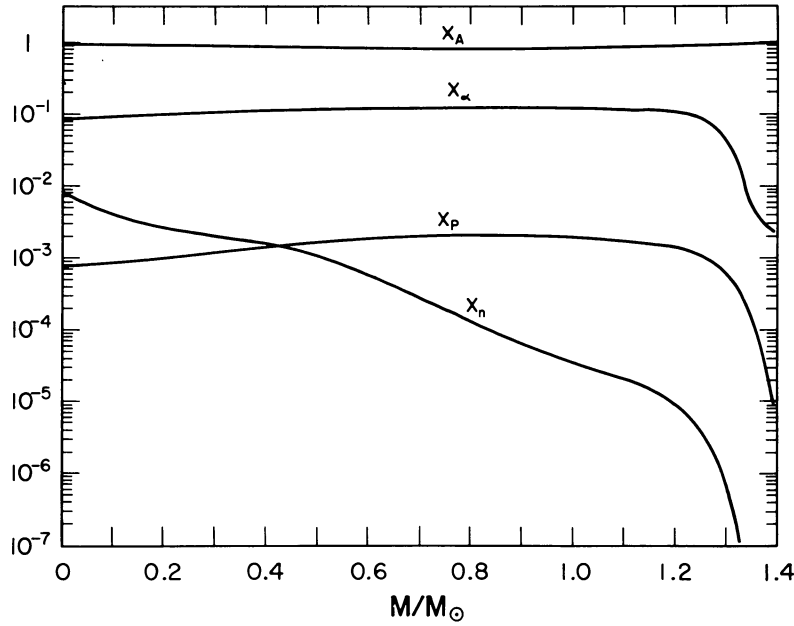


FIG. 2.—The initial (immediate precollapse) composition of the standard model. Shown as a function of the enclosed rest mass are the mass fractions of free neutrons (X_n), free protons (X_p), α -particles (X_{α}), and heavy nuclei (X_A).

The temperatures were then chosen by requiring equality between the pressure data and the pressures computed with our equation of state. The resultant temperature changes were never more than several percent. Generally, the temperatures of the inner mass zones had to be slightly increased and those of the outer zones slightly reduced.

Another problem concerned the difference between the GR equation of motion used here and the Newtonian version used by Weaver and Woosley. The Newtonian gravitational and pressure force imbalance of the Weaver-Woosley model was only about 1% at the center, and increased to about 13% at the outer part of the core. In order to avoid the possibility of distorting the subsequent hydrodynamics by introducing significantly greater gravitational and pressure force imbalances at the onset of our calculations through our use of the GR equations of motion, use was made of the dependence of the GR equations on the internal energy. By the addition of 3.4 MeV baryon⁻¹ to the internal energy, the gravitational and pressure force imbalance of the Weaver-Woosley model given by our GR equation of motion came within 10% of the Newtonian values. (It would have been possible to make them equal at each mass zone by adding a different constant to the internal energy at each of these zones.) Because the effect of electron captures is to depress the effective adiabatic index well below the critical value for neutral stability in the subsequent evolution of the core, the gravitational and pressure force imbalance will quickly become large, and the small discontinuity in the acceleration at $t = 0$ due to the switch from Newtonian to GR equations of motion should have a negligible effect.

The core-collapse calculation beginning with the above Weaver-Woosley model and carried out with the full complement of input physics described in the preceding sections will be referred to as the "standard model" (SM). The model was

TABLE 2
MODELS COMPUTED

Model	Description
SM ("standard model").....	core of the $10 M_{\odot}$ precollapse model of Weaver and Woosley 1980a evolved with the full complement of input physics described in § II
NES.....	same as model SM, but without electron capture on heavy nuclei
A	same as model SM, but without neutrino-electron scattering
NP	same as model SM, but without electron capture on heavy nuclei and neutrino-electron scattering
NT	same as model SM, but with neutrino transport turned off at densities above $5 \times 10^{11} \text{ g cm}^{-3}$
AD.....	same initial configuration as model SM, but evolved with all neutrino interaction rates set to zero, i.e., evolved adiabatically

TABLE 3
INFALL STAGES OF THE STANDARD MODEL

Infall Stage	Central Density (g cm^{-3})	Elapsed Time (ms)
0	2.751×10^{10}	0
1	4.857×10^{10}	15.7
2	1.235×10^{11}	27.7
3	3.286×10^{11}	35.3
4	9.022×10^{11}	39.54
5	2.458×10^{12}	41.75
6	6.643×10^{12}	43.05
7	1.787×10^{13}	43.84
8	4.904×10^{13}	44.32
9	1.343×10^{14}	44.60
10	2.445×10^{14}	44.72
11	3.031×10^{14}	44.81
12	3.648×10^{14}	44.88

computed until all but the last few mass zones passed through the core bounce shock, a total of 7200 cycles. Other models were computed with variations either of the input physics or of the initial conditions in order to delineate the role of some of the important physical processes. A list of the models is given in Table 2.

This paper is concerned with the evolution of the model up to core bounce, which occurred approximately at cycle 1600. Throughout the text it will be convenient to refer to the configuration of the standard model, and those of the other models as well, at various stages of the infall. To facilitate this, Table 3 gives some data for selected stages of the infall of the standard model. A given stage of the infall will hereafter be referred to by the stage number given in this table.

III. INFALL

a) Composition

The composition of the standard model at four different times during infall is shown plotted against density in Figure 3. The heavy nuclei clearly dominate the composition during infall, their mass fraction never falling below 0.7 in any part of the core below nuclear density. The changes in the magnitudes of the mean values of Z and A of the heavy nuclei are governed mainly by the reduction of the net Coulomb energy with increasing density as a result of lattice effects, and the decrease of Y_e because of electron captures with increasing density (Fig. 4). The result of the former is the growth of both Z and A with density, while the latter results in the nuclei becoming more neutron-rich. At a certain density, which will be denoted by ρ_{cutoff} , the $1f_{5/2}$ neutron shell becomes filled and electron capture on nuclei is no longer an allowed process (Fuller, Fowler, and Newman 1982). Because the initial entropy of the standard model increases with decreasing density (Fig. 4), the entropy at a given density during the collapse increases as matter with initially higher entropy compresses to that density. The increase of the entropy with time at a given density during the collapse causes the mean Z and A and the mean mass fraction of the heavy nuclei to decrease with time at that density, and the mass fractions of the light particles (protons, neutrons, and α -particles) to increase with time. One consequence of this is that ρ_{cutoff} increases with time from

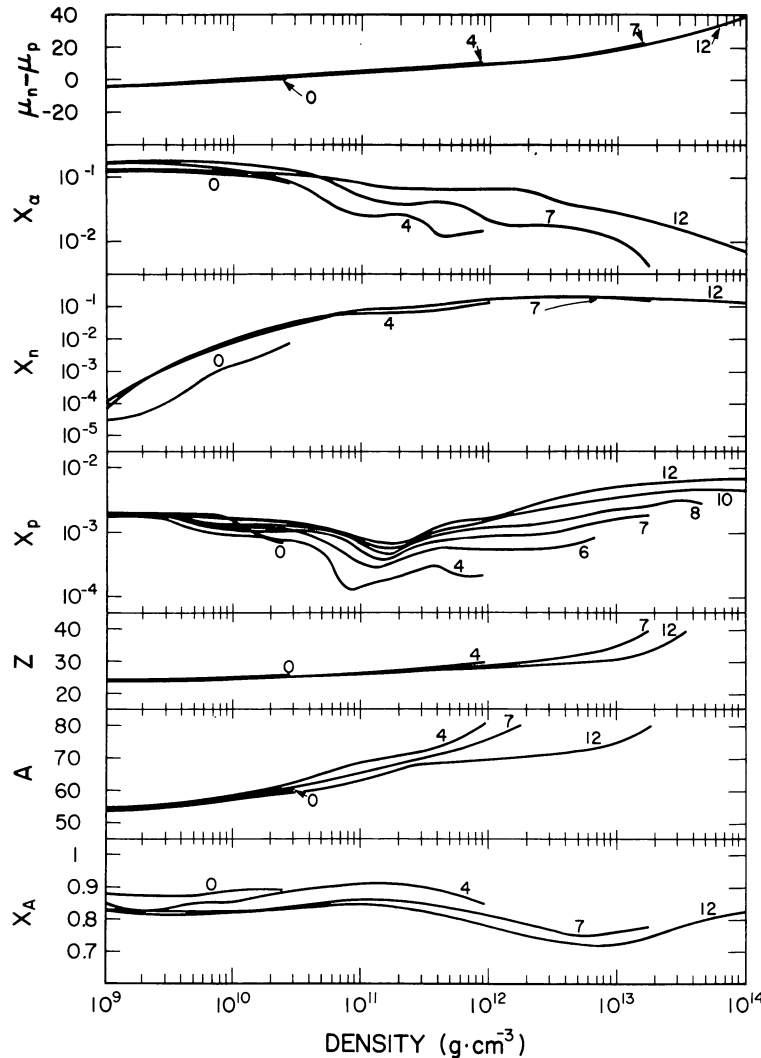


FIG. 3.—Composition vs. density for stages 0, 4, 7, and 12 of the core infall. X_n , X_p , X_α , and X_A are the mass fractions of neutrons, protons, α -particles, and heavy nuclei, respectively; A and Z are the mean mass number and charge number of the heavy nuclei, respectively; and $\mu_n - \mu_p$ ($= \hat{\mu}$) where μ_n and μ_p are the neutron and proton chemical potentials, respectively. Graphs of X_p vs. density are also shown for stages 6, 8, and 10 of the core infall.

about $5 \times 10^{10} \text{ g cm}^{-3}$ at stage 2 to about $1.3 \times 10^{11} \text{ g cm}^{-3}$ at stage 12. A similar effect occurred in the calculation of Van Riper and Lattimer (1981; see their Table 1) and was discussed by Van Riper (1982). The significance of this for the deleptonization of the core will be discussed in § IIIc.

To make possible a better understanding of the other trends in the compositions of the standard model illustrated in Figure 3, Figure 4 shows the dimensionless entropy per baryon versus density and the electron fraction versus density for the same four infall stages shown in Figure 3. It is seen that the electron fraction decreases monotonically with increasing density as does the initial entropy per baryon. However, the latter develops several minima during the collapse as combinations of β -processes occur which increase the entropy in certain density regions and decrease it in others (see § IIIe below).

The free neutron abundance increases with density as a result of the decrease in the electron fraction with increasing density, the general trend of increasing entropy with increas-

ing density above $2 \times 10^{11} \text{ g cm}^{-3}$, and the fact that at constant entropy and electron fraction the free particle abundances increase with density. The free proton-free neutron ratio is given by

$$n_p/n_n = \exp(-\hat{\mu}/kT) \quad (3.1)$$

for nondegenerate conditions for the free nucleons, where $\hat{\mu} = \mu_n - \mu_p$. The decrease in the free proton abundance with increasing density up to about $2 \times 10^{11} \text{ g cm}^{-3}$ results from a decrease in expression (3.1) with increasing density. This, in turn, is due to the increase in the symmetry energy $\hat{\mu}$ with decreasing electron fraction. Above about $2 \times 10^{11} \text{ g cm}^{-3}$ the β -processes tend to heat the material substantially, and the entropy, with some fluctuations, increases with increasing density above this value. This reverses the tendency for expression (3.1) to decrease with increasing density and results

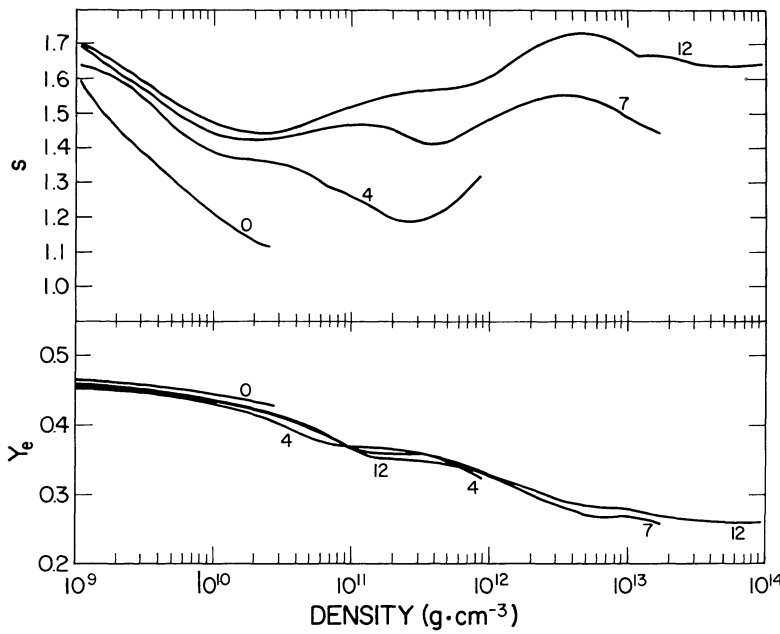


FIG. 4.—The entropy per baryon s divided by the Boltzmann constant, and the electron fraction Y_e as a function of density for stages 0, 4, 7, and 12 of the core infall.

in the free proton abundance increasing with density above about 2×10^{11} g cm $^{-3}$.

The decrease in the α -particle mass fraction with increasing density is a little more involved. The relevant Saha equation gives

$$n_\alpha/n_n \propto \rho^3 X_n^3 T^{-9/2} \exp(Q_\alpha - \bar{\mu})/kT, \quad (3.2)$$

where the symbols have their usual meanings. Generally, the decrease in the exponential with increasing density dominates the other factors and is due to the decrease in the electron fraction. In fact, the rapid decreases in X_α with increasing density are correlated with the rapid decreases in the electron fraction with increasing density. These occur in density regions near 10^{11} and 10^{12} g cm $^{-3}$, where electron captures on nuclei and on free protons become, respectively, most rapid (see § III**b**).

b) Neutrino Production and Equilibration

The neutrino production that occurs during the infall of the standard model is apparent from the net matter-neutrino energy transfer rates, typified by those shown in Figure 5 which are given for stage 12 of the infall. Because a transition to an allowed Gamow-Teller state is possible and because nuclei are the most abundant component of the matter (see Fig. 3), ν_e production by electron captures on nuclei is the dominant neutrino production mechanism at densities below ρ_{cutoff} . At higher densities ($\rho > \rho_{\text{cutoff}}$), the neutron blocking of the $1f_{5/2}$ shell cuts off this process, and ν_e production by electron captures on free protons becomes the dominant neutrino production process. (Electron captures on nuclei mediated by first forbidden matrix elements could occur at densities higher than ρ_{cutoff} , but the rates would be reduced by a factor variously estimated to be between 15 and 400. These forbid-

den processes have not been included here.) Neutrino production by electron-positron pair annihilation never becomes important during the collapse, nor does $\bar{\nu}_e$ production by positron capture on free neutrons. While NES is not a production mechanism, its role in the matter-neutrino energy exchange is shown in Figure 5 and is seen to be comparable in magnitude to the net matter-neutrino energy transfer rate by the dominant neutrino production mechanism, and thus very significant. The role of NES during infall will be discussed in more detail below and in succeeding subsections.

The transport of neutrinos from higher density regimes tends to skew the neutrino occupation distribution (NOD) at a given density toward higher neutrino energies (see Fig. 9), and the NOD can actually exceed the equilibrium NOD above a certain neutrino energy, this energy depending on the density. For densities below 1.5×10^{10} g cm $^{-3}$ at stage 12 of the infall, as an example, the ν_e NOD exceeds the equilibrium ν_e NOD for ν_e energies greater than 9.5 MeV. In the neutrino energy range for which the actual ν_e NOD exceeds the equilibrium ν_e NOD, electron capture reactions are exceeded by their inverses, and a net absorption of neutrinos in this energy range occurs. In the density range from 6×10^9 to 3×10^{12} g cm $^{-3}$, the net neutrino emission rate at low energies by electron captures on free protons is exceeded by the net neutrino absorption at high energies. The result is a net absorption of neutrinos by the nuclei, however, does not occur for any density at this stage of the infall. This is because the net neutrino emission by electron captures at low energies on nuclei always exceeds the net absorption of neutrinos at high energies on nuclei. This difference between the free nucleons and the nuclei in their net rates of neutrino absorption and emission is due to the skewed ν_e NOD. The neutrinos produced by electron captures on free protons have

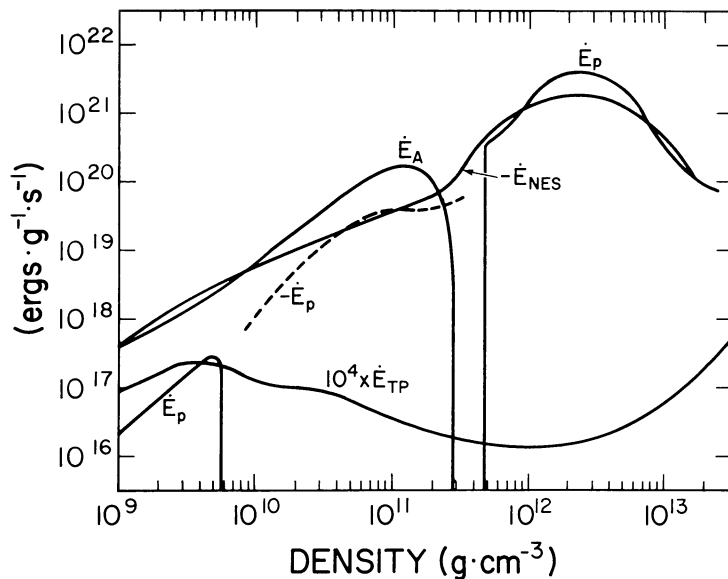


FIG. 5.—Matter- ν_e energy transfer rates as a function of density for stage 12 of the core infall. \dot{E}_p , \dot{E}_A , \dot{E}_{NES} , and \dot{E}_{TP} are the net energy transfer rates from matter to ν_e 's (ergs per gram of matter) by electron captures on free protons, electron captures on nuclei, neutrino-electron scattering, and ν_e pair production by electron-positron annihilation, respectively. The energy transfer rate for each process includes the inverse reaction. The dashed line shows the magnitude of the energy transfer rate by electron captures on free protons in the density range for which this rate is negative.

higher mean energies than those produced by electron captures on nuclei. Since the ν_e NOD is skewed to high energies, it tends to block the electron captures on free protons more than the electron captures on nuclei. This in turn leads to a ratio of neutrino absorption to emission on the free nucleons that is greater than that on the nuclei. (For a ν_e NOD equilibrated with matter, the ν_e emission and absorption on either nucleons or nuclei must, of course, balance at any neutrino energy.)

The processes primarily responsible for the equilibration of neutrinos with matter are absorption and emission of ν_e 's and $\bar{\nu}_e$'s on free nucleons and of ν_e 's on nuclei, and NES for all neutrino types. Figures 6–9 show the effects of these processes for the ν_e 's. Figure 6 illustrates the case for which only ν_e absorption and emission on free protons are considered. The ν_e emission rate goes essentially as ω^2 , where ω is the ν_e energy, until $\omega + Q = \mu_e$ (see eq. [C15]), so the emitted ν_e 's tend to fill the higher energy states first. Using equation (C15), the time needed to fill available phase space at 10 MeV with ν_e 's produced by electron captures on free protons is about $1.4 \times 10^7 / \rho X_p$ s, where X_p is the mass fraction of free protons. The density *e*-folding time, τ_ρ , is given by

$$\tau_\rho = \rho / \dot{\rho} = \chi / (24\pi G\rho)^{1/2}, \quad (3.3)$$

where χ is the ratio of the density *e*-folding time to the free-fall time scale. Taking values of $\chi = 3.1$ and $X_p = 4.5 \times 10^{-3}$, which apply to a mass shell enclosing a rest mass of $0.289 M_\odot$, gives $\rho \approx 5 \times 10^{12}$ as the density at which the ν_e phase-space filling time becomes shorter. A glance at the NODs for the $0.289 M_\odot$ Lagrangian point (LP) in Figure 6 shows that the 10 MeV ν_e 's are beginning to fill their available phase space at about this density.

The effect of including NES in addition to ν_e emission and absorption by free nucleons (model NES) is dramatic, and is shown in Figure 7. With NES included, ν_e 's are effectively equilibrated with matter at a density which is almost an order of magnitude lower than that for model NP, which does not include NES. By downscattering in energy some of the excess high-energy ν_e 's produced by electron captures on free protons, NES lowers the mean ν_e energy in the important transport regime ($\rho \gtrsim$ trapping density). This has the consequence of considerably greater core deleptonization, as will be discussed in the next subsection.

The production and equilibration of ν_e 's when electron captures on nuclei and nucleons are both included, but without the inclusion of NES, are shown in Figure 8. Here it is seen that in some cases the ν_e NOD assumes a double-humped appearance. The bulk of the ν_e 's emitted by electron captures on nuclei are at relatively low energies because the emission takes place at low densities ($\rho < \rho_{\text{cutoff}}$), where the electron Fermi energy is low, and because the energy penalty that must be paid to convert a bound proton to a more loosely bound neutron is relatively large. These ν_e 's comprise the low-energy hump of the NOD. The high-energy hump of the NOD consists of the ν_e 's emitted by electron captures on free protons. Because of the low abundance of free protons, these electron captures are delayed until higher densities are reached ($\rho > 10^{12} \text{ g cm}^{-3}$), where the electron Fermi energy is high. In addition, only the negligible energy penalty of the neutron-proton mass difference must be paid. Most of the ν_e 's produced by electron captures on free protons are therefore of considerably higher energy than those produced by electron capture on nuclei.

The production and equilibration of ν_e 's in the standard model is shown in Figure 9. The standard model differs from model A by the inclusion of NES. A comparison of Figures 8

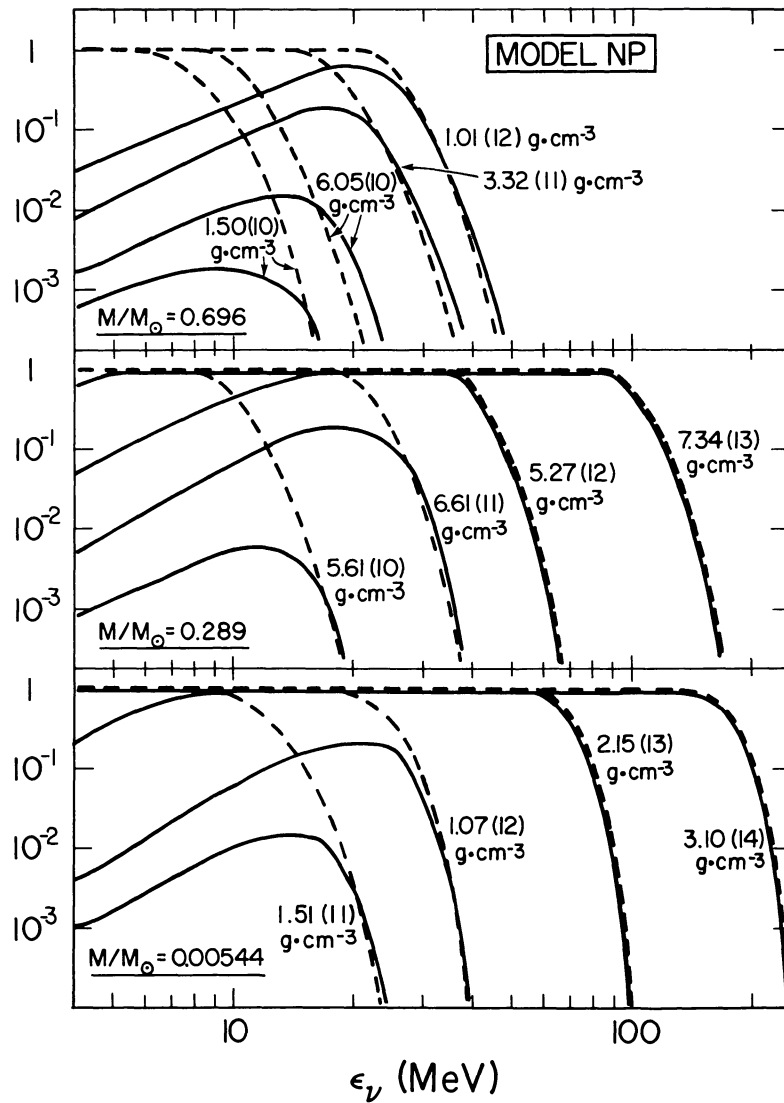


FIG. 6.—The dashed and solid lines give, respectively, the equilibrium ν_e occupation distribution and the zero moment of the actual neutrino occupation distribution as a function of ν_e energy for the indicated densities during the core infall of model NP. By equilibrium ν_e occupation distribution is meant the ν_e distribution that would be equilibrated with the matter at the indicated thermodynamic state of the latter. The numbers in parentheses denote corresponding powers of 10. The lower, middle, and upper panels correspond to Lagrangian points enclosing rest masses of 0.00544, 0.289, and $0.696 M_\odot$, respectively.

and 9 shows that ν_e 's in the standard model become equilibrated with matter at a considerably lower density than in model A. For example, the ν_e NOD of the $0.289 M_\odot$ LP in model A is 70% of the equilibrium ν_e NOD at 4 MeV when $\rho \approx 9.8 \times 10^{12} \text{ g cm}^{-3}$, and at 9.7 MeV when $\rho \approx 6.5 \times 10^{12} \text{ g cm}^{-3}$. The corresponding densities in the standard model are about $9 \times 10^{11} \text{ g cm}^{-3}$ at both 4 and 9.7 MeV. This is similar to the differences in the densities at which ν_e 's become equilibrated with matter between model NP and model NES.

In the standard model a comparison of the densities at which the neutrinos become equilibrated with matter as a function of the Lagrangian distance of the matter from the center shows that higher densities are reached before neutrino equilibration is achieved for matter at greater Lagrangian

distances. This results from the increase in the compression rate at a given density with increasing Lagrangian distance from the center, and will be discussed in more detail in the next subsection.

c) Neutrino Transport and the Deleptonization of the Core

The deleptonization of the core during infall is perhaps the single most important aspect of this calculation because of its sensitive effect on the hydrodynamics and on the success of the shock formed during the core bounce in propagating out and expelling matter in a prompt fashion. Considerable space will therefore be devoted to describing it.

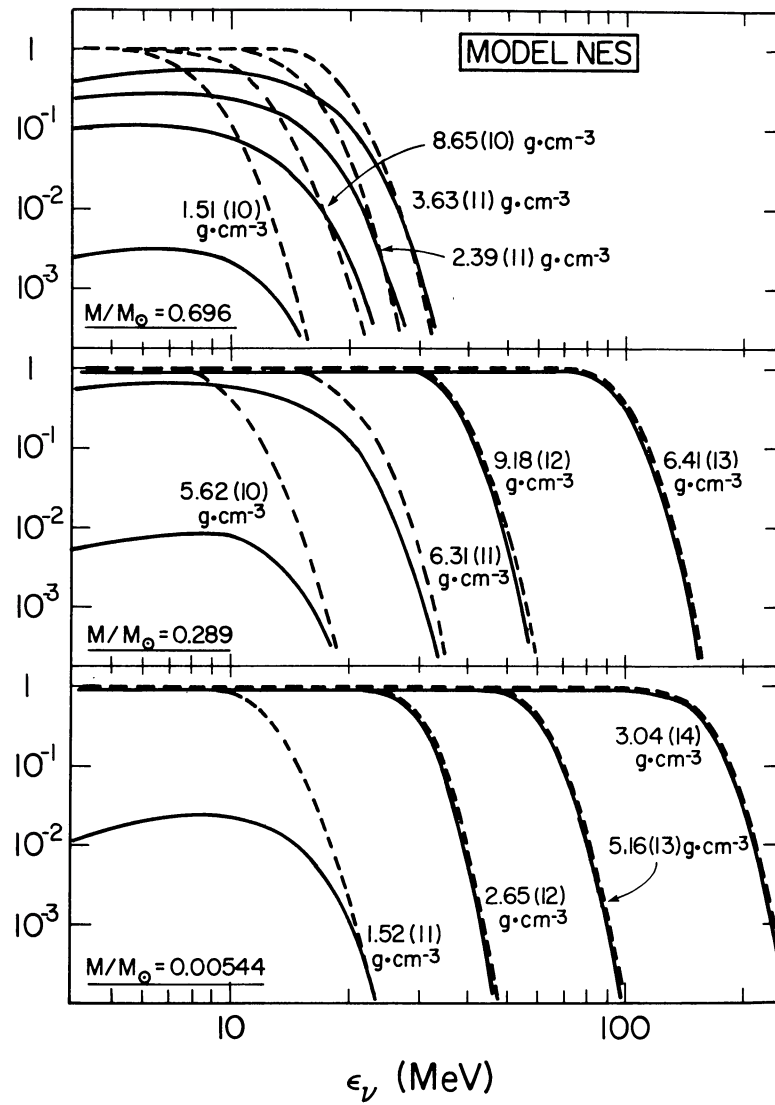


FIG. 7.—The same as Fig. 6, but for model NES

i) *Deleptonization Trajectories*

The lepton, electron, and electron neutrino number fractions as a function of density during infall for models NP, NES, A, and SM are shown in Figures 10 and 11 for LPs enclosing rest masses of $0.00544 M_{\odot}$ and $0.289 M_{\odot}$, respectively. For all models, $Y_l = Y_e$ until $\rho \approx 10^{11} \text{ g cm}^{-3}$, at which point Y_e begins to fall below Y_l , and Y_e rises because of the increasing inability of neutrinos to escape freely. While the neutrino trapping criterion (see below) is satisfied for ρ above $4 \times 10^{11} - 10^{12} \text{ g cm}^{-3}$, depending on the model and the stage of the collapse (see below), deleptonization continues until $\rho \approx 2 \times 10^{12} \text{ g cm}^{-3}$ for the $0.00544 M_{\odot}$ LP and $\rho \approx 3 \times 10^{12} \text{ g cm}^{-3}$ for the $0.289 M_{\odot}$ LP. Letting ρ_{trap} and ρ_{delep} denote, respectively, the neutrino trapping density and the density at which deleptonization effectively ceases during the infall, the fact that ρ_{delep} is a factor of 2–8 larger than ρ_{trap} indicates that the outward transport of neutrinos through mass is still

significant above the trapping density, even though neutrinos may be moving inward in an Eulerian sense.

Neutrino leakage schemes (NLSs) have been used for neutrino transport in some recent stellar collapse calculations. A characteristic of NLSs is that they transport neutrinos from a given mass zone directly out of the core without consideration of the neutrino's zone-to-zone propagation. It is therefore interesting to compare two published deleptonization trajectories given by such schemes with our results. Van Riper and Lattimer (1981; their Figs. 8 and 10), using an NLS, found the onset of $Y_l = \text{constant}$ to be very abrupt, which is at variance with our results. Bludman, Lichtenstadt, and Hayden (1982; their Figs. 4 and 6), using an NLS with a one-zone hydrodynamics scheme, obtained shapes for deleptonization trajectories more similar to ours. Since transport of neutrinos through mass appears to be significant at densities above ρ_{trap} , NLSs which abruptly terminate neutrino transport above ρ_{trap} (e.g.,

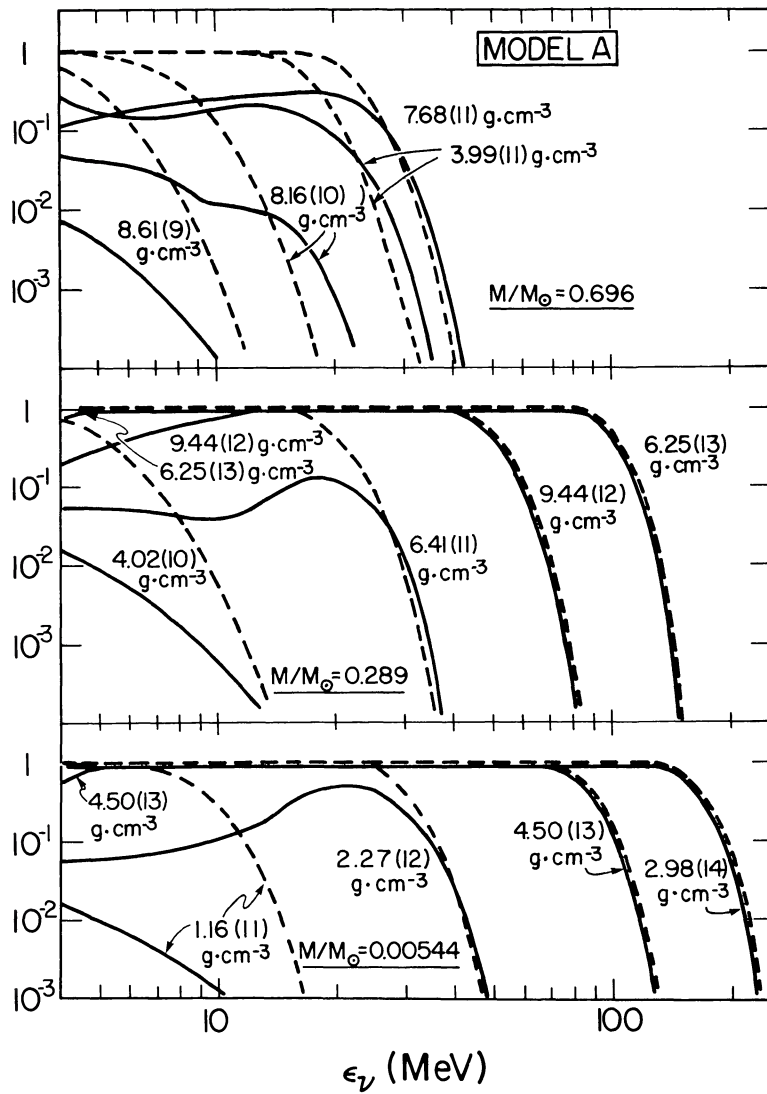


FIG. 8.—The same as Fig. 6, but for model A

Hillebrandt and Müller 1981) may significantly underestimate the extent of the deleptonization of the inner mass zones.

Further details of the deleptonization trajectories given in Figures 10 and 11 can be appreciated by referring to Figure 12, which gives the e -folding times for changes in density, lepton fraction, and electron fraction for stages 4, 6, 8, and 10 of the infall of the standard model. The figure shows that the density e -folding time, τ_ρ , decreases at any given constant density as the collapse proceeds. This result has its counterpart in the self-similar collapse solutions of Yahil and Lattimer (1982) and Yahil (1983). According to these solutions, the inner core collapses almost homologously if the effective adiabatic index, Γ_E (see eq. [3, 19]) is less than $4/3$, and exactly homologously if $\Gamma_E = 4/3$. In the latter case the enclosed mass m varies only with the similarity variable X (Yahil 1983; his eq. [8]), so the mass and time dependence of the density evolution are in this case separable, i.e., $\rho(m, t) = \rho_0(m)f(t)$. The analysis of Van Riper and Lattimer (1982) is

then applicable, and leads to the relation (their eq. [33])

$$\tau_\rho(m_1, \rho^*)/\tau_\rho(m_2, \rho^*) = [\rho_0(m_1)/\rho_0(m_2)]^{1/2}, \quad (3.4)$$

where $\tau_\rho(m_1, \rho^*)$ is the density e -folding time of the matter at LP m_1 (i.e., enclosing a rest mass m_i) when it reaches density ρ^* , and $\rho_0(m_i)$ is the density at m_i at some prior time t_0 during the homology. Thus, the compression rate for two inner-core mass shells at LPs m_1 and m_2 as they each pass through the same density ρ^* is greater for the mass shell enclosing the larger rest mass. This conclusion is similar to that reached by Bludman, Lichtenstadt, and Hayden (1982) but appears to differ from their statement that the collapse rate is the same for all homologously collapsing mass zones, so that one-zone collapse calculations exactly describe the evolution of the homologous core. This latter statement is correct in the sense that at any given time the value of τ_ρ for each homologously collapsing mass zone is the same. The im-

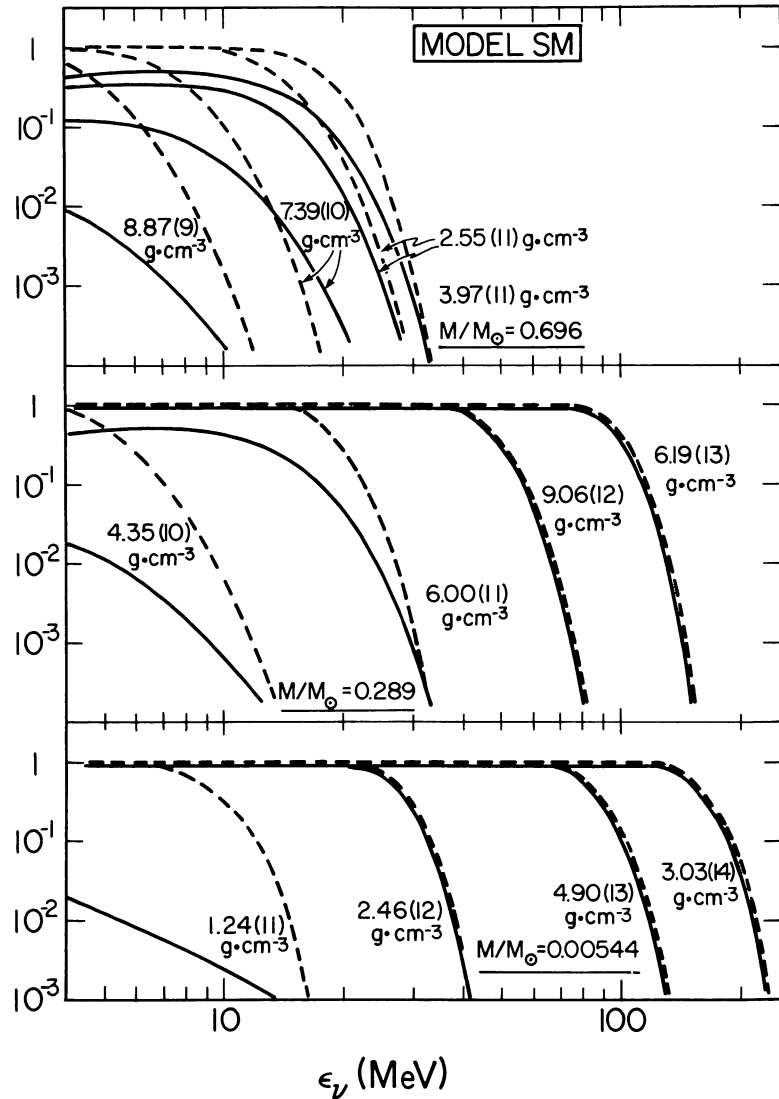


FIG. 9.—The same as Fig. 6, but for the standard model

portant point is that these mass zones are at different densities when τ_p is the same, and it is the compression rate at a given density (not time) that is most relevant for the calculations of the deleptonization of a given mass zone.

It was pointed out in the preceding section that for the standard model the electron capture rate is dominated by the rate on heavy nuclei in the density range of 10^{10} g cm $^{-3}$ to ρ_{cutoff} ($\sim 10^{11}$ g cm $^{-3}$) and by the rate on free protons at higher densities, the latter rate becoming large in the density range of 5×10^{11} – 2×10^{12} g cm $^{-3}$ (see Fig. 5). This is also evident from the curves for $\tau_{e\text{-cap}}$, the electron capture e -folding time, as a function of density given in Figure 12, which show pronounced minima in the above two density ranges. It is interesting to examine the electron-capture and deleptonization trajectories and the extent of electron capture and deleptonization of a mass shell during infall as a function of its Lagrangian distance from the center of the core.

Consider first the electron captures on heavy nuclei. The shell closure cutoff for this process occurs at a density, ρ_{cutoff} , sufficiently below ρ_{trap} so that essentially all the neutrinos produced are able to escape. Thus, $Y_l = Y_e$ for mass zones close to the center during this stage of electron capture. For mass zones at greater Lagrangian distances, $Y_l > Y_e$ because of the presence of ν_e 's flowing through from interior zones. Referring to Figures 10 and 11, it is seen that by the time $\rho = \rho_{\text{cutoff}}$ the value of Y_l for the standard model has been reduced to about 0.37 for both 0.00544 and the 0.289 M_\odot LPs. Remarkably, Y_l is reduced to about this same value for any mass zone that undergoes this stage of electron capture by the time its density reaches ρ_{cutoff} (see Fig. 14). The decrease in Y_l from its initial value for a given mass zone during this stage depends on the combination of its compression rate, the value of ρ_{cutoff} , the heavy-nucleus number fraction Y_A , and the number fraction of ν_e 's flowing through from interior zones.

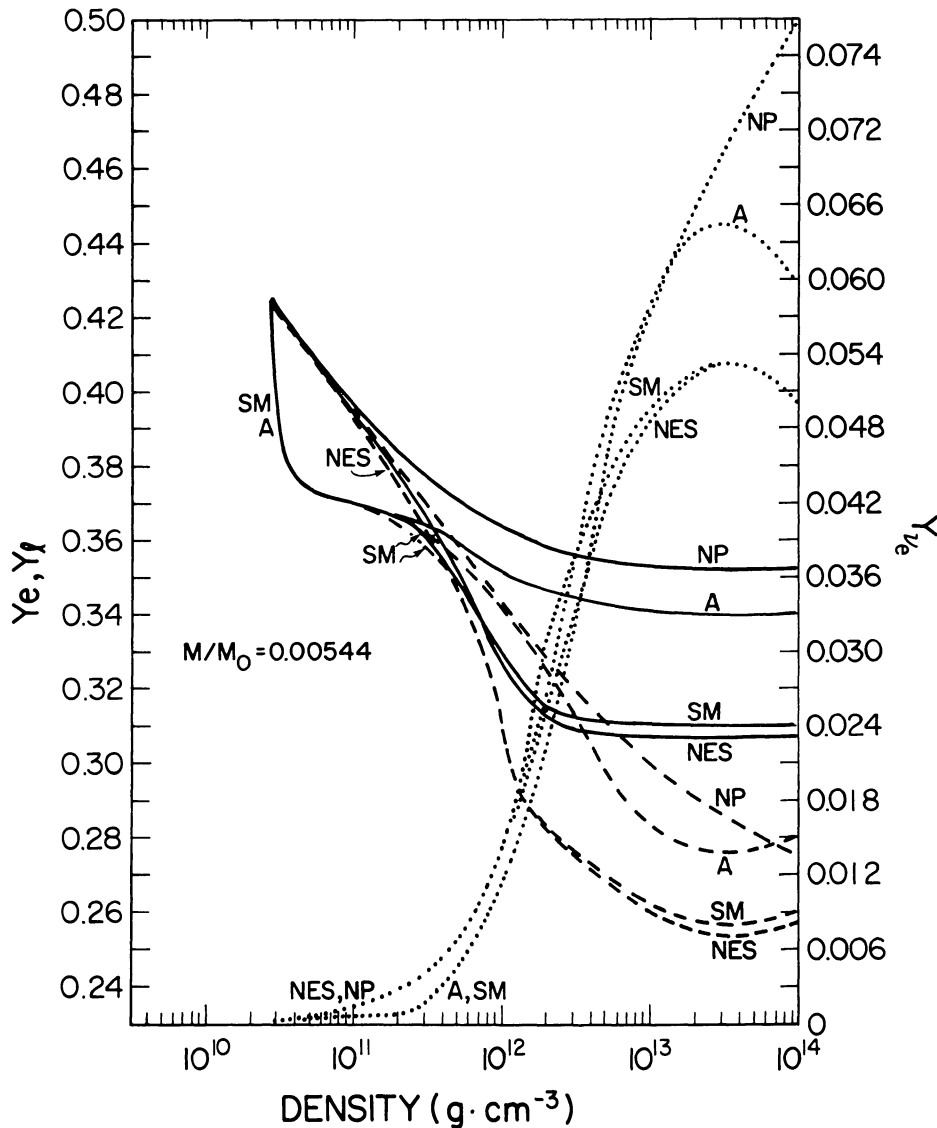


FIG. 10.—Lepton fractions as a function of density for models NP, NES, A, and SM, for a Lagrangian point enclosing a rest mass of $0.00544 M_{\odot}$. The dotted, dashed, and solid lines correspond to the ν_e fraction, electron fraction, and lepton fraction, respectively.

According to Figure 3, the value of $Y_A = X_A/A$ is approximately constant at a given constant density for different LPs. On the other hand, the compression rate, τ_p^{-1} , at a given density increases with Lagrangian distance, as does the number fraction, Y_{ν_e} , of ν_e 's flowing through from interior zones. Both of these latter factors tend to cause the deleptonization of a mass zone, when its density reaches ρ_{cutoff} , to decrease with increasing Lagrangian distance. Slightly overcompensating for these factors is the effect of the increase in ρ_{cutoff} with Lagrangian distance, with the net result of a slight increase in the deleptonization with increasing Lagrangian distance when the matter density reaches ρ_{cutoff} . This almost cancels the slight increase in the initial Y_l with Lagrangian distance, and yields a value of Y_l at ρ_{cutoff} which is nearly independent of Lagrangian distance.

This reduction of Y_l by electron captures on heavy nuclei to about the same value independent of the Lagrangian distance

of the mass zone is evident in Figures 13 and 14. The bottom panel in Figure 13 shows Y_l as a function of enclosed rest mass for various stages of the core infall of the standard model. The plateaus of the graphs at $Y_l \approx 0.37$ correspond to matter that has been deleptonized by electron captures on heavy nuclei, but not yet by electron captures on free protons. It is seen that Y_l has the value of about 0.37 on these plateaus, independent of the enclosed rest mass. Figure 14 shows that the Y_l trajectory for any given LP passes through approximately the same value of 0.37 for Y_l when the density has the value of ρ_{cutoff} for that LP.

The deleptonization trajectories of given mass zones for densities above ρ_{cutoff} , where the electron captures occur on free protons alone, are more complicated to discuss. They depend not only on the compression rate of this mass zone, the value of ρ_{trap} , and the value of the free proton mass fraction X_p , but on the global properties of the neutrino

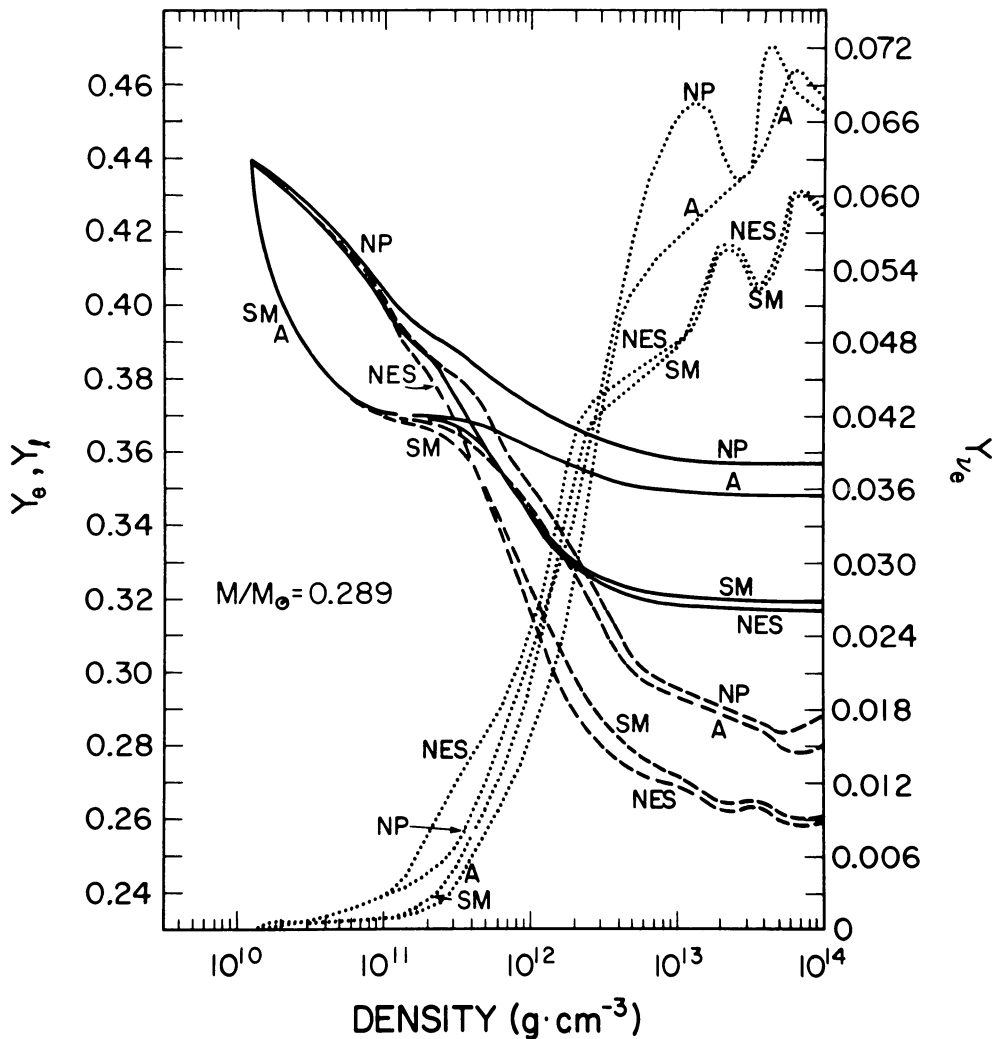


FIG. 11.—Same as Fig. 10, but for a Lagrangian point enclosing a rest mass of $0.289 M_\odot$

transport as well. On the other hand, equilibrated values of Y_e , Y_{ν_e} , and Y_l at core turnaround depend only on the extent of the deleptonization, which determines Y_l , and the set of equations

$$\mu_e = \mu_{\nu_e} + \hat{\mu} \quad (3.5)$$

and

$$Y_l = Y_e + Y_{\nu_e}, \quad (3.6)$$

which determine Y_e and Y_{ν_e} , where we have neglected the contribution of antileptons in equation (3.6) because they do not appear in significant numbers at this stage of the collapse evolution.

A remarkable coincidence also characterizes the stage of electron captures for densities above ρ_{cutoff} and for matter comprising the inner core. A comparison of the free proton mass fractions shown in Figure 3 with the compression rate τ_p^{-1} shown in Figure 12 reveals that, for the inner core, both exhibit almost the same relative increase with Lagrangian

distance at a given density during the infall. As a result, for densities above ρ_{cutoff} , the increase in the electron capture rate with Lagrangian distance at a given density is about the same as the increase in the compression rate. To the extent that the effects of neutrino transport can be neglected, the evolution of Y_l with the density for a given mass zone is therefore practically independent of its Lagrangian position. This characteristic of the Y_l evolution for densities above ρ_{cutoff} is shown explicitly in Figure 15a by the similarity of the electron capture trajectories of various LPs in (Y_l, ρ) -space for a collapsing model (model NT) in which the transport mean free paths have been set to zero for densities above $5 \times 10^{11} \text{ g cm}^{-3}$, thereby suppressing the effects of neutrino transport above this density. With neutrino transport turned off above $5 \times 10^{11} \text{ g cm}^{-3}$, the value of Y_l at any higher density for a given LP was equal to its value at $5 \times 10^{11} \text{ g cm}^{-3}$, which was approximately independent of Lagrangian distance as discussed above. With the high degree of degeneracy of the leptons in the inner core, the density dependence of both μ_e and μ_{ν_e} is $\rho^{1/3}$, while their temperature dependence is very slight. For constant Y_e the value of $\hat{\mu}$ varies with Lagrangian

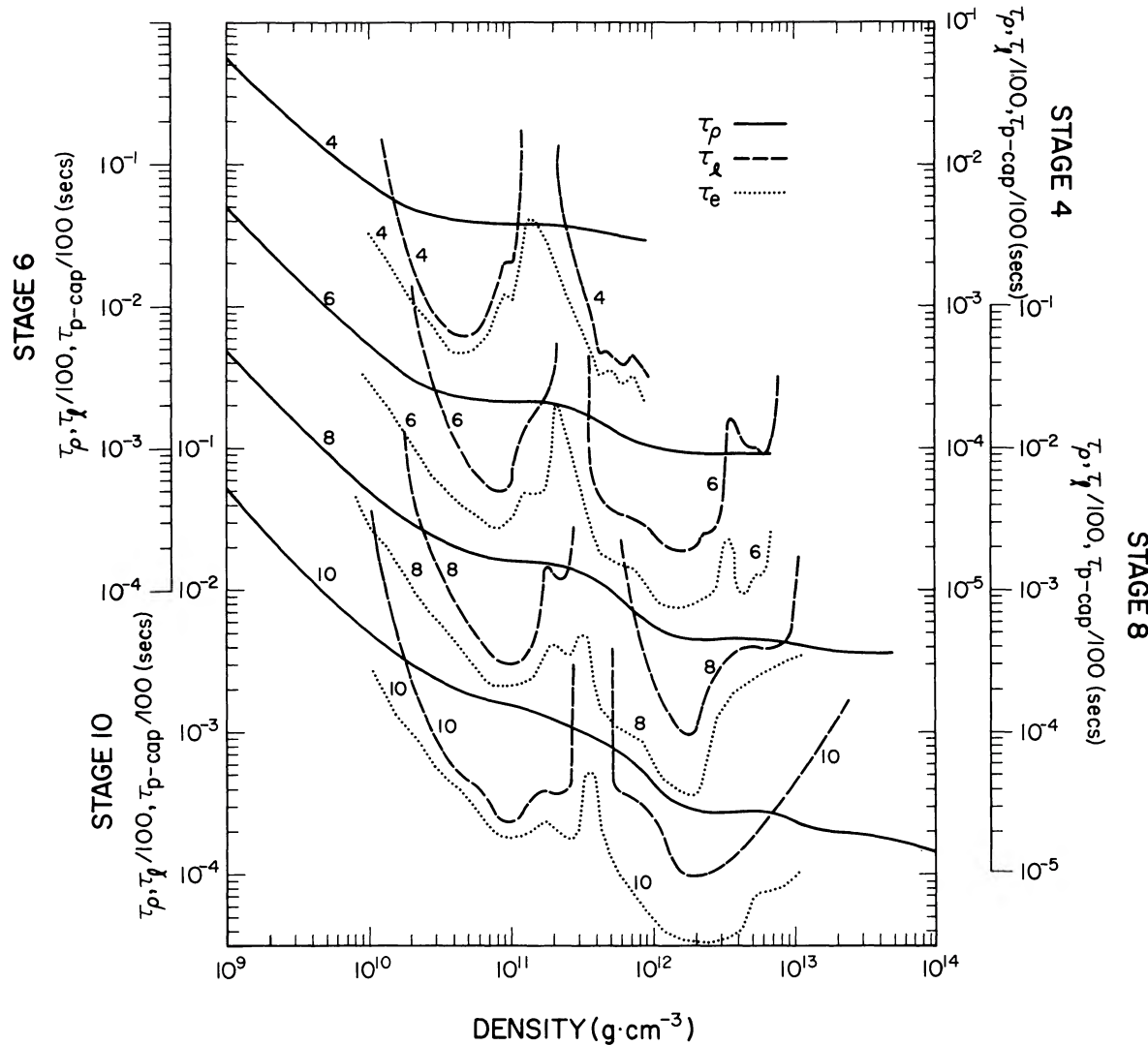


FIG. 12.—The time scales $\tau_p = \rho/\dot{\rho}$ (solid line), $\tau_l = Y_l/(-\dot{Y}_l)$ (dashed line), and $\tau_{e\text{-trap}} = Y_e/(-\dot{Y}_e)$ (dotted line) vs. density for stages 4, 6, 8, and 10 of the standard model during infall.

position approximately as $\rho^{1/3}$. Thus, with the ρ -dependence in Lagrangian distance canceling out in equation (3.5), and the T -dependence slight, equations (3.5) and (3.6) for a constant value of Y_l are satisfied by constant values of Y_e and Y_{ν_e} . Figure 15b shows that Y_e for the inner $0.5 M_\odot$ of model NT is, indeed, approximately constant.

The effect of neutrino transport at densities above $5 \times 10^{11} \text{ g cm}^{-3}$ on the equilibrated values of the lepton fractions is evident by a comparison of model NT with the standard model. Figure 15b shows Y_e and Y_l as a function of the enclosed rest mass for both of these models. It is seen that the effect of including neutrino transport at densities above $5 \times 10^{11} \text{ g cm}^{-3}$ is to decrease Y_l in the inner $0.6 M_\odot$ of the core. Instead of being independent of Lagrangian distance as is the case for model NT, however, Y_l for model SM exhibits a gradual increase with Lagrangian distance. The reasons for this are (1) the increase in the compression rate of the matter

with increasing Lagrangian distance, resulting in less time for neutrino transport to deleptonize the matter of greater Lagrangian distances, and (2) the outward flow of ν_e 's, some of which become trapped in the matter at greater Lagrangian distances. This latter effect accounts, in particular, for the rise in Y_l for model SM above that for model NT in the matter outward of $0.6 M_\odot$ at stage 12 of the infall (Fig. 15b).

It is interesting to compare the lepton fraction profile of model SM (Fig. 13 [bottom panel] or Fig. 15b) shortly before core turnaround (stage 10 or stage 12) with those of other published calculations. The calculations which have used a multienergy zone scheme for the transport of neutrinos (Wilson 1978, 1980; Bowers and Wilson 1982b; Arnett 1977b) all show a similar lepton fraction profile, with Y_l increasing with Lagrangian distance through the inner core. Calculations using less sophisticated neutrino transport schemes (Mazurek, Cooperstein, and Kahana 1980; Van Riper and Lattimer

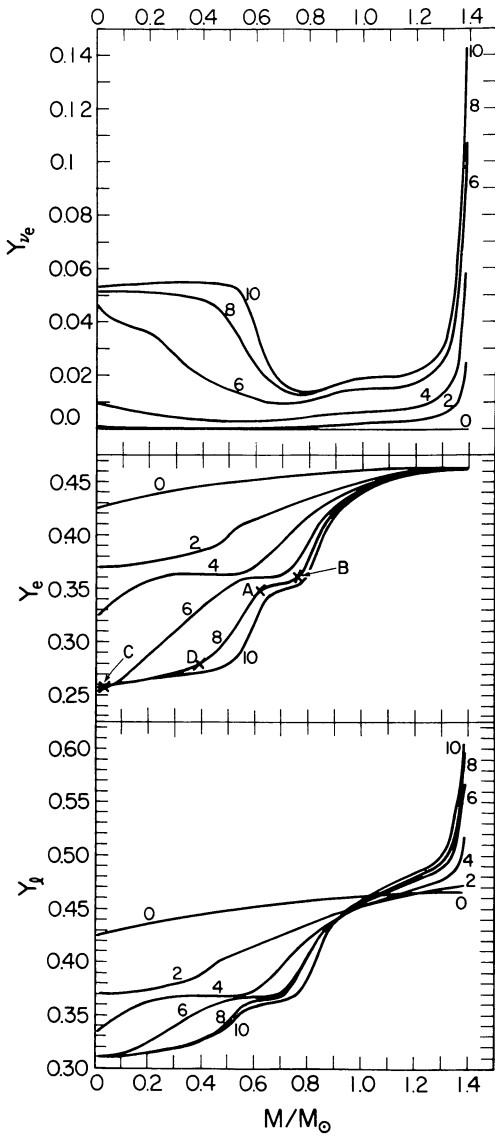


FIG. 13.—Instantaneous profiles of the ν_e fraction Y_{ν_e} (top), electron fraction Y_e (middle), and lepton fraction Y_l (bottom) for stages 0, 2, 4, 6, and 10 of the infall of the standard model. The profiles for Y_e and Y_l develop two approximately horizontal plateaus during the later stages of the core infall, which move rightward in the figure as the collapse proceeds. For a given profile, the plateaus at the higher values of Y_e and Y_l correspond to the matter at densities above ρ_{cutoff} for electron captures in heavy nuclei, but at densities still low enough for the rate of electron capture on free protons to be relatively small. The plateaus at the lower values of Y_e and Y_l correspond to the matter in β -equilibrium.

1981) give a lepton fraction profile which first decreases and later increases with Lagrangian distance, producing a minimum of Y_l away from the center.

ii) Neutrino Trapping Density

Neutrino trapping occurs above the density, ρ_{trap} , at which the neutrinos no longer move outward in space, i.e., at which the inward velocity of the material equals the outward drift velocity of the neutrinos relative to the material. While ρ_{trap} is obviously a function of the neutrino energy, an average value

of ρ_{trap} , which will be referred to as the “trapping density” and denoted hereafter by ρ_{trap} , will be defined as the monoenergetic neutrino drift velocity averaged over ω with respect to the neutrino number distribution. The neutrino trapping density of the standard model is exhibited in Figure 16a for stages 4, 6, 8, and 10 of the core infall by the intersection of the matter infall velocity curves with the corresponding neutrino drift velocity curves. The trapping density depends on the neutrino opacity through the latter’s influence on the neutrino drift velocity. Since the neutrino opacity is dominated by the coherent scattering of neutrinos on heavy nuclei, it depends on the mean energy of the neutrinos and the mean size of the heavy nuclei. The mean (flux-averaged) energy of the neutrinos $\langle \epsilon_{\nu_e} \rangle$, increases slightly during the collapse, as is shown in Figure 16b. This is due to the slight increase in the energy needed to drive the electron captures on free protons, since the increase in the compression rate at a given density as the collapse proceeds is not quite matched by the increase in the free proton abundance. NES tends to minimize this increase in $\langle \epsilon_{\nu_e} \rangle$. On the other hand, the mean size, A , of the heavy nuclei decreases at the trapping density as the collapse proceeds, due to the outward increase of entropy of the initial configuration of the standard model. The changes in $\langle \epsilon_{\nu_e} \rangle$ and A are both rather small and have opposing effects on the neutrino opacity, and the neutrino drift velocity is therefore essentially unchanged after stage 6 of the infall for $\rho < 10^{12} \text{ g cm}^{-3}$. (At higher densities an increase in the neutrino drift velocity with time occurs as a result of the changing density structure of the core.) Since the neutrino drift velocity is approximately constant in time in the trapping region, the principal cause for the change in the neutrino trapping density with time, then, is the increasing infall velocity of the material. As is shown in Figure 16a, the effect is to reduce the trapping density from about $10^{12} \text{ g cm}^{-3}$ at stage 6 of the core infall, which is shortly after neutrinos first become trapped, to about $4.5 \times 10^{11} \text{ g cm}^{-3}$ at stage 10.

iii) The Effects of Electron Captures on Free Protons and on Nuclei, and of NES, on the Deleptonization of the Core

Figures 10 and 11 show the effects of electron captures on both free protons and heavy nuclei, and of NES, on the deleptonization of the core during infall. Consider first the two models without NES, i.e., models NP and A. With electron captures on free protons only (model NP), deleptonization proceeds smoothly and continuously during the collapse until $\rho > 10^{12} \text{ g cm}^{-3}$, at which point neutrino transport effectively ceases for the remainder of the infall. Selected values of Y_l for this model are given in Table 4.

The inclusion of electron captures on heavy nuclei as well as on free protons (model A) results in the core deleptonization proceeding through two well-separated stages. There is an initial burst of electron captures on the heavy nuclei which continues up to the heavy-nucleus closure density of $\rho = \rho_{\text{cutoff}} \approx 10^{11} \text{ g cm}^{-3}$, the exact value depending on the stage of the collapse. Since neutrinos escape freely at these densities, the core deleptonizes at the electron capture rate. At the end of this first stage the lepton fraction, Y_l , has been reduced to about 0.37, as discussed above, for all matter having compressed to the heavy-nucleus closure density. Following this first stage of core deleptonization there is a lull in the electron

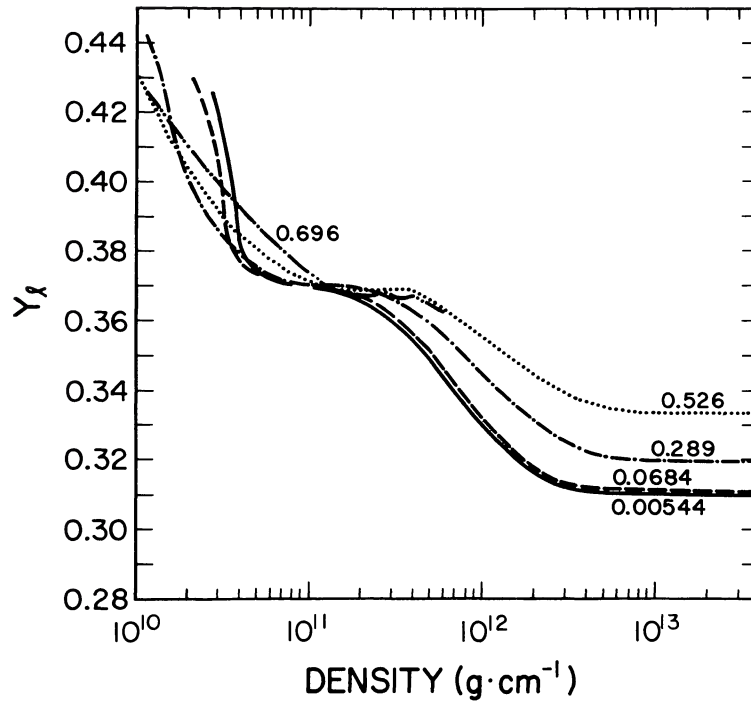


FIG. 14.—Deleptonization trajectories (Y_e vs. density) for Lagrangian points enclosing rest masses of 0.00544, 0.0684, 0.289, 0.526, and 0.696 M_\odot during the infall of the standard model.

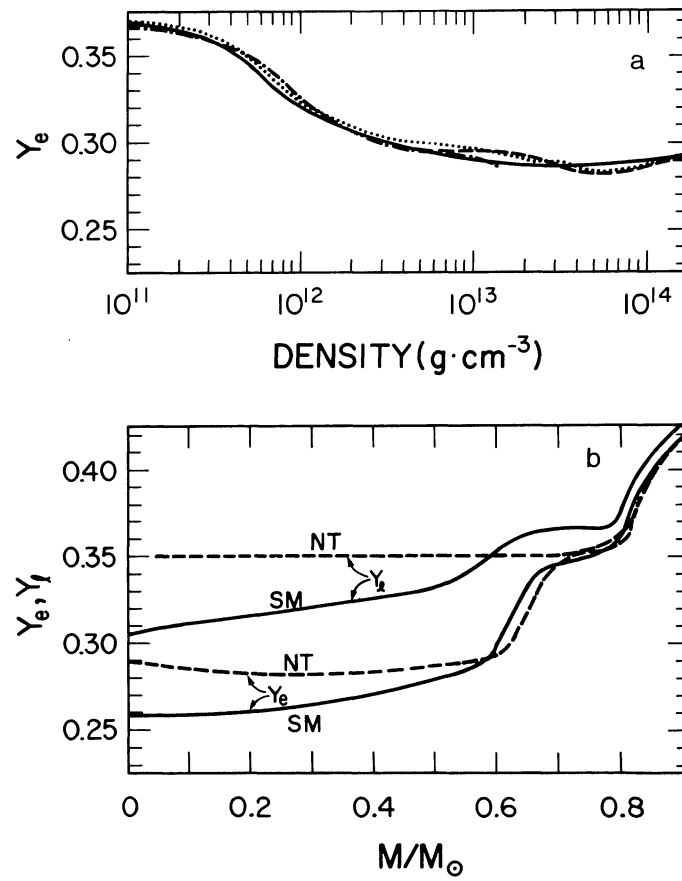


FIG. 15.—(a) Electron capture trajectories in (Y_e, ρ) -space for Lagrangian points of model NT enclosing rest masses of 0.00544 M_\odot (solid line), 0.0684 M_\odot (dashed line), 0.289 M_\odot (dotted line), and 0.526 M_\odot (dot-dash line). (b) Electron fraction and lepton fraction as a function of the enclosed rest mass for stage 12 of the core infall of the standard model (solid line) and model NT (dashed line).

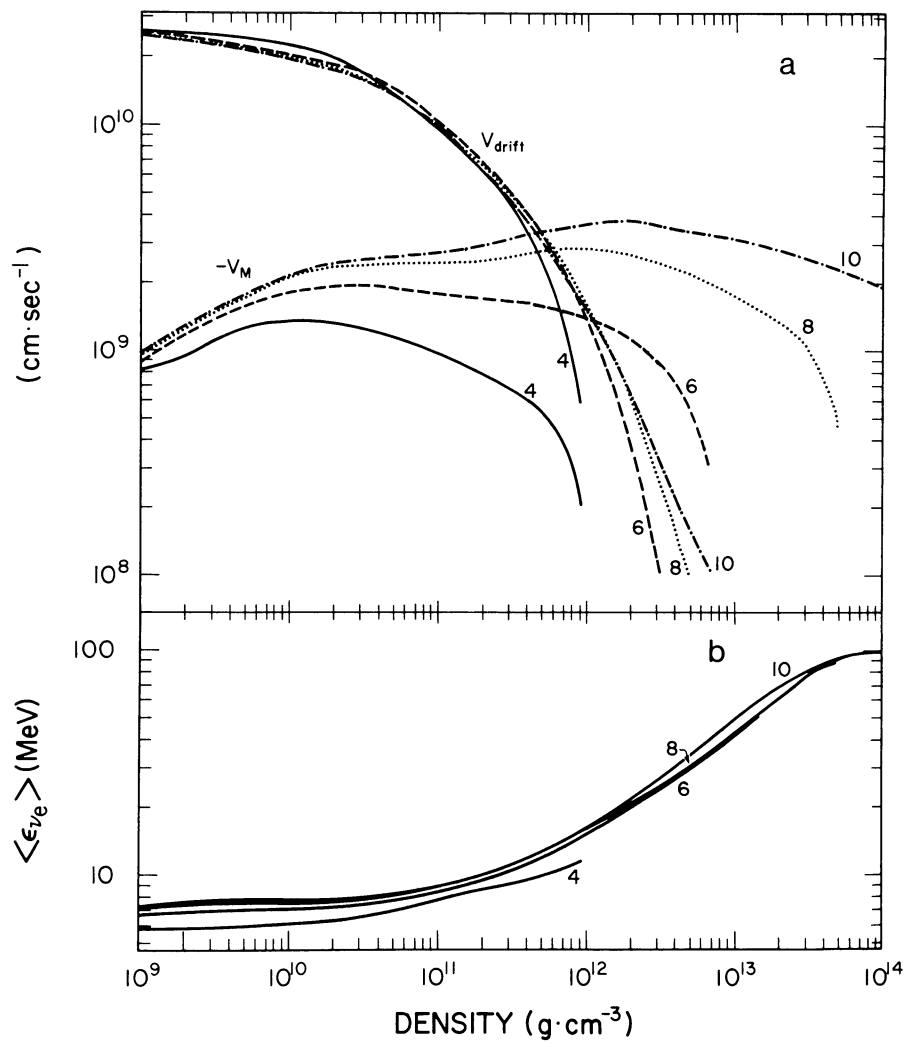


FIG. 16.—(a) The neutrino drift velocity (V_{drift}) and the matter infall velocity ($-V_M$) as a function of density for stages 4, 6, 8 and 10 of the core infall of the standard model. The density corresponding to the intersection of the curves for V_{drift} and $-V_M$ for a given infall stage is defined as the neutrino trapping density (ρ_{trap}) for that stage. (b) The flux-averaged neutrino energy vs. density for stages 4, 6, 8, and 10 of the core infall of the standard model.

TABLE 4
SELECTED VALUES OF Y_I FOR VARIOUS STAGES OF INFALL FOR MODELS NP, A, NES, AND SM

Model	Y_I	Location and Infall Stage
NP	0.382	central value at $\rho_c = 3 \times 10^{11}$ g cm $^{-3}$
	0.365	central value at $\rho_c = 10^{12}$ g cm $^{-3}$
	0.353	central value at core turnaround
	0.377	inner-core edge value at core turnaround
A	0.364	central value at $\rho_c = 3 \times 10^{11}$ g cm $^{-3}$
	0.354	central value at $\rho_c = 10^{12}$ g cm $^{-3}$
	0.340	central value at core turnaround
	0.358	inner-core edge at core turnaround
NES	0.370	central value at $\rho_c = 3 \times 10^{11}$ g cm $^{-3}$
	0.327	central value at $\rho_c = 10^{12}$ g cm $^{-3}$
	0.307	central value at core turnaround
	0.343	inner-core edge at core turnaround
SM	0.361	central value at $\rho_c = 3 \times 10^{11}$ g cm $^{-3}$
	0.332	central value at $\rho_c = 10^{12}$ g cm $^{-3}$
	0.301	central value at core turnaround
	0.340	inner-core edge at core turnaround

NOTE.— ρ_c = central density.

capture rate due to the suppression of the free proton mass fraction as a result of the lowered value of Y_e . This suppression of X_p that follows the first stage of core deleptonization is clearly evident in Figure 3 as a dip in the graphs of X_p versus ρ near $10^{11} \text{ g cm}^{-3}$. As the matter compresses to higher values of the density ($\rho > 5 \times 10^{11} \text{ g cm}^{-3}$), the increased electron chemical potential and the increased value of X_p that results from the general rise of X_p with density at constant entropy results in a second burst of electron captures, this time on the free protons. Now, however, the neutrinos are beginning to be trapped and the deleptonization rate fails to keep pace with the electron capture rate. The values of Y_l are reduced during this stage to 0.34 and 0.35 for the 0.00549 and $0.291 M_\odot$ LPs, respectively, the differences being due primarily to the faster compression rate of the $0.291 M_\odot$ LP and the flow of neutrinos from the inner zones, as discussed previously. Selected values of Y_l for the model are given in Table 4. It is seen from this table that the inclusion of electron captures on heavy nuclei serves to reduce the central value of Y_l at core turnaround by only about 0.01. The reason why the reduction is not larger is that the initial burst of electron captures on the heavy nuclei by reducing Y_e suppresses the free proton abundance that follows and therefore delays the burst of electron captures on free protons until higher densities are reached and neutrino trapping is more effective. Thus, electron captures on heavy nuclei tend to suppress the rate of electron captures on free protons.

The inclusion of NES in models NP and A, resulting in models NES and SM, respectively, gives rise to a considerably greater extent of core deleptonization. There are two principal reasons for this, both of which are consequences of the downscattering of neutrinos in energy by NES. The first is the increase in the mean free paths of the downscattered neutrinos; the second is the entropy increase of the matter resulting from the neutrino downscattering, which tends to increase the free proton fraction Y_p .

Consider the increase in the neutrino mean free paths resulting from the inclusion of NES. Without NES the neutrino spectrum tends to be "top-heavy," as Figures 6 and 8 for

models NP and A show. This results from the electron capture rate being greatest for the most energetic electrons. Neutrinos transported to a given mass shell from interior regions also tend to be of high energy relative to the equilibrium NOD in that mass shell. NES acts to produce thermal equilibration of the NOD with the matter. Given the top-heavy NOD produced by electron capture and transport, the predominant tendency of NES is to downscatter the neutrinos in energy, as is evident by a comparison of Figure 7 with Figure 6 and Figure 9 with Figure 8. Since the magnitudes of the cross sections for neutrino absorption and scattering typically vary as the square of the neutrino energy, the downscattering of neutrinos in energy by NES results in longer neutrino mean free paths and therefore greater neutrino transport.

The effect on the mean neutrino energy of including NES is shown in Figure 17, which gives the flux-averaged neutrino energy as a function of density for stage 8 of the core infall. In the important density range around $6 \times 10^{11} \text{ g cm}^{-3}$, where neutrino trapping is beginning to occur, it is seen that the flux-averaged neutrino energy obtained with NES included is about 0.7 of the value obtained without NES. NES therefore increases the mean free path in this region by about a factor of 2. This increase in the neutrino mean free path increases the neutrino trapping density. The increase is from about $4 \times 10^{11} \text{ g cm}^{-3}$ to $6 \times 10^{11} \text{ g cm}^{-3}$ at stage 8 of the core infall, as is shown in Figure 18. The figure also shows that the inclusion of electron captures on heavy nuclei has little effect on the value of ρ_{trap} (i.e., compare model NP with A, and NES with SM), the reason being that these captures are cut off at a density considerably below ρ_{trap} .

The tendency of NES to increase the entropy of the core during infall can be seen by a comparison in Figure 23 of models NP and A (which do not include NES) with models NES and SM (which do include NES). The evolution of the entropies of these models during infall will be discussed in more detail in § IIIe.

An analytic model will help to clarify the effect of NES on the core deleptonization during infall. Consider, for simplicity, models NP and NES. The former does not include NES, the

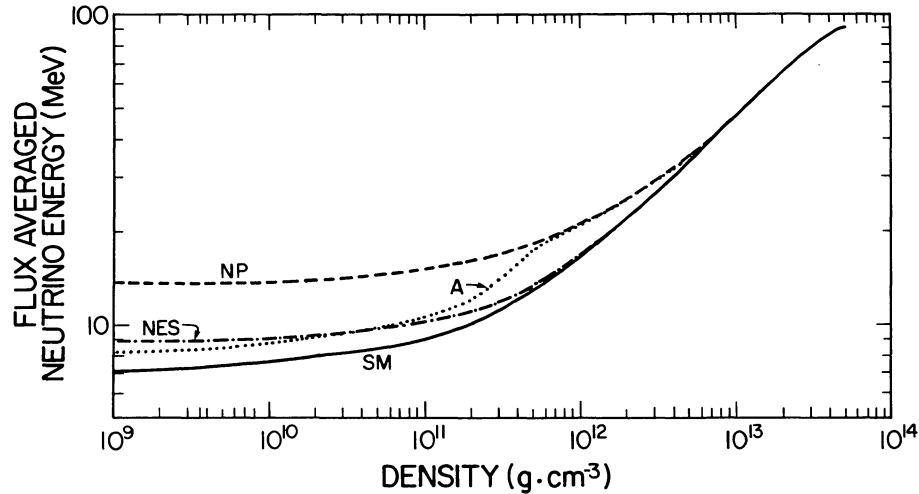


FIG. 17.—The flux-averaged neutrino energy as a function of density for stage 8 of the core infall. The dashed, dot-dash, dotted, and solid lines correspond to models NP, NES, A, and SM, respectively.

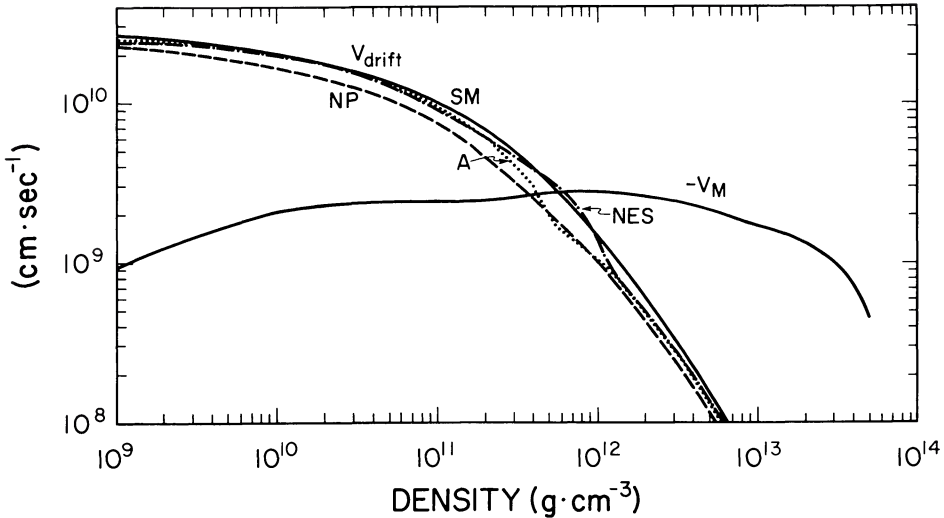


FIG. 18.—Material infall velocity (V_M) and the number-averaged neutrino drift velocity (V_{drift}) as a function of density for stage 8 of the core infall. The dashed, dot-dash, dotted, and solid lines show V_{drift} for models NP, NES, A, and SM, respectively. The matter infall velocity is approximately the same for all models at the stage of the infall, and is shown only for the standard model.

latter does. Neither model includes electron capture on nuclei. (An analysis of models A and SM, which include electron capture in nuclei, would be similar, but not so simple.) The electron capture rate on free protons is given by (e.g., Van Riper and Lattimer 1981)

$$\dot{Y}_e = -3.58 \times 10^{-3} \mu_e^5 Y_p^5 B \text{ s}^{-1}, \quad (3.7)$$

where μ_e is the electron chemical potential in MeV and B is the blocking factor. The compression rate of a given LP is (cf. eq. [3.3])

$$\dot{\rho}/\rho = 224 \rho_{10}^{1/2} / \chi \text{ s}^{-1}, \quad (3.8)$$

where $\rho_{10} = \rho(\text{g cm}^{-3})/10^{10}$, and χ is the ratio of the free-fall compression rate to the actual compression rate. Dividing equation (3.7) by equation (3.8), using

$$\mu_e = 11.1 (\rho_{10} Y_e)^{1/3} \text{ MeV}, \quad (3.9)$$

leads to the equation

$$dY_e/d\rho_{10} = -2.69 \rho_{10}^{1/6} Y_e^{5/3} Y_p \chi B, \quad (3.10)$$

which can be integrated to give

$$\begin{aligned} Y_{e_f}^{-2/3} - Y_{e_i}^{-2/3} &= 1.79 \int_i^f \rho_{10}^{1/6} \chi Y_p B \\ &\approx 1.54 \rho_{10}^{7/6} \chi Y_p B, \end{aligned} \quad (3.11)$$

where the final values (which are taken at $\rho = \rho_{\text{trap}}$) are used on the right-hand side of equation (3.11), since most of the change in Y_e occurs near these values.

Consider the LP enclosing a rest mass of $0.289 M_\odot$. The value of Y_{e_i} is 0.440 in all models for this LP. For the $0.289 M_\odot$ LP of model NP, $\rho_{\text{trap}} \approx 6.5 \times 10^{11} \text{ g cm}^{-3}$, $\chi \approx 4.0$,

$Y_p = 5.5 \times 10^{-4}$, and $B \approx 0.5$ (see Fig. 6). With these values equation (3.11) gives $Y_e = 0.368$, which is not far from the numerically computed value of 0.360 at $\rho = \rho_{\text{trap}}$ ($Y_i = 0.379$ at this time). Equilibration and some slight further deleptonization result in the numerically computed core turnaround values for Y_e and Y_l of 0.291 and 0.359, respectively. For model NES the corresponding values of the quantities on the right-hand side of equation (3.11) for the $0.289 M_\odot$ LP are $\rho_{\text{trap}} = 10^{12} \text{ g cm}^{-3}$, $\chi \approx 3.5$, $Y_p = 7.5 \times 10^{-4}$, and $B \approx 0.5$ (see Fig. 7). Equation (3.11) gives $Y_e = 0.314$, which is equal to the numerically computed value of Y_e at $\rho = \rho_{\text{trap}}$. This equality is somewhat fortuitous given the simplicity of the analytic model and the imprecision of the values used in equation (3.11) to obtain this result ($Y_i = 0.343$ at this time). Equilibration and some slight further deleptonization results in the numerically computed core turnaround values of Y_e and Y_l of 0.258 and 0.317, respectively. This example illustrates what was discussed in general terms above, namely, that NES increases the core deleptonization by increasing the values of both ρ_{trap} and Y_p . In particular, the inclusion of NES in this example increased the value of ρ_{trap} from 6.5×10^{11} to $10^{12} \text{ g cm}^{-3}$, and also increased the value of Y_p at $\rho = \rho_{\text{trap}}$, through an increase in entropy, from 5.5×10^{-4} to 7.5×10^{-4} . The latter effect is more important than the numbers indicate. Without the effect of NES on entropy, the value of Y_p at ρ_{trap} would be much smaller than the model NP value of 5.5×10^{-4} because of the reduced value of Y_e resulting from the increase in ρ_{trap} to $10^{12} \text{ g cm}^{-3}$.

A summary of the above discussion concerning the deleptonization of models with and without the inclusion of electron capture in nuclei and of NES is provided by Table 4 and Figure 19. The latter shows the lepton fraction profiles for models NP, A, NES, and SM just prior to core turnaround.

The transport of neutrinos out of the core as computed by models NP, A, NES, and SM is summarized by Figures 20 and 21. Figure 20 shows the ν_e number luminosity versus density for the different models at stage 8 of the core infall. It

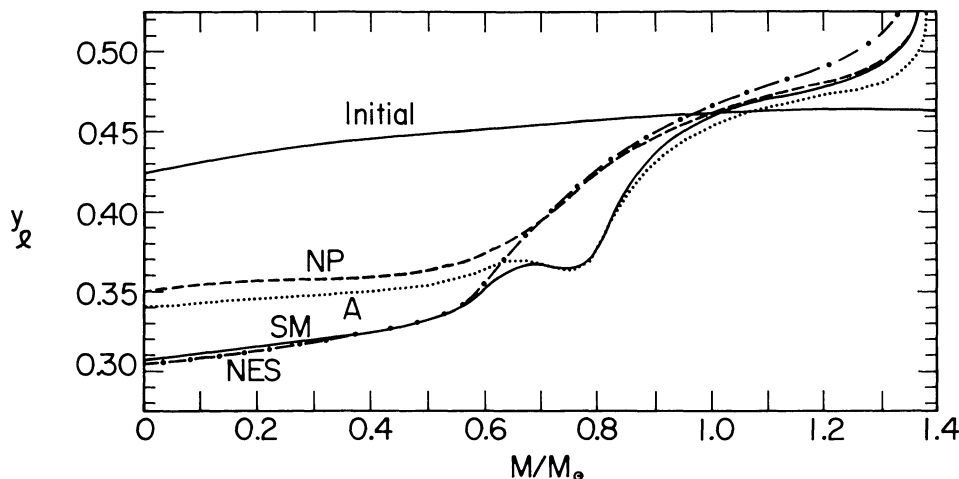


FIG. 19.—Lepton fraction profiles for models NP (dashed line), NES (dot-dash line), A (dotted line), and SM (solid line) just prior to core turnaround. The solid line labeled “initial” shows the lepton fraction profile of the initial configuration of the standard model, from which all the models were evolved.

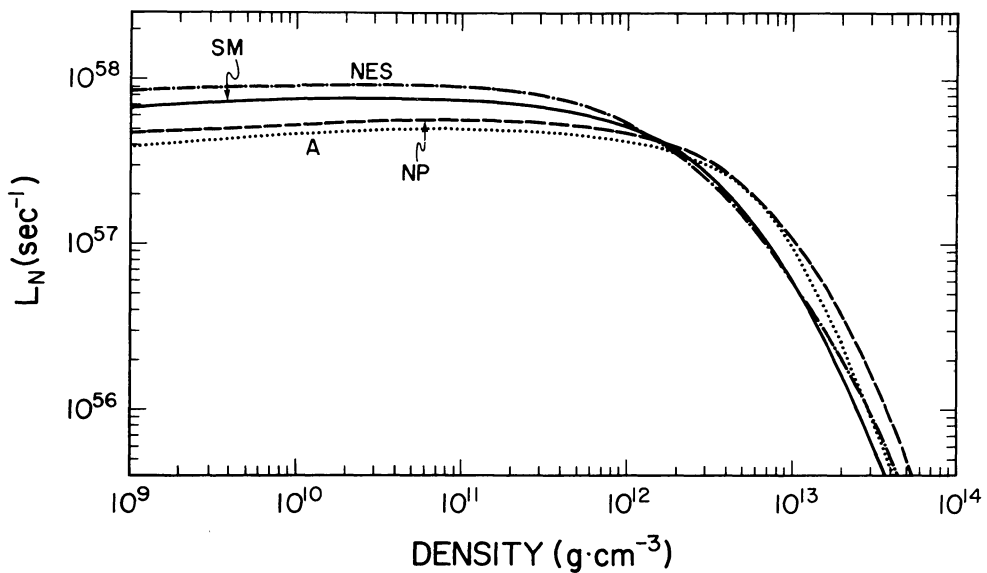


FIG. 20.—Number luminosity of ν_e 's as a function of density at stage 8 of the core infall. The dashed, dot-dash, dotted, and solid lines refer, respectively, to models NP, NES, A, and SM.

is seen that the different ν_e luminosities at this stage originate in the density region between about 4×10^{11} and 2×10^{12} g cm^{-3} . The lower boundary of this region is where NES is beginning to become significant; the upper boundary is where neutrino β -equilibrium is nearly established and the net production rate of ν_e 's by electron captures on free protons is tapering off. Despite the fact that model A is deleptonized more than model NP after infall, its neutrino number luminosity is slightly less than that of model NP at this stage of the infall. The reason is that at this stage the mass flow rate through the region of rapid electron captures on free protons is greater for model NP than for model A. At earlier stages of core infall the luminosity of model A exceeds that of model NP. As expected, including NES has a substantial effect on the number luminosity, increasing it by a factor of 2 at stage 8 of the infall whether or not electron captures on heavy nuclei are included.

Figure 21 shows the spectra of the neutrino number luminosity at the outer boundary of the core for stages 2, 5, and 8 of infall for the four models. (Stage 11 of model SM is also shown.) The tendency of the luminosity spectrum of model NP to be top-heavy is clearly evident, as is the tendency of the spectrum of model A to exhibit two peaks. In both cases the inclusion of NES tends to shift the peaks in the luminosity spectrum to lower energies.

The inset at the upper right in Figure 21 shows the ν_e number luminosity, L_N , as a function of the time at the outer boundary of the core for the four models. L_N for models A and SM exhibits an abrupt initial rise to a plateau having a value of about $1.5 \times 10^{57} \text{ s}^{-1}$, followed by another rapid rise at $t \approx 0.04$ s. The initial rise is due to the burst of ν_e 's produced at low energies (10^{10} – 10^{11} g cm^{-3}), and therefore early in the collapse, by electron captures on heavy nuclei; the second rise at $t \approx 0.04$ s occurs as the central density reaches $\sim 10^{12}$

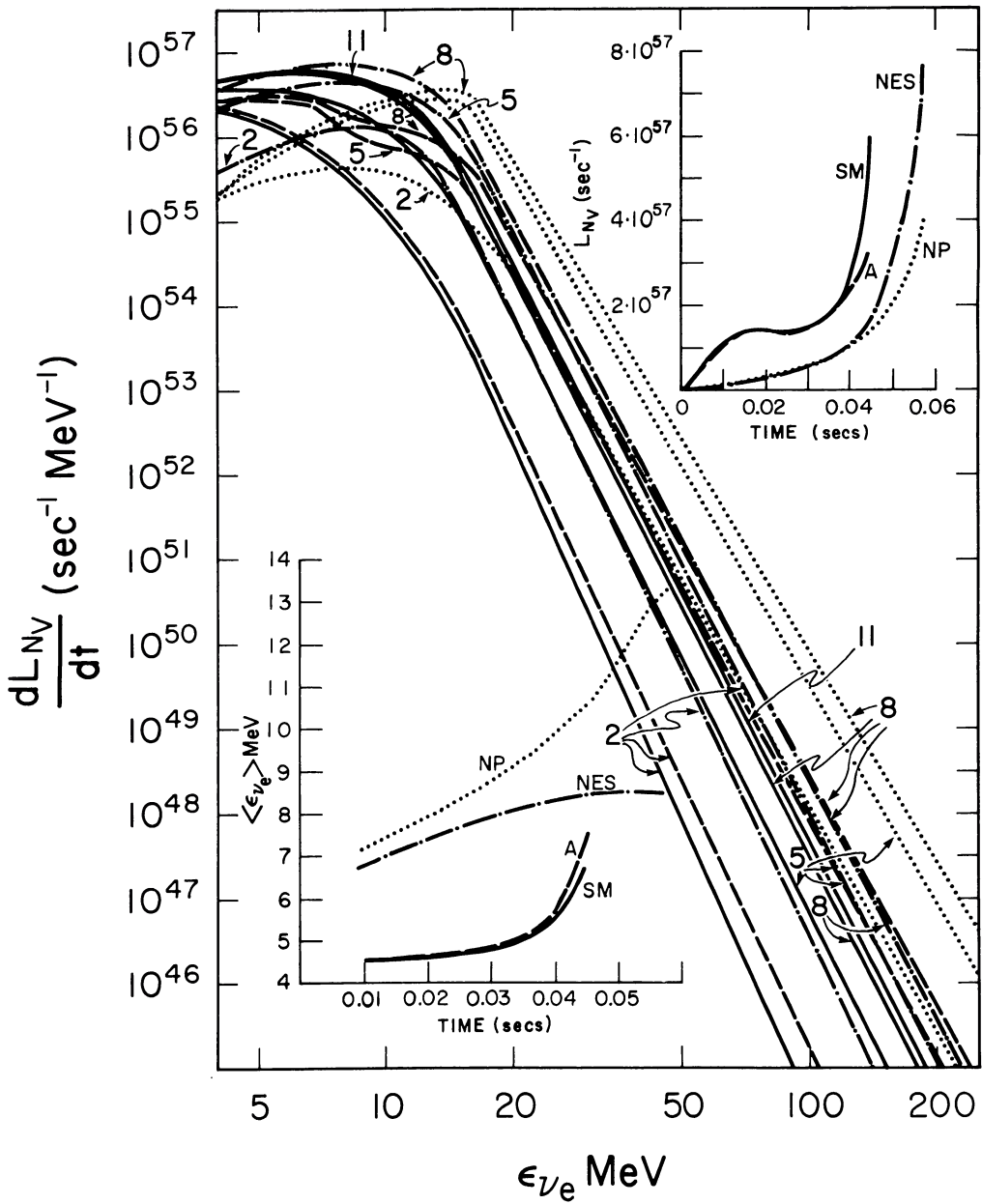


FIG. 21.—The ν_e number luminosity spectrum at the core boundary for stages 2, 5, and 8 of the core infall for models NP (dotted lines), NES (dot-dash lines), A (dashed lines), and SM (solid lines). The inset at the upper right shows the ν_e number luminosity $L_{N\nu}$ at the core boundary as a function of time up to core bounce for the above four models. The inset at the lower left shows the flux-averaged ν_e energy at the core boundary as a function of time up to core bounce for these models.

g cm^{-3} and the ν_e production rate due to electron captures on free protons becomes high. The continued increase in L_N thereafter is due mainly to the increased flow rate of matter through the region of rapid electron capture, which is a consequence of the increase in the compression rate at a given density with an increase in the Lagrangian distance. Models NP and NES, neither of which includes electron captures on heavy nuclei, do not produce a burst of ν_e 's at densities $< 10^{11} \text{ g cm}^{-3}$ and exhibit a slow initial rise in L_N . This rise becomes rapid, as in the case of the other two models, when their central densities reach $10^{12} \text{ g cm}^{-3}$. The collapse rates of models NP and NES are slower than for models A and SM

because the former lack the initial rapid decrease in Y_e arising from the burst of electron captures on heavy nuclei. About 10 ms more is required for their central densities to reach $10^{12} \text{ g cm}^{-3}$, which is why their ν_e luminosities appear displaced to the right with respect to those of models A and SM. The effect of NES on L_N becomes appreciable when the production of ν_e 's occurs near the trapping density, and therefore only after sufficient time has elapsed for the central density of the core to reach $\sim 10^{12} \text{ g cm}^{-3}$. This occurs at $t \approx 0.04$ s for models A and SM, and at $t \approx 0.05$ s for models NP and NES, and is why L_N for the models with and without NES diverge rapidly at these respective times. The effect of NES on L_N is even

larger than indicated in the figure, which shows L_N only up to core turnaround, since a neutrino produced near the trapping region requires a free flight time of about 3 ms to reach the outer core boundary. At core turnaround, therefore, many neutrinos are in transit but have not reached the core boundary. The effect of NES on L_N , which increases as core bounce approaches, is therefore not fully manifested in the figure.

The inset at the lower left in Figure 21 shows the flux-averaged ν_e energy, $\langle \epsilon_{\nu_e} \rangle$, as a function of time at the outer boundary of the core for the four models. The value of $\langle \epsilon_{\nu_e} \rangle$ for models A and SM is considerably lower than that for models NP and NES throughout the infall because of the presence in models A and SM of a significant fraction of low-energy ν_e 's produced by electron captures on heavy nuclei. The effect of NES is to lower the average energy of the ν_e 's emitted by the core, as can be seen by a comparison of models NP with NES and A with SM. As in the case of L_N , the effect of NES on $\langle \epsilon_{\nu_e} \rangle$ becomes appreciable only after sufficient time has elapsed for the ν_e 's to be produced near the trapping density. The value of $\langle \epsilon_{\nu_e} \rangle$ for models A and SM, which include electron captures on heavy nuclei, exhibits a slow rise with time before the arrival at 0.04 s of the neutrinos produced by electron captures on free protons. This is a consequence of the increase in the compression rate at a given density with an increase in the Lagrangian distance. The result of this is that zones of greater Lagrangian distances are further from β -equilibrium at a given density in the density range where electron captures on heavy nuclei are occurring. For example, at $\rho = 5 \times 10^{10}$ g cm⁻³ the electron capture rate is dominated by captures on heavy nuclei, and the mass fraction of heavy nuclei decreases slightly during the collapse from 0.9 at stage 4 to 0.84 at stage 10, as shown in Figure 3. The energy available for captures on heavy nuclei, $\Delta_A = \mu_e - \hat{\mu} - \Delta$ (see Appendix C), increases as the collapse proceeds, being 4.56 MeV at stage 4 and 6.18 MeV at stage 10. Taking into account the slight reduction in the heavy-nucleus mass fraction in going from stage 4 to stage 10, and the fact that the capture rate on heavy nuclei is proportional to Δ_A^4 , to first order, the capture rate at stage 10 is about a factor of 3 larger than at stage 4. According to Figure 12, this is approximately how much faster the compression rate is at stage 10 than at stage 4.

d) Emergent Neutrino Spectrum

The evolution of the emergent electron-type neutrino luminosity spectrum is shown in Figure 22. The spectrum after stage 11 of the infall remains essentially unchanged until core bounce. Comparison of this figure with the corresponding figure (Fig. 3) in Bowers and Wilson (1982b) shows that the neutrino spectrum calculated here asymptotically peaks at a lower energy (~ 7.5 MeV) than that given by the Bowers and Wilson calculation (~ 9 MeV). Given the crudeness of the energy zoning, however, this energy difference may not be significant.

e) Entropy Change

A number of authors (Arnett 1980; Epstein and Pethick 1981; Van Riper and Lattimer 1981; Bludman, Lichtenstadt, and Hayden 1982) have discussed the change in the entropy of

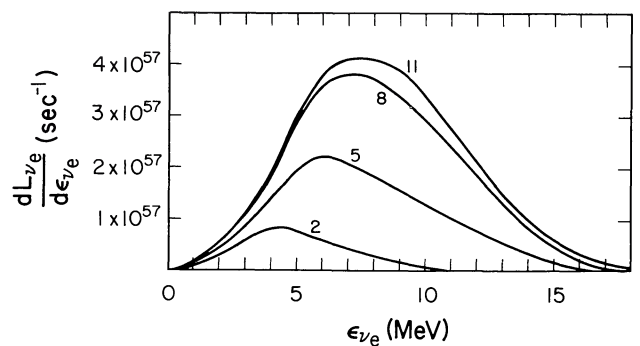


FIG. 22.—The luminosity spectrum of the ν_e 's leaving the core boundary at stages 2, 5, 8, and 11 of the infall of the standard model.

the core during the infall stage of core collapse in terms of the expression

$$kT\dot{s} = (\mu_e - \hat{\mu} - \mu_\nu)(-\dot{Y}_e) + (\mu_\nu - \langle \epsilon_\nu \rangle_{\text{escape}})(-\dot{Y}_l), \quad (3.12)$$

where s is the entropy per baryon divided by the Boltzmann constant k , $\langle \epsilon_\nu \rangle_{\text{escape}}$ is the average energy of the escaping ν_e 's and the subscript ν refers to electron-type neutrinos. Other neutrino types have negligible effects on the entropy during core infall. A different formulation is preferred here, which is more compatible with the quantities computed by the computer code and which recognizes that the ν_e distribution is not *a priori* assumed to be an equilibrium distribution (i.e., Fermi-Dirac). Neutrinos do not equilibrate with matter until densities substantially higher than ρ_{trap} are reached. At lower densities, therefore, the ν_e distribution is not necessarily a Fermi-Dirac distribution, and, if not, the ν_e thermodynamic variables, such as μ_ν , are not defined. On the other hand, matter is always equilibrated with respect to the instantaneous value of Y_e , so, confining our attention to the entropy of the matter alone, to which s will hereafter refer, we can write (e.g., Imshennik and Chechetkin 1971)

$$kT\dot{s} = \dot{q} + (\mu_e - \hat{\mu})(-\dot{Y}_e), \quad (3.13)$$

where q is the neutrino-to-matter energy transfer rate per baryon. A useful expression for q is

$$\dot{q} = -\langle \epsilon_\nu \rangle_{\text{emit}}(-\dot{Y}_e)_{\text{emit}} + \langle \epsilon_\nu \rangle_{\text{abs}}(\dot{Y}_e)_{\text{abs}} - \langle \Delta \epsilon_\nu \rangle_{\text{scat}} r_{\text{scat}}, \quad (3.14)$$

where $\langle \epsilon_\nu \rangle_{\text{emit}}$ and $\langle \epsilon_\nu \rangle_{\text{abs}}$ are the average energies of the emitted and absorbed ν_e 's, $(\dot{Y}_e)_{\text{emit}}$ and $(\dot{Y}_e)_{\text{abs}}$ are the rates of change of Y_e due to emission and absorption, and $\langle \Delta \epsilon_\nu \rangle_{\text{scat}}$ and r_{scat} are, respectively, the mean ν_e energy change per ν_e - e scattering and the ν_e - e scattering rate per baryon. If ν_e absorption is unimportant, equations (3.13) and (3.14) can be combined to give

$$kT\dot{s} = (\mu_e - \hat{\mu} - \langle \epsilon_\nu \rangle_{\text{emit}})(-\dot{Y}_e) - \langle \Delta \epsilon_\nu \rangle_{\text{scat}} r_{\text{scat}}. \quad (3.15)$$

For electron captures occurring at densities $\rho \ll \rho_{\text{trap}}$, the last term in equation (3.15) is approximately zero, and the analysis given by Van Riper and Lattimer (1981) applies here (with their $\langle \epsilon_\nu \rangle_{\text{escape}}$ replaced by $\langle \epsilon_\nu \rangle_{\text{emit}}$, which, under these conditions, is equivalent). Electron captures on heavy nuclei produce ν_e 's with mean energies given by $\langle \epsilon_\nu \rangle_{\text{emit}} = \frac{2}{3}(\mu_e - \hat{\mu} - \Delta)$, where Δ is the excitation energy in which the daughter nucleus is produced, so that

$$kT\dot{s} = [\frac{2}{3}(\mu_e - \hat{\mu}) + \frac{2}{3}\Delta](-\dot{Y}_e) \quad (3.16)$$

and, since all terms are positive, s increases. For electron captures on free protons, however, $\langle \epsilon_\nu \rangle_{\text{emit}} = \frac{5}{6}\mu_e$ (neglecting the small neutron-proton mass difference), and

$$kT\dot{s} = (\frac{1}{6}\mu_e - \hat{\mu})(-\dot{Y}_e), \quad (3.17)$$

so that s decreases if $\mu > \frac{1}{6}\mu_e$, which is the case unless $Y_e \gtrsim 0.44$.

Figure 23 gives the entropy for the LPs enclosing rest masses of 0.00544, 0.289, and $0.696 M_\odot$ as a function of the densities of these points during infall for models AD, NP, NES, A, and SM. Since shocks are absent during the core infall, the entropy change of the matter in the core during this

stage is due entirely to the weak interactions. It is essential that this entropy change be computed accurately, since the entropy change has a sensitive influence on the core composition and therefore on the β -rates. A necessary condition for an accurate computation is that there be no change in the core entropy during infall if the weak interactions are turned off. As a test of the computer code, model AD was computed. This model was the same as model SM except that all weak interactions were turned off. Although the hydrodynamic equations were not differenced explicitly to conserve entropy under nondissipative conditions, it is seen that the entropy remains constant to within 1% or 2% for model AD.

To provide for a more detailed analysis of the entropy changes shown in Figure 23, Figure 24 gives, for the $0.289 M_\odot$ LP of models NP and SM, the following quantities, which together comprise the right-hand side of equation (3.13): (1) $\langle \epsilon_\nu \rangle_{\text{eff}}$, defined by

$$\langle \epsilon_\nu \rangle_{\text{eff}} = \{ \langle \epsilon_\nu \rangle_{\text{emit}} (-\dot{Y}_e) - \langle \epsilon_\nu \rangle_{\text{abs}} (\dot{Y}_e)_{\text{abs}} \} / (-\dot{Y}_e), \quad (3.18)$$

which is equal to $\langle \epsilon_\nu \rangle_{\text{emit}}$ when ν_e absorption is unimportant and less than $\langle \epsilon_\nu \rangle_{\text{emit}}$ otherwise; (2) $\epsilon_0 = \mu_e - \hat{\mu}$, which is the

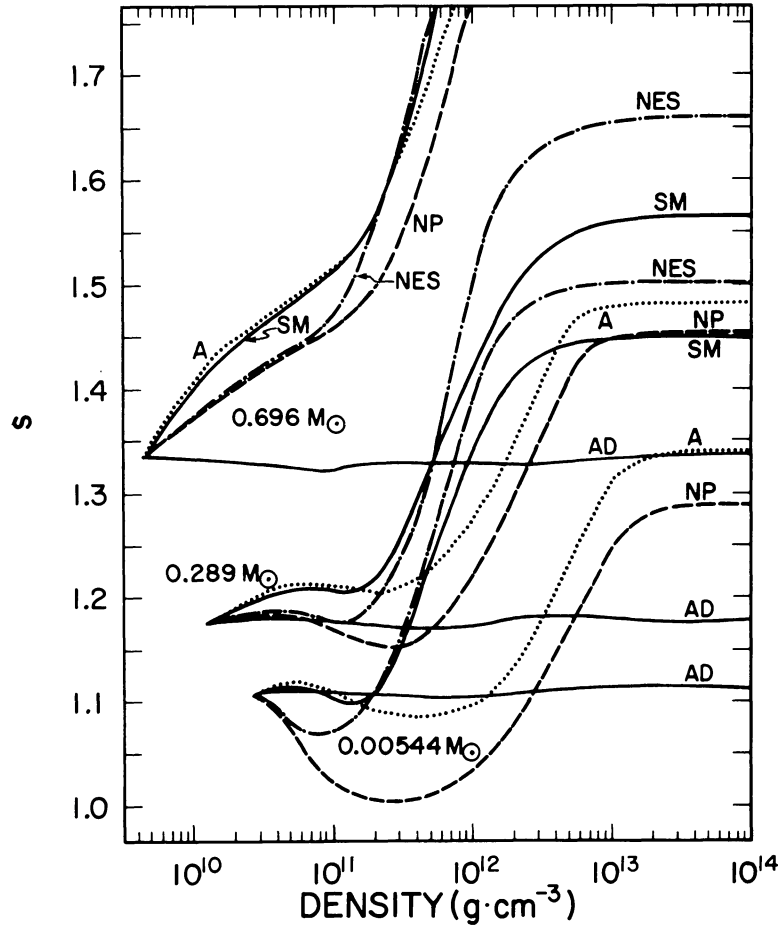


FIG. 23.—Entropy as a function of density for Lagrangian points enclosing rest masses of 0.00544, 0.289, and $0.696 M_\odot$, respectively, for the core infall of models NP (dashed line), NES (dot-dash line), A (dotted line), AD (solid line), and SM (solid line).

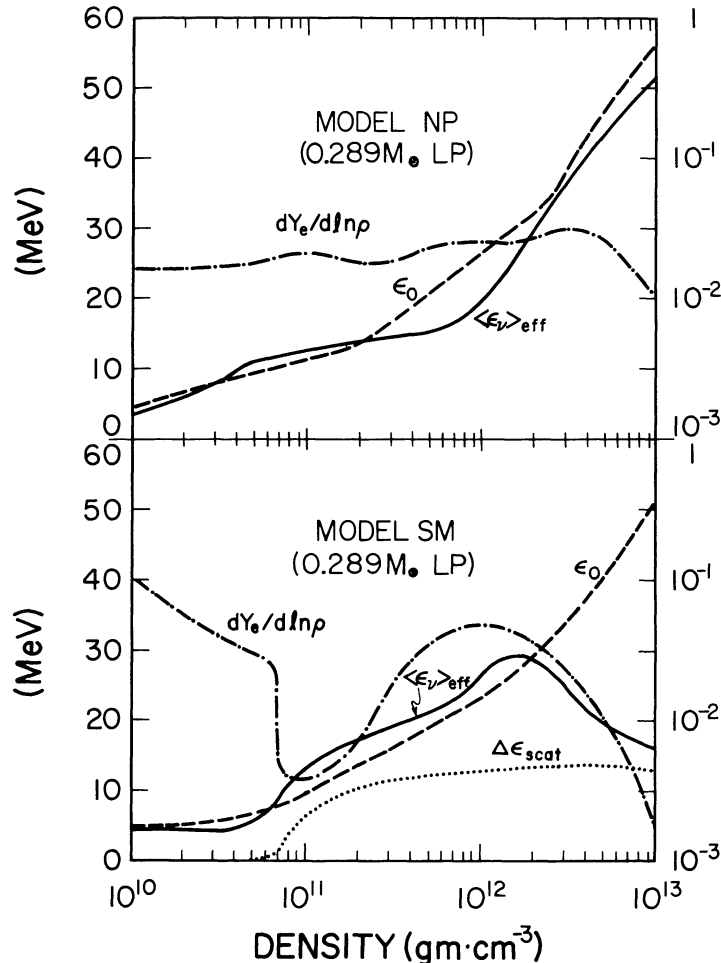


FIG. 24.—The quantities $\langle \epsilon_\nu \rangle_{\text{eff}}$ (solid line), ϵ_0 (dashed line), and $dY_e/d \ln \rho$ (dot-dash line) as a function of density for the Lagrangian point enclosing a rest mass of $0.289 M_\odot$ for the core infall of model NP and the standard model. Also shown is the quantity $\Delta \epsilon_{\text{scat}}$ for the standard model. These quantities are defined in the text.

value of the neutrino energy such that a ν_e created with this energy would result in no entropy change for the matter; (3) $\Delta_{\text{scat}} = -(\Delta \epsilon_\nu)_{\text{scat}} r_{\text{scat}} / (-\dot{Y}_e)$, which is equivalent to the negative of the mean energy change of the neutrinos due to NES per created neutrino; and (4) $dY_e/d \ln \rho$, which is a measure of the extent to which these β -processes occur per unit change in $d\rho/\rho$.

Consider first model NP, which omits both electron captures on nuclei and NES. Figure 23 shows that following a small entropy increase up to $\rho \approx 3 \times 10^{10} \text{ g cm}^{-3}$, resulting from a value of $Y_e > 0.44$, the $0.289 M_\odot$ LP of model NP undergoes an entropy decrease up to a density of about $2 \times 10^{11} \text{ g cm}^{-3}$, followed by a substantial entropy increase to about $10^{13} \text{ g cm}^{-3}$, after which the entropy remains nearly constant. This is reflected in Figure 24 by the fact that, consistent with the discussion of equation (3.17), $\langle \epsilon_\nu \rangle_{\text{eff}}$ is larger than ϵ_0 between 3×10^{10} and $2 \times 10^{11} \text{ g cm}^{-3}$. Therefore, in this density range, ν_e emission cools the matter. At higher densities ν_e absorption becomes important, $\langle \epsilon_\nu \rangle_{\text{eff}}$ falls below ϵ_0 , and the net effect of the β -processes is to heat the matter. Above about $10^{13} \text{ g cm}^{-3}$ the ν_e 's are almost com-

pletely equilibrated with the matter and $dY_e/d \ln \rho$ becomes very small.

For model SM, electron captures on nuclei predominate up to densities of about $7 \times 10^{10} \text{ g cm}^{-3}$ for the $0.289 M_\odot$ LP, and, consistent with the discussion of equation (3.16), $\langle \epsilon_\nu \rangle_{\text{eff}}$ (which is equal to $\langle \epsilon_\nu \rangle_{\text{emit}}$ in this density range) is less than ϵ_0 because of the neutron-proton chemical potential difference and the daughter excitation energy that must be paid. The neutrino emission therefore heats the matter in this density range. Above $7 \times 10^{10} \text{ g cm}^{-3}$ electron captures occur on free protons and the matter entropy decreases, for the reasons discussed above for model NP, until NES becomes important at about $10^{11} \text{ g cm}^{-3}$. The downscattering in energy of both the neutrinos created locally by electron captures and the neutrinos transported from interior regions results in a substantial value of Δ_{scat} and a net heating of the matter. The downscattering in energy of neutrinos that would otherwise have a tendency to be absorbed delays the onset of significant neutrino absorption, and $\langle \epsilon_\nu \rangle_{\text{eff}}$ remains greater than ϵ_0 for a density an order of magnitude higher than in the case of model NP. Owing to the effects of NES, Y_e undergoes a

considerably greater decrease for model SM than for model NP. Because of this, the net entropy increase of model SM is considerably greater than for model NP.

Figure 25 shows the entropy profiles of the standard model for various stages of the infall. The shapes of the profiles can be understood from the preceding discussion. For each of the stages shown beyond stage 0, the entropy is increased above that of stage 0 from the outer core boundary to the heavy-nucleus closure density, marked by the upward-pointing arrow, owing to the heating effect of electron captures on heavy nuclei. The entropy dips because of electron captures on free protons from the upward-pointing arrow to the downward-pointing arrow, the latter marking the onset of the neutrino-trapping region, which is approximately where NES becomes important. In the neutrino-trapping region (to the left of the

downward-pointing arrow) the entropy shows a substantial increase. The net change in the dimensionless entropy s is about 0.35 throughout the inner core of the standard model at the end of infall. This value of the entropy change is consistent with the original prediction of Bethe *et al.* (1979).

The entropy profiles of models NP, A, and NES at stage 10 of the infall are also shown in Figure 26. The entropy increase of models NP and A during infall is less than that of the standard model, because of the absence of NES and the consequent smaller degrees of deleptonization. With the absence of electron captures on nuclei, the entropy increase of model NES is slightly greater than that of the standard model. Both undergo about the same degree of deleptonization, but the entropy decrease of a given LP below the trapping density in model NES is more than made up for by the large entropy

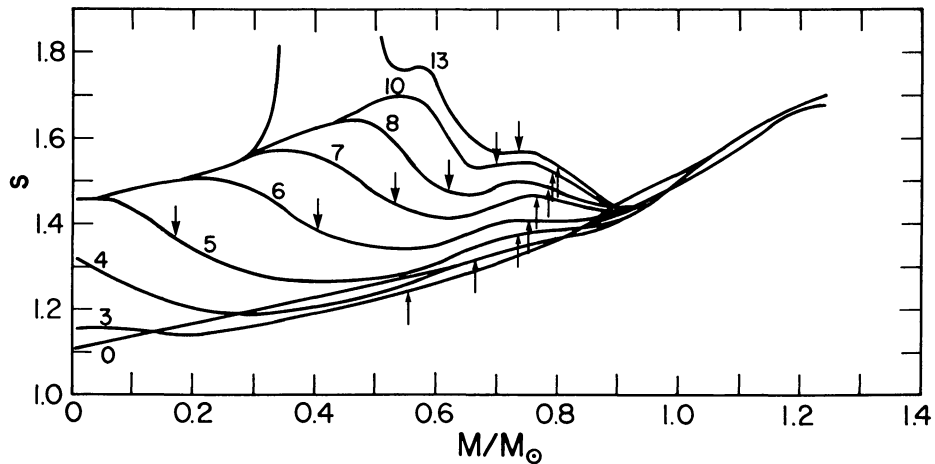


FIG. 25.—The dimensionless entropy per baryon, $s = S/kN_B$, as a function of the enclosed rest mass for the indicated stages of the core infall of the standard model. The upward-pointing arrows denote the Lagrangian points at which the electron captures on nuclei are cut off. The downward-pointing arrows denote the Lagrangian points at which ν_e 's first become trapped.

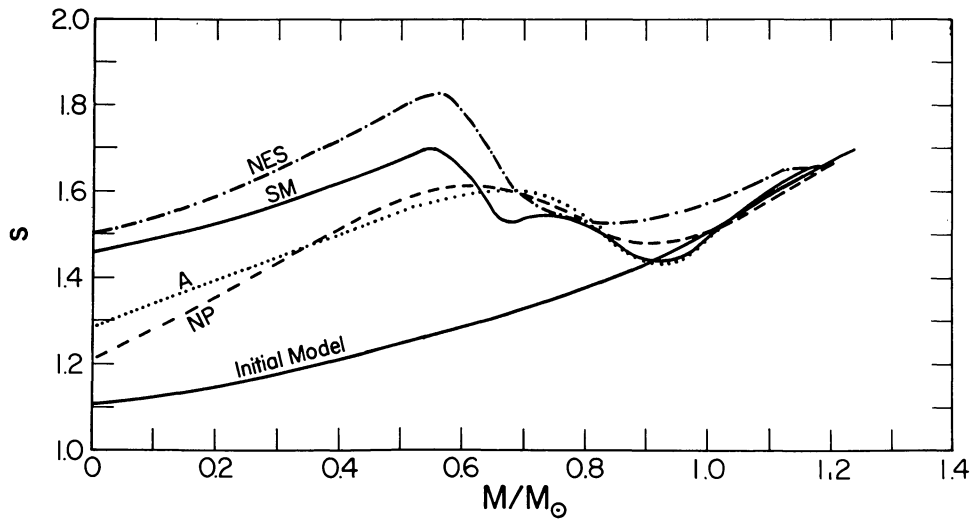


FIG. 26.—The dimensionless entropy per baryon, $s = S/kN_B$, as a function of the enclosed rest mass for stage 10 of models NP (dashed line), NES (dot-dash line), A (dotted line), and SM (solid line). Also shown is the dimensionless entropy per baryon for the initial configuration of the standard model (from which all the models were evolved).

increase above the trapping density. This is because a greater percentage of the electron captures occur above the trapping density in this model.

f) Hydrodynamics

i) Adiabatic Indices

The appropriate “adiabatic index” to consider in a discussion of the hydrodynamics of the core infall is the effective adiabatic index

$$\Gamma_E = \left(\frac{\partial \ln P}{\partial \ln \rho} \right)_\xi, \quad (3.19)$$

since the deviation of its value from $4/3 + O(P/\rho c^2)$ required for neutral stability is a measure of the force imbalance that develops during the collapse. It is also the quantity most convenient for use in a comparison with self-similar solutions. The subscript ξ specifies that the derivative is to be taken with respect to a comoving fluid element. “Effective adiabatic index” is a misnomer, since a fluid element is not in general compressed adiabatically during core infall. “Effective adiabatic index” has become the conventional appellation for equation (3.19), however, so it will be used here. It is convenient to regard P as a function of ρ , the entropy s , and the abundance fractions Y_i , and expand equation (3.19) as

$$\begin{aligned} \Gamma_E = & \left(\frac{\partial \ln P}{\partial \ln \rho} \right)_{s, Y_i} + \left(\frac{\partial \ln P}{\partial \ln s} \right)_{\rho, Y_i} \left(\frac{\partial \ln s}{\partial \ln \rho} \right)_\xi \\ & + \sum_i \left(\frac{\partial \ln P}{\partial \ln Y_i} \right)_{\rho, s} \left(\frac{\partial \ln Y_i}{\partial \ln \rho} \right)_\xi. \end{aligned} \quad (3.20)$$

The first term is frequently denoted by Γ_1 (e.g., Clayton 1968) and depends only on the state of the matter (through the equation of state). The other terms depend on the rate of change of s and the Y_i 's along the particular collapse trajectory of the fluid element in question.

Figure 27 gives Γ_1 as a function of density in the standard model for stage 10 of the core infall. Van Riper and Lattimer (1981) discuss the behavior of Γ_1 , which they refer to as Γ_{EOS} , in a similar context, and their discussion is applicable here. To summarize, at low densities (less than a few times 10^{11} g cm $^{-3}$) Γ_1 is depressed below $4/3$ because the core is skirting the heavy-element- α -particle phase transition; at densities between a few times 10^{11} g cm $^{-3}$ and about 10^{13} g cm $^{-3}$ the reduced value of Y_e and the increased value of s , due to electron capture and neutrino equilibration, respectively, result in an increased abundance of free neutrons (see Fig. 3) whose $5/3$ contribution to the value of Γ_1 raises it above $4/3$; at densities between about 10^{13} g cm $^{-3}$ and nuclear density (2.6×10^{14} g cm $^{-3}$ in the equation of state of Lamb *et al.* 1978, 1981), a combination of strong interactions among the baryons and Coulomb lattice effects, both attractive, cause Γ_1 to decrease below $4/3$ again; above nuclear density the equation of state stiffens, primarily because of nucleon degeneracy, and Γ_1 rises rapidly above $4/3$.

The second term on the right-hand side of equation (3.20) is very small during core infall, since P is not a sensitive

function of s in the low-entropy core [$(\partial \ln P / \partial \ln s)_{\rho, Y} < 0.2$], and the rate of entropy increase of the core during infall is modest [$(\partial \ln s / \partial \ln \rho)_\xi < 0.1$]. The second term of equation (3.20) is therefore at most 0.02, approaching this value in the density range between a few times 10^{11} g cm $^{-3}$ and a few times 10^{12} g cm $^{-3}$, where most of the entropy increase occurs.

Approximate expressions for the third term on the right-hand side of equation (3.20) can be obtained by noting that below nuclear density the pressure of the infalling core is dominated by the leptons, so that $P \propto (Y_e \rho)^{4/3} + 2^{1/3} (Y_\nu \rho)^{4/3}$, where ν denotes electron-type neutrinos. Then in this approximation,

$$\begin{aligned} & \sum_i \left(\frac{\partial \ln P}{\partial \ln Y_i} \right)_{\rho, s} \left(\frac{\partial \ln Y_i}{\partial \ln \rho} \right)_\xi \\ &= \frac{4}{3} \frac{1}{1 + 2^{1/3} (Y_\nu / Y_e)^{4/3}} \left(\frac{\partial \ln Y_e}{\partial \ln \rho} \right)_\xi \\ &+ 2^{1/3} \left(\frac{Y_\nu}{Y_e} \right)^{1/3} \left(\frac{\partial \ln Y_\nu}{\partial \ln \rho} \right)_\xi. \end{aligned} \quad (3.21)$$

In the density region between 10^{10} and 10^{11} g cm $^{-3}$, the electron capture rate on heavy nuclei dominates the total electron capture rate, and $Y_\nu \approx 0$, since this density region lies well below ρ_{trap} . Equation (3.21) then simplifies to

$$\sum_i \left(\frac{\partial \ln P}{\partial \ln Y_i} \right)_{\rho, s} \left(\frac{\partial \ln Y_i}{\partial \ln \rho} \right)_\xi \approx \frac{4}{3} \left(\frac{\partial \ln Y_e}{\partial \ln \rho} \right)_\xi. \quad (3.22)$$

The quantity $(\partial \ln Y_e / \partial \ln \rho)$ can be expressed as $-\tau_\rho / \tau_{e\text{-cap}}$, where τ_ρ and $\tau_{e\text{-cap}}$ are the e -folding times for $\rho(t)$ and $Y_e(t)$ along a fluid element trajectory, respectively, and are shown in Figure 12. The minimum value of $-\tau_\rho / \tau_{e\text{-cap}}$ in the above density range is ~ -0.075 and occurs at a density of about 10^{11} g cm $^{-3}$ at stage 10 of the infall. This gives a value of -0.1 to expression (3.22) and, neglecting the second term in equation (3.20), depresses Γ_E below Γ_1 by this value at the above density, in reasonable agreement with Figure 27.

At densities above 2×10^{12} g cm $^{-3}$ the neglect of neutrino transport becomes a good approximation. Then $dY_\nu|_\xi = -dY_e|_\xi$, and equation (3.21) then simplifies to

$$\begin{aligned} & \sum_i \left(\frac{\partial \ln P}{\partial \ln Y_i} \right)_{\rho, s} \left(\frac{\partial \ln Y_i}{\partial \ln \rho} \right)_\xi \approx \frac{4}{3} \frac{1 - 2^{1/3} (Y_\nu / Y_e)^{1/3}}{1 + 2^{1/3} (Y_\nu / Y_e)^{4/3}} \\ & \times \left(\frac{\partial \ln Y_e}{\partial \ln \rho} \right)_\xi. \end{aligned} \quad (3.23)$$

The quantity $(\partial \ln Y_e / \partial \ln \rho)$ takes another minimum value, numerically equal to about -0.15 at stage 10 of the infall, at a density of a few times 10^{12} g cm $^{-3}$ where the rate of electron capture on free protons peaks. At this density $Y_e \approx 0.3$ and $Y_\nu \approx 0.044$, which, with the above value of -0.15 for $(\partial \ln Y_e / \partial \ln \rho)$, gives expression (3.23) a value of about -0.06 . With a value of about -0.02 for the second term in expression (3.20), Γ_E should be depressed below Γ_1 by about -0.04 , again in reasonable agreement with Figure 27.

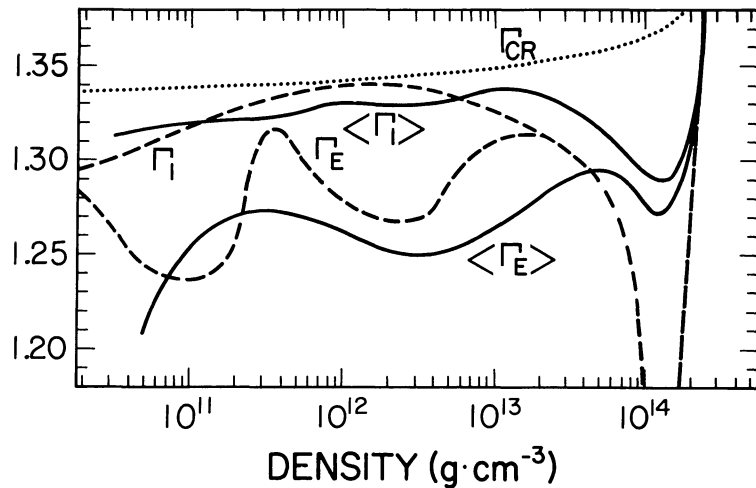


FIG. 27.—The dashed curves give the adiabatic index Γ_1 and the effective adiabatic index $\langle \Gamma_E \rangle$ as a function of density for stage 10 of the core infall of the standard model. The solid curves give Γ_1 and $\langle \Gamma_E \rangle$ mass-averaged over the inner core of the standard model as a function of the central density during the core infall. The dotted line gives the critical index for neutral stability as given by the theory of relativistic polytropes.

Figure 27 also shows Γ_{CR} at stage 10 of the infall, where Γ_{CR} is the critical index for neutral stability. Values of $\Gamma_{\text{CR}} = 4/3 + 2.78P/\rho c^2$ (ρ is the rest mass density). This relation was taken from the theory of relativistic polytropes (Chandrasekhar 1964, 1965; see Van Riper 1979 for more discussion and further references). By increasing the value of Γ_{CR} above 4/3, the effect of GR is to speed up the infall at high densities, increase the density of core bounce, and reduce the size of the inner core.

ii) Infall of the Inner and Outer Core

Yahil and Lattimer (1982) and Yahil (1983) have shown that if the equation of state for the matter in the core during infall can be expressed by the polytropic relation

$$P = \kappa \rho^\gamma, \quad (3.24)$$

where κ and γ are constant in both space and time, $6/5 < \gamma < 4/3$, and GR effects are negligible, then self-similar solutions (SSSs) for the core during infall can be found. These SSSs should describe the hydrodynamics of the core infall after sufficient time has elapsed for transients produced by the initial conditions of the core to become small. The quantity γ should be identified with $\Gamma'_E = \Gamma_E - (\Gamma_{\text{CR}} - 4/3)$ which, according to Figure 23, is definitely not a constant in space and time for model SM; nor is κ a constant, being a function of both s and the Y_i . Nevertheless, the hydrodynamics of the core infall appear to be in qualitative accord with the SSSs, and the latter therefore provide a convenient framework for describing the numerical results.

The division of the collapsing core into an inner and outer core, each of which undergoes different hydrodynamics, and the two of which are separated by the mass zone having the greatest infall velocity, is shown in Figure 28. In agreement with the results of the SSSs for $\gamma < 4/3$, the mass, M_{IC} , of the inner core decreases with time. The decrease is from 0.87 to 0.6 M_\odot , most of which occurs as the central density increases from about 10^{13} to about $7 \times 10^{13} \text{ g cm}^{-3}$. The homologous

mass, M_H (for which $u \propto r$), and the sonic mass, M_S (which is the mass inside the innermost mass shell moving at the sonic velocity), are also shown in Figure 28. The homologous mass is difficult to estimate, since the homology is only roughly satisfied and the choice of the mass zone at which it breaks down is a little arbitrary.

The degree of homology of the inner zones during infall is shown in Figure 29. According to the SSSs, exact homology is to be expected only when $\Gamma'_E = 4/3$. The figure indicates that the inner core undergoes two major readjustments of homology during infall, the first between stages 0 and 2, and the second between stages 4 and 6. During each of these readjustments the homologous mass shrinks substantially. The central densities at which these two readjustments occur coincide approximately with the densities of the two minima of Γ_E shown in Figure 27. Following each of these readjustments the homologous mass expands. (Another readjustment of the core appears to be starting at stage 9 of the infall as GR effects increase Γ_{CR} and strong interactions and lattice effects reduce Γ_E . The stiffening of the equation of state occurs so soon thereafter that the readjustment has no chance to complete itself.)

For the outer core, the SSSs establish a number of asymptotic relations. Two of these are

$$ur^{(\Gamma'_E-1)/(2-\Gamma'_E)} = F_1(t), \quad (3.25)$$

$$\rho r^{2/(2-\Gamma'_E)} = F_2(t), \quad (3.26)$$

where F_1 and F_2 are functions of time but not of r . The $\Gamma'_E = 4/3$ limits of these relations have been discussed by Brown, Bethe, and Baym (1982) and were given by them in the form

$$u^2 r = 10^{26} \text{ cm}^3 \text{ s}^{-2}, \quad (3.27)$$

$$\rho r^3 = 3 \times 10^{31} \text{ g}. \quad (3.28)$$

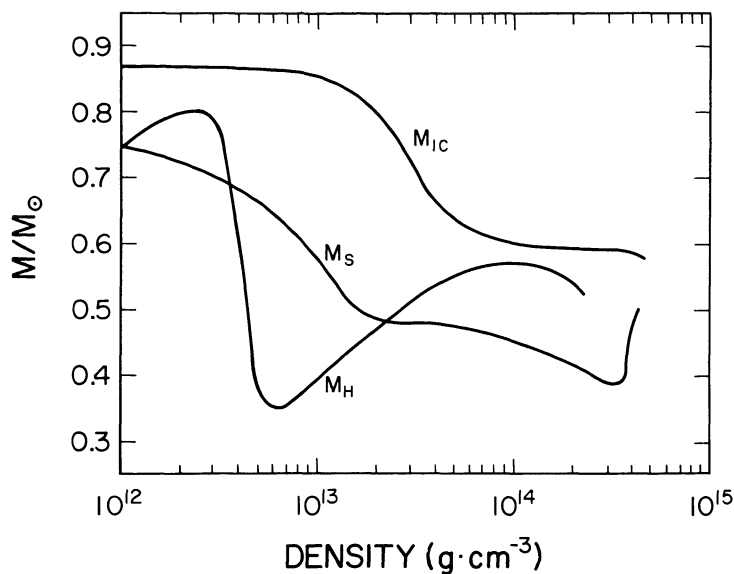


FIG. 28.—The inner-core mass M_{IC} , the sonic mass M_S , and the homologous mass M_H as a function of the central density during the core infall of the standard model. The inner-core mass is the rest mass enclosed by the Lagrangian point having the greatest inward velocity; the sonic mass is the rest mass enclosed by the innermost Lagrangian point moving with the sonic velocity with respect to the Eulerian frame; and the homologous mass is the rest mass that is collapsing in such a way that $v \propto r$, approximately.

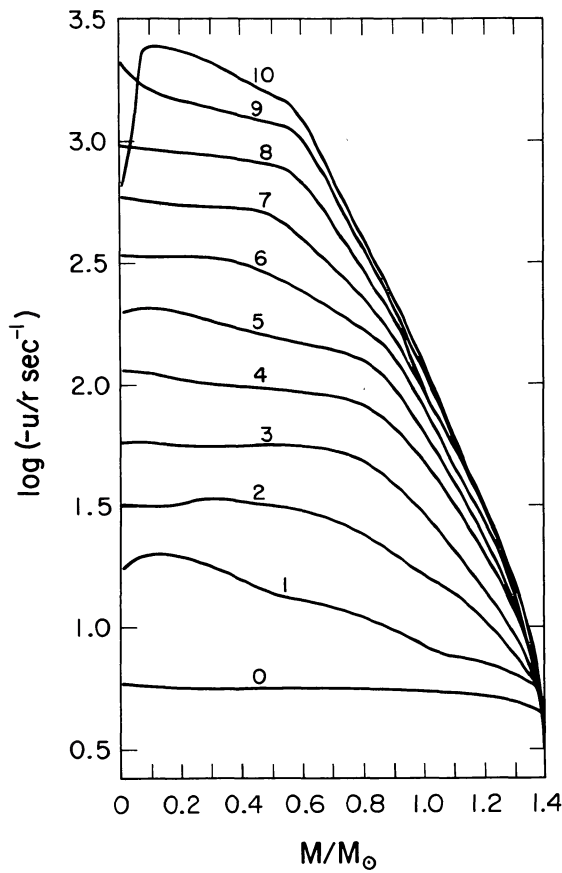


FIG. 29.—The ratio of the negative of the matter velocity to the radius r as a function of the enclosed rest mass for stages 0–10 of the core infall of the standard model.

For $\Gamma'_E < 4/3$, it is evident from equations (3.25) and (3.26) that the SSSs give both $u^2 r$ and ρr^3 as increasing with r . The quantity $u^2 r$ is shown in Figure 30 as a function of the enclosed rest mass for various stages of the infall of the standard model. By stage 10 it is seen that $u^2 r$ increases by less than a factor of 2 from 0.6 to 1 M_\odot , in qualitative agreement with the SSSs, but decreases beyond 1 M_\odot . The latter behavior suggests that insufficient time has elapsed for the hydrodynamics of this outer part of the core to become self-similar. The quantity ρr^3 is shown in Figure 31 as a function of enclosed rest mass for the same stages of core infall as shown in Figure 30. By stage 10 both the slow increase in this quantity from 0.6 to 1.2 M_\odot and the hump at the outer part of the inner core ($\sim 0.4 M_\odot$) are in qualitative agreement with the SSSs.

Two other consequences of the SSSs are that the ratio of the infall velocity of matter in the outer core to the local sound speed should approach a constant value of about 2.5, and that the ratio of the infall velocity of matter in the outer core to the free-fall velocity should approach a constant value of about 0.6. (The exact values for these two ratios depend on the values of Γ_E .) Both of these ratios are shown in Figure 32 for stages 8 and 10 of the infall of the standard model. It is evident that a flow approximating the flow given by the SSSs is developing in the outer core between 0.6 and 1 M_\odot , but not yet in the region beyond.

IV. SUMMARY AND CONCLUSIONS

This paper has been concerned with the core infall stage of the final evolution of a 10 M_\odot star as given by an accurate and detailed numerical model. A brief summary of the results of this model follows.

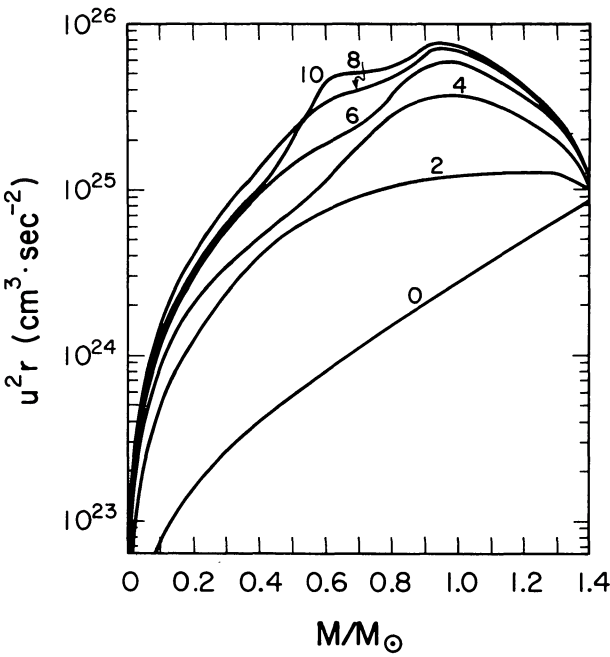


FIG. 30

FIG. 30.—The quantity $u^2 r$ as a function of the enclosed rest mass for stages 0, 2, 4, 6, 8, and 10 of the core infall of the standard model; u denotes the matter velocity and r the radius.

FIG. 31.—The quantity $\rho_{10} r_7^3 = (\rho/10^{10})(r/10^7)^3$, with units of 10^{31} g, as a function of the enclosed rest mass for stages 0, 2, 4, 6, 8, and 10 of the core infall of the standard model. During the later stages of the infall the density varies roughly as $1/r^3$ throughout the outer core, except for a region of about $0.15 M_\odot$ at the outer edge of the core.

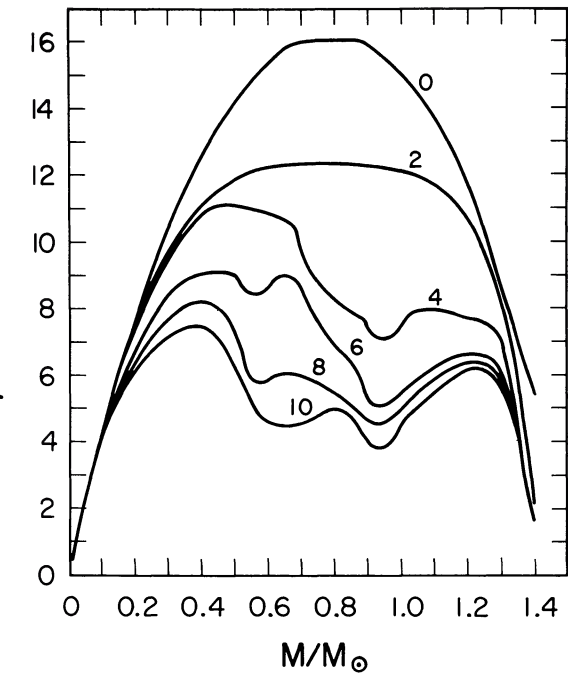


FIG. 31

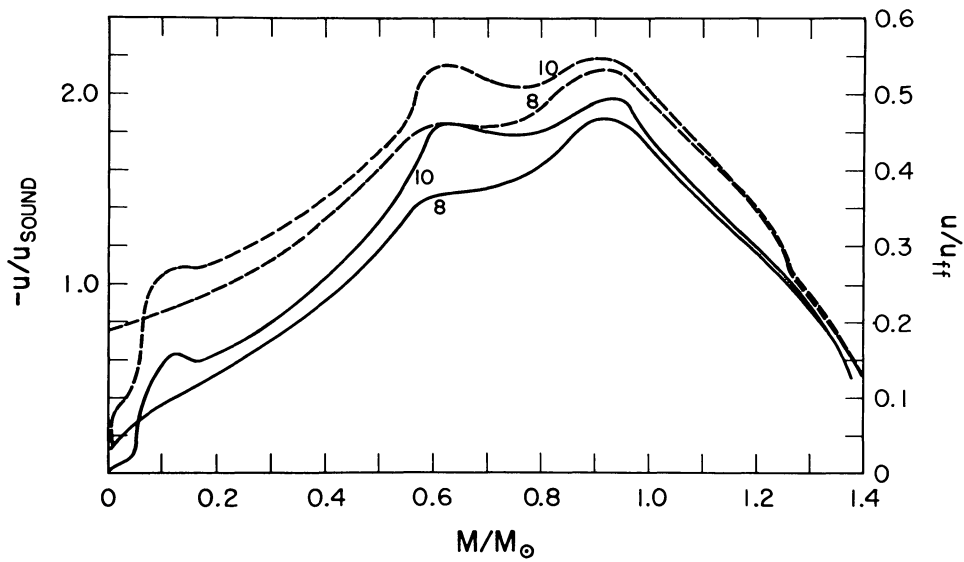


FIG. 32.—The ratio of the negative of the matter velocity u to the speed of sound u_{sound} (solid lines) and the ratio of u to the free-fall velocity u_{ff} (dashed lines) as a function of the enclosed rest mass for stages 8 and 10 of the infall of the standard model.

a) Core Deleptonization during Infall

It was argued that the core deleptonization during infall was one of the most important aspects of the calculation—a greater degree of core deleptonization making it less likely that the shock will propagate outward and expel matter in a prompt manner. One of the principal conclusions of this work concerns the substantial degree of core deleptonization of our standard model. The immediate precollapse lepton fraction of the core varied from 0.4254 at the center to 0.464 at the edge. At core turnaround, the lepton fraction of the core of the standard model varied from 0.30 at the center to 0.344 at the edge of the inner core. This degree of core deleptonization is larger than that given by most other recent calculations, as is evident by the comparisons in Table 5.

The culprit mainly responsible for the extent of core deleptonization is neutrino-electron scattering (NES) and the equation of state. (The effect of the latter will be discussed in § IVe below.) A model (NES) computed without electron capture on nuclei suffered roughly the same deleptonization, although the time history of the deleptonization was substantially different. On the other hand, two models computed without NES, one with electron capture on nuclei omitted and one with this process included, had electron fractions at core bounce substantially higher than the standard model. Without NES, the emitted neutrinos tended to fill the higher energy states first, resulting in a neutrino distribution skewed to high energies. Neutrinos did not equilibrate with matter until densities substantially higher than the trapping density were reached. With NES included, the neutrinos became equilibrated with the matter at a density almost an order of magnitude lower. By downscattering in energy some of the excess high-energy neutrinos produced by electron captures, NES lowered the mean neutrino energy in the important transport regime ($\rho \gtrsim$ trapping density). Since the neutrino interaction cross sections typically increase as the square of the neutrino energy, the effect of NES was to increase substantially the rate of neutrino transport, with the consequence of considerably greater core deleptonization. For the standard model, the emergent neutrino spectrum at bounce peaked at 7.5 MeV.

b) Neutrino Trapping Density

The value of the ν_e trapping density, ρ_{trap} , during the infall of the standard model decreased from $10^{12} \text{ g cm}^{-3}$ when neutrinos first become trapped to $4.5 \times 10^{11} \text{ g cm}^{-3}$ at core bounce. The decrease in ρ_{trap} was due almost entirely to the increase with time in the compression rate of matter at the trapping density. Considerable outward transport of neutrinos through mass occurred above the trapping density, even though the average neutrino was moving inward in an Eulerian sense. Thus, a substantial amount of deleptonization occurred above the trapping density, particularly for the inner mass zones.

c) Entropy Change during Infall

The entropy of matter below the trapping density increased if electron captures on nuclei dominated, or if electron captures on free protons dominated and $Y_e > 0.44$; otherwise the entropy of the matter decreased. Above the trapping density the matter entropy increased substantially until the neutrinos were completely equilibrated with the matter. With s denoting the entropy per baryon divided by the Boltzmann constant, the initial value of s increased from about 1.1 at the center of the core to about 1.7 at the core edge. Just prior to core bounce, the value of s had increased by about 0.35 over its initial value throughout the inner core.

d) Hydrodynamics during Infall

The hydrodynamics of the core infall appeared to be in qualitative accord with the self-similar solutions, despite the fact that the effective adiabatic index was constant neither in space nor in time. The mass shell having the greatest inward velocity divided the collapsing core into an inner and an outer core, each of which underwent different hydrodynamics. The mass of the inner core decreased with time from 0.87 to 0.59 M_\odot , most of the decrease occurring as the central density increased from 10^{13} to $7 \times 10^{13} \text{ g cm}^{-3}$. The effective adiabatic index dipped to about 1.24 at $\rho \approx 10^{11} \text{ g cm}^{-3}$ as a result of electron captures on nuclei, and dipped to about 1.27 at

TABLE 5
CENTRAL VALUES OF Y_l AT BOUNCE

Collapse Calculation	Y_l
Standard model (this work).....	0.30 0.31 (averaged over inner 0.56 M_\odot of core) (0.36 at $\rho_c = 3 \times 10^{11} \text{ g cm}^{-3}$; 0.33 at $\rho_c = 10^{12} \text{ g cm}^{-3}$) 0.38 ($\rho_{\text{trap}} = 3 \times 10^{11} \text{ g cm}^{-3}$) ^a 0.36 ($\rho_{\text{trap}} = 10^{12} \text{ g cm}^{-3}$) ^a
Hillebrandt and Müller 1981	0.37
Bludman, Lichtenstadt, and Hayden 1982.....	0.23
Arnett 1977b.....	0.35
Arnett 1982a.....	0.38 (minimum value of 0.31 at roughly half the inner-core mass)
Mazurek, Cooperstein, and Kahana 1980	0.385
Bowers and Wilson 1982b	0.35
Van Riper and Lattimer 1981	0.40
Hillebrandt 1983.....	

NOTE.— ρ_c = central density.

^aNeutrino transport was cut off above ρ_{trap} .

$\rho \approx 2.5 \times 10^{12} \text{ g cm}^{-3}$ owing to electron captures on free protons. One final large dip occurred at $\rho \approx 10^{14} \text{ g cm}^{-3}$ because of the softening of the equation of state just below nucleon density. The mass-averaged effective adiabatic index $\langle \Gamma_E \rangle$ of the inner core fluctuated between 1.25 and 1.30 during most of the infall. Because of this rather low value of $\langle \Gamma_E \rangle$, the mass of the inner core had dropped to about $0.59 M_\odot$ by core turnaround.

e) Comparison with Other Work

The extent of the core deleptonization obtained during the infall of the standard model is substantially greater than that obtained in most other recent calculations, as noted in § IVa, so considerable concern arises as to the correctness of this model. Comparisons with other work that uses simpler numerical algorithms for the neutrino interactions and transport are difficult to make, short of using these algorithms in the standard model for a direct comparison. Nevertheless, attempts were made to account for some of the differences between the standard model and other work in § III.

The recent calculations of Bowers and Wilson (1982b) were performed with detail comparable to that in the present work, but resulted in a considerably greater trapped lepton fraction. A direct comparison of these two calculations is therefore of great interest. To this end, the calculation of the core infall of the standard model was repeated with the Bowers and Wilson equation of state (Wilson 1980; Bowers and Wilson 1982a, b) substituted for the "Illinois" equation of state. The result was a trapped lepton fraction almost identical with the value quoted by Bowers and Wilson (1982b) for their $10 M_\odot$ model ($Y_t \sim 0.375$ averaged over the inner $0.56 M_\odot$). The larger trapped lepton fraction resulted mainly from (1) a larger mean heavy-nucleus mass number, which caused the allowed electron capture on heavy nuclei to be cut off earlier in the collapse, and (2) a substantially smaller mass fraction of free protons, which reduced the rate of electron capture thereafter.

Because of the differences obtained in the trapped electron fraction resulting from the use of a different equation of state, a further calculation was performed using the "Munich" equation of state (Wolff 1983). The trapped lepton fraction resulting from this last calculation was only slightly greater ($\Delta Y_t \sim 0.005-0.01$) than that of the standard model.

Judging from the results of these calculations, it appears that if the differences in the core configuration of the initial models can be ignored, the differences between the standard model and the results obtained by Bowers and Wilson (1982a, b) can be largely accounted for by the differences in the equation of state used. A more detailed comparison of these results will be the subject of a forthcoming paper.

f) Implications

The considerable extent of the core deleptonization during the infall of the standard model resulted in an inner-core mass of only $0.59 M_\odot$ at core turnaround. The resulting large mass of the outer core through which the shock, formed at the outer edge of the inner core at core turnaround, must propagate,

and the correspondingly large value of the ram pressure of the infalling outer core opposing the outward propagation of the shock, make it unlikely that the shock will propagate outward and expel matter in a prompt fashion. The calculation of the propagation of the shock through the core of the standard model has been completed, and the results show that the shock does indeed stall. This calculation will be the subject of a forthcoming paper.

Two important questions immediately present themselves in the face of these results. Is the extent of the core deleptonization during the infall of the standard model (i.e., the $10 M_\odot$ model of Weaver and Woosley 1980a) typical, or is it merely a reflection of the particular initial structure of this model? Does the faltering of the outward Eulerian propagation of the shock before it reaches the outer edge of the core spell doom for the possibility of a supernova, or might the shock at some later time be rejuvenated?

Of relevance to the first question is the recent work of Weaver, Woosley, and Fuller (1982), who find smaller "Fe" cores with lower entropies for their precollapse models of massive stars. Lower entropy cores tend to undergo a smaller degree of deleptonization during infall because the free proton abundance, and therefore the electron capture rate, is smaller. A smaller "Fe" core will result in a smaller outer core through which the shock must propagate. Preliminary results of models obtained from the Weaver-Woosley (1980a) $10 M_\odot$ model by first artificially lowering the entropy and then evolving the resulting core through the infall stage of core collapse were not encouraging. Although the extent of the core deleptonization was reduced, considerable core deleptonization occurred even for cases in which the entropy of the Weaver-Woosley model was substantially reduced, and even for calculations in which the electron capture rate on nuclei was set to zero. This will be the subject of a forthcoming paper.

The outlook appears more optimistic concerning the second question. A recent calculation by Wilson (1983) showed that the slow neutrino heating of the matter that was behind the shock but well outside the neutrino sphere strengthened the shock and led to an explosion. The heating time scale was found to be about 250 ms for a $10 M_\odot$ model, increasing to about 550 ms for a $25 M_\odot$ model. The extended postcollapse behavior of massive stars certainly seems worth pursuing.

My thanks for the unstinting support of the staff of the Southeast Regional Data Center and the more recently formed Florida Atlantic University Academic Computing Center, where the numerical work was performed, and in particular to Bob Gray for many hours spent in troubleshooting problems arising with the use of the various computers. The use of the Algebraic Manipulator "REDUCE 2" greatly eased the burden of extracting useful results for the moments of the neutrino-electron scattering kernels and the neutrino absorption and production kernels due to electron-positron pair annihilation. This research was supported in part by NSF grant AST-8111709.

APPENDIX A

MULTIGROUP FLUX-LIMITED DIFFUSION APPROXIMATION

In this appendix I derive the multigroup flux-limited diffusion approximation (MGFLDA) used in this investigation to evolve the neutrino distribution for each neutrino type, and to follow the momentum-energy and lepton number exchanges with the matter. Matter in this context refers to all constituents of the stellar core other than neutrinos. Some of the material in the first part of this appendix has appeared elsewhere (Bruenn, Buchler, and Yueh 1978a) but is presented again here for the sake of completeness and continuity of exposition.

The derivation of the MGFLDA begins with the assumption that the evolution of the neutrino distribution can be adequately described by an appropriate Boltzmann transport equation (BTE) with source terms involving the constituents of the matter but constructed with the assumption that these constituents are not spatially correlated. The BTE appropriate for neutrinos, and with the assumption of spherical symmetry, is given by

$$B_t[f] + B_s[f] + B_v[f] = B_{AE}[f] + B_{NES}[f] + B_{IS}[f] + B_{TP}[f, \bar{f}], \quad (A1)$$

where $f = f(t, r, \mu, \omega)$ is the neutrino occupation probability defined such that $dn = f(t, r, \mu, \omega) dV d\Omega [\omega^2 d\omega / (2\pi\hbar c)^3]$ is the mean number of neutrinos at time t_1 within a volume dV at r , having a propagation direction within a solid angle $d\Omega$ at μ , and within an energy $d\omega$ at ω . Here r is a Lagrangian coordinate (distance from the center of the star of a given spherically symmetric fluid element), μ is the cosine of the angle between the propagation direction of the neutrino and the outward radial direction, and ω is the neutrino energy.

The terms on the left-hand side of equation (A1) have been derived to first order in v/c by Castor (1972), and are given by

$$B_t[f] = \frac{1}{c} \frac{\partial f}{\partial t}, \quad (A2)$$

$$B_s[f] = \frac{\mu}{r^2} \frac{\partial}{\partial r} (r^2 f) + \frac{1}{r} \frac{\partial}{\partial \mu} [(1 - \mu^2) f], \quad (A3)$$

$$\begin{aligned} B_v[f] = & -\frac{f}{c} \frac{\partial \ln \rho}{\partial t} - \frac{1}{c} \left[\left(\frac{\partial \ln \rho}{\partial t} + \frac{3v}{r} \right) \mu^2 - \frac{v}{r} \right] + \frac{1}{c} \left[\left(\frac{\partial \ln \rho}{\partial t} + \frac{3v}{r} \right) \mu^2 - \frac{v}{r} \right] \frac{1}{\omega^3} \frac{\partial}{\partial \omega} (\omega^4 f) \\ & + \frac{\partial}{\partial \mu} \left\{ \left[\frac{1}{c} \left(\frac{\partial \ln \rho}{\partial t} + \frac{3v}{r} \right) \mu (1 - \mu^2) \right] f \right\}. \end{aligned} \quad (A4)$$

Here v is the matter velocity given by $v = (\partial r / \partial t)_m$, where m is the mass enclosed by r . Terms of order $(v/c)^2$ and $(\partial v / \partial t)_m$ have been dropped. [Buchler 1979 has derived an expression analogous to expression (A4) in which the terms in $(\partial v / \partial t)_m$ have been retained.]

The terms on the right-hand side of equation (A1) are the neutrino source terms. The dependence of these terms on r and t will be suppressed for notational convenience [e.g., $f(\mu, \omega) \equiv f(t, r, \mu, \omega)$]. These terms are given by

$$B_{AE}[f] = j(\omega) [1 - f(\mu, \omega)] - f(\mu, \omega) / \lambda^a(\omega), \quad (A5)$$

corresponding to absorption and emission, where $j(\omega)$ is the neutrino emissivity and $\lambda^a(\omega)$ the neutrino absorption mean free path;

$$\begin{aligned} B_{NES}[f] = & [1 - f(\mu, \omega)] \frac{1}{c(2\pi\hbar c)^3} \int_0^\infty \omega'^2 d\omega' \int_{-1}^1 d\mu' f(\mu', \omega') \int_0^{2\pi} d\phi R_{NES}^{\text{in}}(\omega, \omega', \cos \theta) \\ & - f(\mu, \omega) \frac{1}{c(2\pi\hbar c)^3} \int_0^\infty \omega'^2 d\omega' \int_{-1}^1 d\mu' [1 - f(\mu', \omega')] \int_0^{2\pi} R_{NES}^{\text{out}}(\omega, \omega', \cos \theta), \end{aligned} \quad (A6)$$

corresponding to neutrino-electron scattering, where $R_{NES}^{\text{in/out}}(\omega, \omega', \cos \theta)$ is the in/out beam neutrino-electron scattering kernel, and θ , the angle between the incident and emergent neutrino, is given by

$$\cos \theta = \mu \mu' + [(1 - \mu^2)(1 - \mu'^2)]^{1/2} \cos \phi, \quad (A7)$$

where ϕ is the azimuthal angle of one neutrino relative to the other;

$$B_{IS}[f] = \frac{1}{c(2\pi\hbar c)^3} \omega^2 \int_{-1}^1 d\mu' \int_0^{2\pi} d\phi R_{IS}^0(\omega, \omega, \cos \theta) [f(\mu', \omega) - f(\mu, \omega)], \quad (A8)$$

corresponding to isoenergetic neutrino scattering (neutrino scattering on protons, neutrons, or nuclei, for which the energy exchange is assumed to be zero), where $R_{\text{IS}}^0(\omega, \omega', \cos \theta) \delta(\omega - \omega') = R_{\text{IS}}(\omega, \omega', \cos \theta)$. Expression (A8) results when $R_{\text{IS}}(\omega, \omega', \cos \theta)$, the isoenergetic neutrino scattering kernel, is substituted for $R_{\text{NES}}^{\text{in/out}}(\omega, \omega', \cos \theta)$ in an expression similar to expression (A6);

$$\begin{aligned} B_{\text{TP}} = & [1 - f(\mu, \omega)] \frac{1}{c(2\pi\hbar c)^3} \int_0^\infty \omega'^2 d\omega' \int_{-1}^1 d\mu' \int_0^{2\pi} d\phi R_{\text{TP}}^p(\omega, \omega', \cos \theta) [1 - \bar{f}(\mu', \omega')] \\ & - f(\mu, \omega) \frac{1}{c(2\pi\hbar c)^3} \int_0^\infty \omega'^2 d\omega' \int_{-1}^1 d\mu' \int_0^{2\pi} d\phi R_{\text{TP}}^a(\omega, \omega', \cos \theta) \bar{f}(\mu', \omega'), \end{aligned} \quad (\text{A9})$$

corresponding to thermal production and absorption of neutrino-antineutrino pairs, where \bar{f} is the occupation probability of the antiparticle of the particle described by f , and R_{TP}^p and R_{TP}^a are the thermal production and absorption kernels.

The MGFLDA used here is obtained by expanding the neutrino occupation probability, f , in a Legendre series and keeping only the first two terms, that is,

$$f(t, r, \mu, \omega) = \psi^{(0)}(t, r, \omega) + \mu \psi^{(1)}(t, r, \omega), \quad (\text{A10})$$

and assuming that $\psi^{(1)}$ does not depend explicitly on time, i.e.,

$$\frac{\partial}{\partial t} \psi^{(1)} = 0. \quad (\text{A11})$$

The truncation of all but the first two terms in the Legendre expansion for f is justified, as it stands, only for small deviations of f from isotropy. The addition of a flux limiter (see below) extends the range of applicability of equation (A10) to regions where the neutrino mean free paths are large and f is very anisotropic.

Substituting equation (A10) in equation (A1) and applying the operator $\frac{1}{2} \int_{-1}^1 d\mu$, we have

$$\begin{aligned} & \frac{1}{c} \frac{\partial}{\partial t} \psi^{(0)} + \frac{1}{3r^2} \frac{\partial}{\partial r} (r^2 \psi^{(1)}) + \frac{1}{3c} \frac{\partial \ln \rho}{\partial t} \left(\omega \frac{\partial}{\partial \omega} \psi^{(0)} \right) \\ & = j(\omega) (1 - \psi^{(0)}) - \Psi^{(0)} / \lambda^{(a)}(\omega) + A^{(0)}(\omega) \psi^{(0)} + B^{(0)}(\omega) \psi^{(1)} + C^{(0)}(\omega). \end{aligned} \quad (\text{A12})$$

We have suppressed in our notation the dependence of the variables in equation (A12) on r and t and will continue this practice below. Substituting equation (A10) in equation (A1), applying the operator $\frac{3}{2} \int_{-1}^1 \mu d\mu$, and using equation (A11), yields

$$\begin{aligned} & \frac{\partial}{\partial r} \psi^{(0)} + \left[-\frac{2}{c} \frac{\partial \ln \rho}{\partial t} \psi^{(1)} - \frac{2v}{cr} \psi^{(1)} + \frac{3}{5c} \frac{\partial \ln \rho}{\partial t} \frac{1}{\omega^3} \frac{\partial}{\partial \omega} (\omega^4 \psi^{(1)}) + \frac{4}{5} \frac{v}{cr} \frac{1}{\omega^3} \frac{\partial}{\partial \omega} (\omega^4 \psi^{(1)}) \right] \\ & = -[j(\omega) + 1/\lambda^{(a)}(\omega)] \psi^{(1)} + A^{(1)}(\omega) \psi^{(0)} + B^{(1)}(\omega) \psi^{(1)} + C^{(1)}(\omega). \end{aligned} \quad (\text{A13})$$

The terms on the right-hand side in equations (A12) and (A13) are given by

$$A^{(a)}(\omega) = A_{\text{NES}}^{(a)}(\omega) + A_{\text{IS}}^{(a)}(\omega) + A_{\text{TP}}^{(a)}(\omega), \quad (\text{A14})$$

with similar expressions for $B^{(a)}(\omega)$ and $C^{(a)}(\omega)$. These quantities are given by

$$\begin{aligned} A_{\text{NES}}^{(a)}(\omega) = & \frac{1}{c(2\pi\hbar c)^3} \int_0^\infty \omega'^2 d\omega' \{ [\mathcal{F}_{\alpha,0}^{\text{out}}(\omega, \omega') - \mathcal{F}_{\alpha,0}^{\text{in}}(\omega, \omega')] \psi^{(0)}(\omega') \\ & + [\mathcal{F}_{\alpha,1}^{\text{out}}(\omega, \omega') - \mathcal{F}_{\alpha,1}^{\text{in}}(\omega, \omega')] \psi^{(1)}(\omega') - \mathcal{F}_{\alpha,0}^{\text{out}} \}, \end{aligned} \quad (\text{A15})$$

$$\begin{aligned} B_{\text{NES}}^{(a)}(\omega) = & \frac{1}{c(2\pi\hbar c)^3} \int_0^\infty \omega'^2 d\omega' \{ [\mathcal{F}_{\alpha+1,0}^{\text{out}}(\omega, \omega') - \mathcal{F}_{\alpha+1,0}^{\text{in}}(\omega, \omega')] \psi^{(0)}(\omega') \\ & + [\mathcal{F}_{\alpha+1,1}^{\text{out}}(\omega, \omega') - \mathcal{F}_{\alpha+1,1}^{\text{in}}(\omega, \omega')] \psi^{(1)}(\omega') - \mathcal{F}_{\alpha+1,0}^{\text{out}} \}, \end{aligned} \quad (\text{A16})$$

$$C_{\text{NES}}^{(a)}(\omega) = \frac{1}{c(2\pi\hbar c)^3} \int_0^\infty \omega'^2 d\omega' [\mathcal{F}_{\alpha,0}^{\text{in}}(\omega, \omega') \psi^{(0)}(\omega') + \mathcal{F}_{\alpha,1}^{\text{in}}(\omega, \omega') \psi^{(1)}(\omega')], \quad (\text{A17})$$

where

$$\mathcal{F}_{\beta,\gamma}^{\text{in/out}}(\omega, \omega') = \frac{1+2\alpha}{2} \int_{-1}^1 d\mu \mu^\beta \int_{-1}^1 d\mu' \mu'^\gamma \int_0^{2\pi} d\phi R_{\text{NES}}^{\text{in/out}}(\omega, \omega', \cos \theta). \quad (\text{A18})$$

The quantities $A_{\text{IS}}^{(\alpha)}(\omega)$, $B_{\text{IS}}^{(\alpha)}(\omega)$, and $C_{\text{IS}}^{(\alpha)}(\omega)$ are zero, except for $B_{\text{IS}}^{(1)}$, which is given by

$$B_{\text{IS}}^{(1)}(\omega) = \frac{1}{c(2\pi\hbar c)^3} \omega^2 [\mathcal{G}_{1,1}(\omega) - \mathcal{G}_{2,0}(\omega)], \quad (\text{A19})$$

where

$$\mathcal{G}_{\beta,\gamma}(\omega) = \frac{1+2\alpha}{2} \int_{-1}^1 d\mu \mu^\beta \int_{-1}^1 d\mu' \mu'^\gamma \int_0^{2\pi} d\phi R_{\text{IS}}^0(\omega, \omega', \cos \theta). \quad (\text{A20})$$

The quantities $A_{\text{TP}}^{(\alpha)}(\omega)$, $B_{\text{TP}}^{(\alpha)}(\omega)$, and $C_{\text{TP}}^{(\alpha)}(\omega)$ are given by

$$\begin{aligned} A_{\text{TP}}^{(\alpha)}(\omega) &= \frac{1}{c(2\pi\hbar c)^3} \int_0^\infty \omega'^2 d\omega' \{ [\mathcal{H}_{\alpha,0}^p(\omega, \omega') - \mathcal{H}_{\alpha,0}^a(\omega, \omega')] \bar{\psi}^{(0)}(\omega') \\ &\quad + [\mathcal{H}_{\alpha,1}^p(\omega, \omega') - \mathcal{H}_{\alpha,1}^a(\omega, \omega')] \bar{\psi}^{(1)}(\omega') - \mathcal{H}_{\alpha,0}^p(\omega, \omega') \}, \end{aligned} \quad (\text{A21})$$

$$\begin{aligned} B_{\text{TP}}^{(\alpha)}(\omega) &= \frac{1}{c(2\pi\hbar c)^3} \int_0^\infty \omega'^2 d\omega' \{ [\mathcal{H}_{\alpha+1,0}^p(\omega, \omega') - \mathcal{H}_{\alpha+1,0}^a(\omega, \omega')] \bar{\psi}^{(0)}(\omega') \\ &\quad + [\mathcal{H}_{\alpha+1,1}^p(\omega, \omega') - \mathcal{H}_{\alpha+1,1}^a(\omega, \omega')] \bar{\psi}^{(1)}(\omega') - \mathcal{H}_{\alpha+1,0}^p(\omega, \omega') \}, \end{aligned} \quad (\text{A22})$$

$$C_{\text{TP}}^{(\alpha)}(\omega) = \frac{1}{c(2\pi\hbar c)^3} \int_0^\infty \omega'^2 d\omega' [-\mathcal{H}_{\alpha,0}^p(\omega, \omega') \bar{\psi}^{(0)}(\omega') - \mathcal{H}_{\alpha,1}^p(\omega, \omega') \bar{\psi}^{(1)}(\omega') + \mathcal{H}_{\alpha,0}^p(\omega, \omega')], \quad (\text{A23})$$

where $\bar{\psi}^{(0)}$ and $\bar{\psi}^{(1)}$ correspond to the antiparticles of the particles described by $\psi^{(0)}$ and $\psi^{(1)}$, and where

$$\mathcal{H}_{\beta,\gamma}^{p/a}(\omega, \omega') = \frac{1+2\alpha}{2} \int_{-1}^1 d\mu \mu^\beta \int_{-1}^1 d\mu' \mu'^\gamma \int_0^{2\pi} d\phi R_{\text{TP}}^{p/a}(\omega, \omega', \cos \theta). \quad (\text{A24})$$

To derive a diffusion equation from equations (A12) and (A13), we neglect the velocity-dependent terms (the terms in brackets) on the left-hand side of equation (A13), since they contribute only to $O(v^2/c^2)$ in the energy-balance equation, and solve equation (A13) formally for $\psi^{(1)}$ to obtain

$$\psi^{(1)} = -\lambda^{(t)}(\omega) \left[\frac{\partial}{\partial r} \psi^{(0)} - A^{(1)}(\omega) \psi^{(0)} - C^{(1)}(\omega) \right], \quad (\text{A25})$$

where

$$1/\lambda^{(t)}(\omega) = j(\omega) + 1/\lambda^{(a)}(\omega) - B^{(1)}(\omega). \quad (\text{A26})$$

Substitution of equation (A25) in equation (A12) results in a diffusion equation for neutrinos of energy ω of the form

$$\begin{aligned} \frac{1}{c} \frac{\partial}{\partial t} \psi^{(0)} - \frac{1}{3r^2} \frac{d}{dr} \left\{ r^2 \lambda^{(t)}(\omega) \left[\frac{\partial}{\partial r} \psi^{(0)}(\omega) - A^{(1)}(\omega) \psi^{(0)} - C^{(1)}(\omega) \right] \right\} + \frac{1}{3c} \frac{\partial \ln \rho}{\partial t} \left(\omega \frac{\partial}{\partial \omega} \psi^{(0)} \right) \\ = X(\omega) + Y(\omega) \psi^{(0)} + Z(\omega) \frac{\partial}{\partial r} \psi^{(0)}, \end{aligned} \quad (\text{A27})$$

where

$$X(\omega) = j(\omega) + C^{(0)}(\omega) + B^{(0)}(\omega) C^{(1)}(\omega) \lambda^{(t)}(\omega), \quad (\text{A28})$$

$$Y(\omega) = -j(\omega) - 1/\lambda^{(a)}(\omega) + A^{(0)}(\omega) + B^{(0)}(\omega) A^{(1)}(\omega) \lambda^{(t)}(\omega), \quad (\text{A29})$$

$$Z(\omega) = -B^{(0)}(\omega) \lambda^{(t)}(\omega). \quad (\text{A30})$$

There are several problems with equation (A27) as it stands. The first is that the quantities $\lambda^{(t)}(\omega)$, $A^{(1)}(\omega)$, $C^{(1)}(\omega)$, and the terms on the right-hand side are functionals of both $\psi^{(0)}$ and $\psi^{(1)}$ because of the neutrino-electron scattering terms (eqs. [A15]–[A17]), and of both $\bar{\psi}^{(0)}$ and $\bar{\psi}^{(1)}$ because of the neutrino thermal production and absorption terms (eqs. [A21]–[A23]). We will return to this problem in Appendix B, where the numerical solution of equations (A25) and (A27) is discussed.

This second problem with equation (A27) is that it is valid only for neutrino-opaque regions where the anisotropy of the neutrino occupation probability is very small. This is because of the truncation of the neutrino occupation probability, $f(\omega, \mu)$, after the first two terms. In the free-streaming neutrino transparent regime, all terms in the Legendre expansion of $f(\omega, \mu)$ become important. So that equation (A27) will give accurate solutions of f in both neutrino-opaque and -transparent regimes, the well-known artifice of including a flux limiter in $\lambda^{(t)}(\omega)$ is employed. That is, $\lambda^{(t)}(\omega)$ is modified so that

$$\lambda^{(t)}(\omega) \rightarrow \Lambda^{(t)}(\omega), \quad (\text{A31})$$

where, in its simplest form,

$$\Lambda^{(t)}(\omega) = \frac{3\lambda^{(t)}(\omega)}{3 + \lambda^{(t)}(\omega)|\nabla\psi^{(0)}(\omega)|/\psi^{(0)}(\omega)}, \quad (\text{A32})$$

which, by limiting the magnitude of the neutrino flux when $\lambda^{(t)}(\omega)$ becomes large, prevents the effective velocity of neutrinos from exceeding the velocity of light. The exact prescription for constructing the flux limiter used here is described in detail in Bruenn, Buchler, and Yueh (1978a). The use of a flux limiter requires a careful treatment of the neutrino-matter coupling, since inconsistencies can easily arise. This is discussed below.

The neutrino-electron scattering and thermal production terms on the right-hand side of equation (A27) require quadruple integrations (over μ , μ' , ϕ , and ω') for their evaluation, while the neutrino isoenergetic scattering terms require triple integrations (over μ , μ' , and ϕ). The integrations over μ , μ' , and ϕ can be eliminated by expanding the kernels of these terms in a Legendre series and truncating these expansions after the first two terms, as is appropriate with the diffusion approximation.

Expanding the neutrino-electron scattering kernels in the first two terms of a Legendre series yields

$$R_{\text{NES}}^{\text{in/out}}(\omega, \omega', \cos \theta) = \frac{1}{2} \sum_l (2l+1) \Phi_{l,\text{NES}}^{\text{in/out}}(\omega, \omega') P_l(\cos \theta) \approx \frac{1}{2} \Phi_{0,\text{NES}}^{\text{in/out}}(\omega, \omega') + \frac{3}{2} \Phi_{1,\text{NES}}^{\text{in/out}}(\omega, \omega') \cos \theta. \quad (\text{A33})$$

With the use of equation (A33) the quantities $A_{\text{NES}}^{(\alpha)}(\omega)$, $B_{\text{NES}}^{(\alpha)}(\omega)$, and $C_{\text{NES}}^{(\alpha)}(\omega)$, given by equations (A15)–(A17), can now be written as

$$A_{\text{NES}}^{(0)}(\omega) = -\frac{2\pi}{c(2\pi\hbar c)^3} \int_0^\infty \omega'^2 d\omega' \{ \Phi_{0,\text{NES}}^{\text{in}}(\omega, \omega') \psi^{(0)}(\omega') + \Phi_{0,\text{NES}}^{\text{out}}(\omega, \omega') [1 - \psi^{(0)}(\omega')] \}, \quad (\text{A34})$$

$$B_{\text{NES}}^{(0)}(\omega) = -\frac{2\pi}{3c(2\pi\hbar c)^3} \int_0^\infty \omega'^2 d\omega' [\Phi_{1,\text{NES}}^{\text{in}}(\omega, \omega') - \Phi_{1,\text{NES}}^{\text{out}}(\omega, \omega')] \psi^{(1)}(\omega'), \quad (\text{A35})$$

$$C_{\text{NES}}^{(0)}(\omega) = \frac{2\pi}{c(2\pi\hbar c)^3} \int_0^\infty \omega'^2 d\omega' \Phi_{0,\text{NES}}^{\text{in}}(\omega, \omega') \psi^{(0)}(\omega'), \quad (\text{A36})$$

$$A_{\text{NES}}^{(1)}(\omega) = -\frac{2\pi}{c(2\pi\hbar c)^3} \int_0^\infty \omega'^2 d\omega' [\Phi_{1,\text{NES}}^{\text{in}}(\omega, \omega') - \Phi_{1,\text{NES}}^{\text{out}}(\omega, \omega')] \psi^{(1)}(\omega'), \quad (\text{A37})$$

$$B_{\text{NES}}^{(1)}(\omega) = -\frac{2\pi}{c(2\pi\hbar c)^3} \int_0^\infty \omega'^2 d\omega' \{ \Phi_{0,\text{NES}}^{\text{in}}(\omega, \omega') \psi^{(0)}(\omega') + \Phi_{0,\text{NES}}^{\text{out}}(\omega, \omega') [1 - \psi^{(0)}(\omega')] \}, \quad (\text{A38})$$

$$C_{\text{NES}}^{(1)}(\omega) = \frac{2\pi}{c(2\pi\hbar c)^3} \int_0^\infty \omega'^2 d\omega' \Phi_{1,\text{NES}}^{\text{in}}(\omega, \omega') \psi^{(1)}(\omega'). \quad (\text{A39})$$

Expanding the isoenergetic scattering kernel in a similar manner gives

$$R_{\text{IS}}^0(\omega, \omega, \cos \theta) \approx \frac{1}{2} \Phi_{0,\text{IS}}(\omega) + \frac{3}{2} \Phi_{1,\text{IS}}(\omega) \cos \theta. \quad (\text{A40})$$

The quantities $A_{\text{IS}}^{(\alpha)}(\omega)$, $B_{\text{IS}}^{(\alpha)}(\omega)$, and $C_{\text{IS}}^{(\alpha)}(\omega)$ are again zero, except for $B_{\text{IS}}^{(1)}(\omega)$ (eq. [A19]), which is now given by

$$B_{\text{IS}}^{(1)}(\omega) = \frac{2\pi}{c(2\pi\hbar c)^3} \omega^2 [\Phi_{1,\text{IS}}(\omega) - \Phi_{0,\text{IS}}(\omega)]. \quad (\text{A41})$$

Finally, the thermal production and absorption kernels are expanded to give

$$R_{\text{TP}}^{p/a}(\omega, \omega', \cos \theta) \approx \frac{1}{2} \Phi_{0,\text{TP}}^{p/a}(\omega, \omega') + \frac{3}{2} \Phi_{1,\text{TP}}^{p/a}(\omega, \omega') \cos \theta, \quad (\text{A42})$$

from which the quantities $A_{\text{TP}}^{(a)}(\omega)$, $B_{\text{TP}}^{(a)}(\omega)$, and $C_{\text{TP}}^{(a)}(\omega)$, given by equations (A21)–(A23), can now be written

$$A_{\text{TP}}^{(0)}(\omega) = -\frac{2\pi}{c(2\pi\hbar c)^3} \int_0^\infty \omega'^2 d\omega' \left\{ \Phi_{0,\text{TP}}^p(\omega, \omega') [1 - \bar{\psi}^{(0)}(\omega')] + \Phi_{0,\text{TP}}^a \bar{\psi}^{(0)}(\omega') \right\}, \quad (\text{A43})$$

$$B_{\text{TP}}^{(0)}(\omega) = \frac{2\pi}{3c(2\pi\hbar c)^3} \int_0^\infty \omega'^2 d\omega' [\Phi_{1,\text{TP}}^p(\omega, \omega') - \Phi_{1,\text{TP}}^a(\omega, \omega')] \bar{\psi}^{(1)}(\omega'), \quad (\text{A44})$$

$$C_{\text{TP}}^{(0)}(\omega) = \frac{2\pi}{c(2\pi\hbar c)^3} \int_0^\infty \omega'^2 d\omega' \Phi_{0,\text{TP}}^p(\omega, \omega') [1 - \bar{\psi}^{(0)}(\omega')], \quad (\text{A45})$$

$$A_{\text{TP}}^{(1)}(\omega) = \frac{2\pi}{c(2\pi\hbar c)^3} \int_0^\infty \omega'^2 d\omega' [\Phi_{1,\text{TP}}^p(\omega, \omega') - \Phi_{1,\text{TP}}^a(\omega, \omega')] \bar{\psi}^{(1)}(\omega'), \quad (\text{A46})$$

$$B_{\text{TP}}^{(1)}(\omega) = -\frac{2\pi}{c(2\pi\hbar c)^3} \int_0^\infty \omega'^2 d\omega' \left\{ \Phi_{0,\text{TP}}^p(\omega, \omega') [1 - \bar{\psi}^{(0)}(\omega')] + \Phi_{0,\text{TP}}^a(\omega, \omega') \bar{\psi}^{(0)}(\omega') \right\}, \quad (\text{A47})$$

$$C_{\text{TP}}^{(1)}(\omega) = -\frac{2\pi}{c(2\pi\hbar c)^3} \int_0^\infty \omega'^2 d\omega' \Phi_{1,\text{TP}}^p \bar{\psi}^{(1)}(\omega'). \quad (\text{A48})$$

The numerical computation of $j(\omega)$, $\lambda^{(a)}(\omega)$, and the Legendre terms $\Phi_{l,\text{NES}}^{\text{in}/\text{out}}(\omega, \omega')$, $\Phi_{l,\text{IS}}(\omega)$, and $\Phi_{l,\text{TP}}^{p/a}(\omega, \omega')$ is described in Appendix C.

In order to treat the energy-momentum transfer between neutrinos and matter consistently, it is helpful to consider the energy-momentum conservation equations that arise from the MGFLDA. The Newtonian approximation to the matter hydrodynamics will be made here. Operating on equation (A12) by

$$\frac{4\pi c}{(2\pi\hbar c)^3} \int_0^\infty \omega^3 d\omega$$

yields

$$\begin{aligned} \frac{\partial}{\partial t} \left(\frac{E_\nu}{\rho} \right) + \frac{1}{\rho} \frac{1}{r^2} \frac{\partial}{\partial r} (r^2 F_\nu) + P_\nu \frac{\partial}{\partial t} \left(\frac{1}{\rho} \right) &= \frac{1}{\rho} \frac{4\pi c}{(2\pi\hbar c)^3} \int_0^\infty \omega^3 d\omega \left\{ j(\omega) - [j(\omega) - 1/\lambda^{(a)}(\omega) - A^{(0)}(\omega)] \psi^{(0)}(\omega) \right. \\ &\quad \left. + B^{(0)}(\omega) \psi^{(1)}(\omega) + C^{(0)}(\omega) \right\}, \end{aligned} \quad (\text{A49})$$

where the usual definitions of energy density, E_ν , energy flux, F_ν , and pressure, P_ν , of the neutrino field have been made, viz.,

$$E_\nu = \frac{4\pi}{(2\pi\hbar c)^3} \int_0^\infty \omega^3 \psi^{(0)}(\omega) d\omega, \quad (\text{A50})$$

$$F_\nu = \frac{4\pi}{(2\pi\hbar c)^3} \frac{c}{3} \int_0^\infty \omega^3 \psi^{(1)}(\omega) d\omega, \quad (\text{A51})$$

$$P_\nu = \frac{4\pi}{(2\pi\hbar c)^3} \frac{1}{3} \int_0^\infty \omega^3 \psi^{(0)}(\omega) d\omega = \frac{1}{3} E_\nu. \quad (\text{A52})$$

Equation (A49) requires that

$$\left(\frac{\partial E}{\partial t} \right)_{\text{mat} \rightarrow \nu} = \frac{4\pi c}{(2\pi\hbar c)^3} \int_0^\infty \omega^3 d\omega \{ j(\omega) - [j(\omega) - 1/\lambda^{(a)}(\omega) - A^{(0)}(\omega)] \psi^{(0)}(\omega) + B^{(0)}(\omega) \psi^{(1)}(\omega) + C^{(0)}(\omega) \}, \quad (\text{A53})$$

where $(\partial E/\partial t)_{\text{mat} \rightarrow \nu}$ is the net rate of energy transfer per unit volume from matter to neutrinos due to absorption, emission, scattering, and thermal processes, but not due to the matter velocity field. Terms accounting for the latter are introduced in the transformation of the left-hand side of the Boltzmann transport equation (i.e., the streaming terms) from the Eulerian to the fluid frame. Such a term, suitably metamorphosed, is the third term on the left-hand side of equation (A49), i.e., $-\rho P_\nu \partial(1/\rho)/\partial t$ is the rate of energy transfer per unit volume from matter to neutrinos due to the matter velocity field.

The equation for the matter analogous to equation (A49) is

$$\frac{\partial}{\partial t} \left(\frac{E}{\rho} \right) + P \frac{\partial}{\partial t} \left(\frac{1}{\rho} \right) = \frac{1}{\rho} \left(\frac{\partial E}{\partial t} \right)_{\nu \rightarrow \text{mat}}, \quad (\text{A54})$$

where E and P are the energy density and pressure of the matter, and $(\partial E/\partial t)_{\nu \rightarrow \text{mat}}$ is the negative of expression (A53). Adding equation (A49) and (A54) yields the internal energy conservation equation for both matter and neutrinos:

$$\frac{\partial}{\partial t} \left(\frac{E}{\rho} + \frac{E_\nu}{\rho} \right) + (P + P_\nu) \frac{\partial}{\partial t} \left(\frac{1}{\rho} \right) + \frac{1}{\rho} \frac{1}{r^2} \frac{\partial}{\partial r} (r^2 F_\nu) = 0. \quad (\text{A55})$$

Applying the operator

$$\frac{4\pi}{3} \frac{1}{(2\pi\hbar c)^3} \int_0^\infty \omega^3 d\omega$$

on equation (A13) and neglecting the velocity-dependent terms in the brackets on the left-hand side [since they are $O(v^2/c^2)$ in the energy equation], we have

$$\frac{\partial P_\nu}{\partial r} = \frac{4\pi}{3(2\pi\hbar c)^3} \int_0^\infty \omega^3 d\omega [-\psi^{(1)}(\omega)/\lambda^{(t)}(\omega) + A^{(1)}(\omega) \psi^{(0)}(\omega) + C^{(1)}(\omega)], \quad (\text{A56})$$

where $\lambda^{(t)}(\omega)$ is given by equation (A26). Retention of the term $\partial\psi^{(1)}/\partial t$ in the derivation of equation (A13) would have resulted in an extra term on the left-hand side of equation (A56) corresponding to the time derivative of the neutrino field momentum density. The diffusion approximation neglects the momentum density of the neutrinos as it relates to their transport (but not as it relates to neutrino-matter momentum transfer). Equation (A56) requires that

$$(F)_{\text{mat} \rightarrow \nu} = \frac{4\pi}{3(2\pi\hbar c)^3} \int_0^\infty \omega^3 d\omega [-\psi^{(1)}(\omega)/\lambda^{(t)}(\omega) + A^{(1)}(\omega) \psi^{(0)}(\omega) + C^{(1)}(\omega)], \quad (\text{A57})$$

where $(F)_{\text{mat} \rightarrow \nu}$ is the matter-neutrino stress (rate of momentum transfer per unit volume from matter to neutrinos).

The inclusion of a flux limiter changes equation (A56) by the substitution of $\Lambda^{(t)}(\omega)$ for $\lambda^{(t)}(\omega)$ (see the discussion before and after eq. [A31]). The quantity $\partial P_\nu/\partial r$ is then no longer equal to the matter-neutrino stress, but is instead given by

$$\begin{aligned} \frac{\partial P_\nu}{\partial r} &= \int_0^\infty d\omega \eta(\omega) \frac{d(F)_{\text{mat} \rightarrow \nu}}{d\omega} \\ &= R^{-1}(F)_{\text{mat} \rightarrow \nu}, \end{aligned} \quad (\text{A58})$$

where R is defined by the second equality in equation (A58), and

$$\eta(\omega) = \frac{-\psi^{(1)}(\omega)/\Lambda^{(t)}(\omega) + A^{(1)}(\omega) \psi^{(0)}(\omega) + C^{(1)}(\omega)}{-\psi^{(1)}(\omega)/\lambda^{(t)}(\omega) + A^{(1)}(\omega) \psi^{(0)}(\omega) + C^{(1)}(\omega)}, \quad (\text{A59})$$

$$\frac{d(F)_{\text{mat} \rightarrow \nu}}{d\omega} = \frac{4\pi}{3(2\pi\hbar c)^3} \omega^3 [-\psi^{(1)}(\omega)/\lambda^{(t)}(\omega) + A^{(1)}(\omega) \psi^{(0)}(\omega) + C^{(1)}(\omega)]. \quad (\text{A60})$$

Multiplying the matter momentum equation by v/ρ , the conservation equation for mechanical energy is obtained, given by

$$\frac{\partial}{\partial t} \left[\frac{v^2}{2} - \frac{GM(r)}{r} \right] + \frac{1}{\rho} \frac{1}{r^2} \frac{\partial}{\partial r} (r^2 v P) - P \frac{\partial}{\partial t} \left(\frac{1}{\rho} \right) = \frac{v}{\rho} (F)_{\nu \rightarrow \text{mat}}, \quad (\text{A61})$$

where $(F)_{\nu \rightarrow \text{mat}}$, the neutrino-matter stress, is the negative of (A57). Eliminating the right-hand side of equation (A60) by equation (A58) results in

$$\frac{\partial}{\partial t} \left[\frac{v^2}{2} - \frac{GM(r)}{r} \right] + \frac{1}{\rho} \frac{1}{r^2} \frac{\partial}{\partial r} (r^2 v P) - P \frac{\partial}{\partial t} \left(\frac{1}{\rho} \right) = R \frac{1}{\rho} \frac{1}{r^2} \frac{\partial}{\partial r} (r^2 v P_\nu) + RP_\nu \frac{\partial}{\partial t} \left(\frac{1}{\rho} \right). \quad (\text{A62})$$

Adding equation (A61) to equation (A55) gives the equation of overall energy conservation,

$$\frac{\partial}{\partial t} \left[\frac{E}{\rho} + \frac{E_\nu}{\rho} + \frac{v^2}{2} - \frac{GM(r)}{r} \right] + \frac{1}{\rho} \frac{1}{r^2} \frac{\partial}{\partial r} [r^2 v (P + RP_\nu)] + P_\nu (1 - R) \frac{\partial}{\partial t} \left(\frac{1}{\rho} \right) + \frac{1}{\rho} \frac{1}{r^2} \frac{\partial}{\partial r} (r^2 F_\nu) = 0. \quad (\text{A63})$$

The next to last term in equation (A63) should be zero, since it represents the rate of work done by matter on neutrinos minus that done by neutrinos on matter. The inconsistency arose with the introduction of the flux limiter in equation (A56), and is expected to be serious when the flux limiter deviates significantly from unity. This occurs in the outer, neutrino-transparent regions of the core. In limiting the neutrino flux in neutrino-transparent regions, the flux limiter quite correctly reduces the momentum transfer rate between matter and neutrinos. This reduction does not appear in the third term on the left-hand side of equation (A49), since the latter is derived from the third term on the left-hand side of equation (A12), which has its origin in the velocity field of the matter and is unaffected by the flux limiter. Therein lies the inconsistency. This inconsistency will be eliminated by the introduction of a similar factor of R in the differencing of this latter term, as will be discussed in Appendix B.

APPENDIX B

NUMERICAL TREATMENT OF THE NEUTRINO EVOLUTION EQUATION

In this appendix the numerical treatment of the neutrino evolution equations is discussed. These equations are the MGFLDA equations discussed in Appendix A and consisting of equations (A25) and (A27) with equation (A31), and several additional equations introduced below to complete the system. The numerical scheme to be described was applied separately to electron neutrinos, electron antineutrinos, and the thermal neutrinos (viz., ν_μ and ν_τ pairs). The absorption, emission, scattering, and thermal production rates used for each of the above neutrino types will be derived in Appendix C.

The neutrino evolution equations for different neutrino types are coupled to each other and to the hydrodynamic equations through the neutrino-matter interaction terms by the effect and dependence of the latter on the temperature and electron fraction of the matter. An additional coupling between each neutrino and antineutrino field arises from the thermal production and absorption of neutrino-antineutrino pairs. (Neutrino-neutrino scattering, predicted by the standard model, and other models, of weak interactions couple all neutrino fields directly, but this process is not considered here.) Finally, for each neutrino field the neutrino occupation probabilities in different spatial zones are coupled by the diffusion terms in the evolution equation, and in different energy zones by the neutrino-electron scattering terms. The number of coupled unknowns to be solved for is thus very large. If N_M is the number of radial mass zones (typically 50–100) and N_E is the number of energy zones (typically about 10) for each neutrino type, then there are N_M temperatures, N_M electron fractions (which are coupled to the absorption and emission of electron-type neutrinos and antineutrinos), and $N_M \times N_E$ neutrino occupation numbers for each neutrino type to solve for at each time step.

Care must be exercised in the choice of the numerical scheme used to advance the solution of the neutrino evolution equations. The large number of unknowns involved would tend to suggest that an explicit scheme which solves for each of the unknowns independently of the others would be the appropriate scheme to adopt. However, the maintenance of numerical stability with such a scheme would impose prohibitively small time steps on the forward time-integration of the solution. The neutrino diffusion terms, for example, would impose the time-step restriction $\Delta t \leq \tau_C (c_s/c)[3\Delta r/\lambda(r)]$, where τ_C is the Courant time, c_s/c is the ratio of the speed of sound to that of light, and $\lambda^{(t)}$ is the effective neutrino mean free path given by equation (A26). The permissible time step would become extremely small in the neutrino-transparent regions. (The flux limiter could modify this stability criterion, but experience indicates that it is still severe.)

Problems also arise with the neutrino-matter interaction terms. Consider electron-type neutrino absorption and emission. The net rate of change of electron fraction due to capture on free protons is

$$\dot{Y}_{e,p} = -3.6 \times 10^{-3} X_p (\mu_e^5 - \mu_\nu^5) (1 - e^{-\Delta/kT})$$

(e.g., Bludman, Lichtenstadt, and Hayden 1982), where $\Delta = \mu_e - \mu_\nu - \mu_n + \mu_p$, and μ_i is the chemical of species i (in MeV). Using

$\mu_e \approx 5.1 \times 10^{-3} (\rho Y_e)^{1/3}$, and assuming a proton mass fraction $X_p = 10^{-3}$, it is seen that the electron fraction change time scale, $|Y_e/\dot{Y}_{e,p}|$, for unblocked electron capture becomes of the order of microseconds for $\rho Y_e = 3 \times 10^{13} \text{ g cm}^{-3}$. This is already shorter than the Courant time step encountered at bounce. Even shorter time scales can result from considering neutrino absorption lifetimes in the higher energy zones. Clearly, the numerical treatment of neutrino absorption and emission cannot be explicit.

The neutrino absorption and emission process does not strongly couple neutrinos in different energy zones, the coupling being only through changes in T and Y_e . It is therefore possible to solve implicitly for the neutrino occupation probabilities in each energy zone (and all mass zones) separately. Efficient elimination schemes avoid the necessity of inverting large matrices (e.g., Lund and Wilson 1980). This procedure will not work if processes which strongly couple neutrinos in different energy zones are considered. Neutrino-electron scattering is such a process. The lifetime of a high-energy neutrino ($\omega \gg \mu_e$) against scattering off relativistic, degenerate electrons is $1/\langle\sigma\rangle n_e c \approx 3 \times 10^{-4}/\omega$ s for $\rho Y_e = 3 \times 10^{11} \text{ g cm}^{-3}$, where ω is the neutrino energy in MeV, $\omega \gg 35$ MeV, and equation (31a) of Tubbs and Schramm (1975) was used for $\langle\sigma\rangle$. An explicit numerical treatment of neutrino-electron scattering would thus already impose severe time step restrictions at $\rho Y_e = 3 \times 10^{11} \text{ g cm}^{-3}$.

The approach by other recent multineutrino energy numerical studies of gravitational collapse has been to use an implicit neutrino diffusion scheme for the neutrinos in each energy zone, and, to avoid the need for implicitly coupling zones of different energy, an approximate treatment of neutrino-electron scattering, the latter being either a Fokker-Planck algorithm (Bowers and Wilson 1982a) or a thermal relaxation algorithm (Arnett 1977a; Wilson 1980). However, Tubbs *et al.* (1980) have shown that these approximations yield reasonable agreement with Monte Carlo results only over a relatively restricted temperature and density regime, the regime depending on the parameters used in the approximation. In view of this, the approach taken here was to sacrifice numerical efficiency and directly solve the source terms on the right-hand side of the MGFLDA, implicitly coupling all mass and energy zones. This resulted in good agreement with the Monte Carlo results for neutrino-electron scattering of Tubbs *et al.* (1980) in most cases (see Appendix E). Another advantage of this approach (or any approach involving implicit differencing of the neutrino equations) has to do with the fact that the neutrino states in the lower energy zones become almost completely filled in the highly neutrino-opaque region that develops in the inner part of the core during collapse. Implicit differencing of the neutrino evolution equations results in this condition being approached smoothly and without overshoot. An obvious disadvantage of this approach is that an implicit calculation involving many unknowns presents a considerable chore for the computer, so that fewer collapse calculations can be performed with a given amount of computer time.

While the goal was to solve for the zero and first moments of the neutrino occupation numbers of all neutrino types simultaneously and implicitly, in practice it was found expedient to obtain an implicit solution for the zeroth moments of each neutrino type separately, the first moments being then obtained explicitly from equation (A25). The calculation was sequenced as illustrated by the block diagram in Figure 33. The cycle begins with the updating of the densities and temperatures of the matter as dictated by the matter hydrodynamics. (The numerical scheme for the hydrodynamics is explicit, and is discussed in Appendix D.) The change in the zeroth moments of the neutrino occupation numbers for each neutrino type due to the compression or expansion of the matter is then calculated. (The equations governing this process are purely algebraic, and no stability problems arise.) Next, the change in the temperatures and electron fractions of the matter and the change in the zeroth moments of the neutrino occupation numbers due to the combined effects of neutrino absorption, emission, scattering, thermal processes, and transport are computed successively for electron neutrinos, electron antineutrinos, and thermal neutrinos. Finally, the first moments of the neutrino occupation numbers are calculated.

The procedure for updating the zeroth and first moments of the neutrino occupation numbers of each neutrino type as described above requires some comment. The problems associated with the explicit calculation of the first moments of the neutrino occupation numbers are discussed in the last section of this appendix. Here we discuss the sequencing of the solution for the different neutrino types. Neutrinos of different types are coupled through their effect and dependence on the temperature and electron fraction of the matter, and through the thermal production and absorption terms. Inaccuracies and potential stability problems introduced by this sequencing because of the coupling of each neutrino type to the temperature and electron fraction of the matter were kept small by restricting the percentage time-step change in the latter quantities by appropriate time-step criteria. (The actual criteria used were $d \ln T \leq 0.01$ and $d \ln Y_e \leq 0.01$.) The coupling of neutrinos to antineutrinos through the thermal production and absorption terms is stronger than through T and Y_e , and the sequencing could give rise to more severe stability problems. In the case of the thermal neutrinos this problem did not arise. The thermal neutrino and antineutrino distributions were represented by the same function in this work, so the updating of these distributions was not sequenced. The coupling was incorporated implicitly in the difference equations. In the case of the electron-type neutrino and antineutrino distributions, the sequencing of their solution prevented their coupling from being incorporated implicitly. Stability problems never arose, but to be conservative they were further suppressed by time-step restrictions that kept the fractional change of the neutrino or antineutrino occupation probability in any mass and energy zone from exceeding 0.1, provided that the occupation probability itself exceeded 0.01. This restriction was gradually removed for smaller occupation probabilities, becoming absent for occupation probabilities smaller than 0.001. These time-step restrictions were not severe in practice because of the relative slowness of the thermal production process under the conditions encountered in the core-collapse problems considered here. Thus, for example, the time required to attain a thermal equilibrium electron-type neutrino distribution by thermal production is about $13/T^5$ s, where T is in MeV (cf. eq. [15.1] of Bethe, Applegate, and Brown 1980). This time is about 0.1 ms for $T = 10$ MeV, but increases very quickly with decreasing temperature and is about 4 ms for $T = 5$ MeV.

In the following, the numerical scheme used to advance the neutrino occupation probability of each neutrino type with the compression or expansion of the matter is first described. The numerical scheme used to obtain simultaneous implicit solutions of

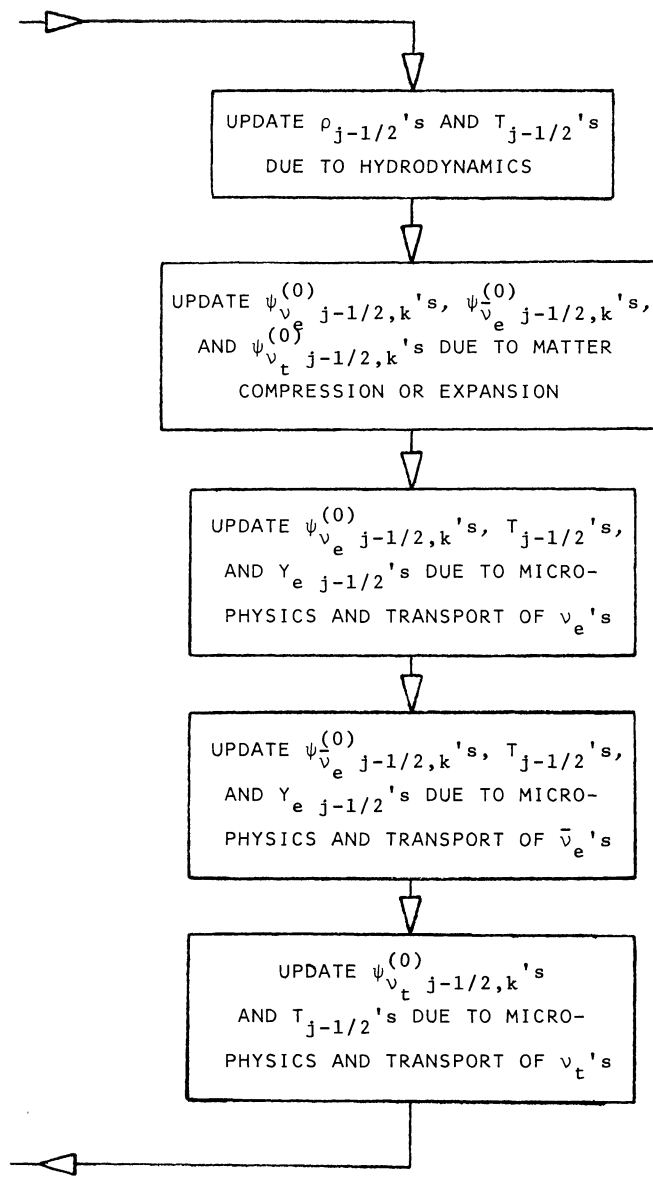


FIG. 33.—The sequencing of the solution for the $\rho_{j-1/2}$, $T_{j-1/2}$, $(Y_e)_{j-1/2}$, and $(\psi_{\nu_i}^{(0)})_{j-1/2,k}$. The solution for the $(\psi_{\nu_i}^{(1)})_{j-1/2,k}$ directly follows the solution for the $(\psi_{\nu_i}^{(0)})_{j-1/2,k}$.

the matter temperatures, electron fractions, and occupation probabilities for a given neutrino type due to absorption, emission, scattering, thermal production, and transport (hereafter referred to as microphysics and transport) is then described. The following notation will be used. Quantities defined on the edge of a mass shell will be represented with a subscript j , where $1 \leq j \leq N_M$, N_M being the number of mass zones. Quantities defined in the center of a mass shell will be denoted by a subscript $j - 1/2$. The energy spectrum of each neutrino type is divided into N_E energy zones of energy ω_k and energy width $\Delta\omega_k$, $1 \leq k \leq N_E$ ($\omega_k < \omega_{k+1}$). Quantities defined at neutrino energy ω_k will be written with a subscript k . Finally, quantities defined at time t^n (where t^n is the time after n time steps), t^{n+1} , or spanning the time from t^n to t^{n+1} will be written with a superscript n , $n+1$, or $n+1/2$, respectively.

I. CHANGE OF $\psi^{(0)}$ DUE TO MATTER COMPRESSION OR EXPANSION

The change in $\psi^{(0)}$ due to the compression or expansion of the matter is given by the third term, $D_v \psi^{(0)}$, on the left-hand side of the MGFLDA, equation (A27). We rewrite this term here for convenience:

$$D_v \psi^{(0)} = \frac{1}{3c} \frac{\partial \ln \rho}{\partial t} \left(\omega \frac{\partial}{\partial \omega} \psi^{(0)} \right), \quad (\text{B1})$$

where $\psi^{(0)} = \psi^{(0)}(r, t, \omega)$ is the zero-order moment of the neutrino occupation number, and ω is the neutrino energy. The significance of this term can be appreciated if we isolate it in the MGFLDA by turning off all nonconservative neutrino-matter interactions (so that the right-hand side of the MGFLDA vanishes), and consider the limit of small isoenergetic scattering mean free paths (which results in the vanishing of the second term on the left-hand side of the MGFLDA, eq. [A31]). In this limit the MGFLDA reduces to

$$\frac{1}{c} \frac{\partial \omega^{(0)}}{\partial t} + \frac{1}{3c} \frac{\partial \ln \rho}{\partial t} \left(\omega \frac{\partial}{\partial \omega} \psi^{(0)} \right) = 0. \quad (\text{B2})$$

The solution of this equation is

$$\psi^{(0)}(t, r, \omega) = \psi^{(0)}(t_i, r, \omega \rho_i^{1/3} / \rho_i^{1/3}), \quad (\text{B3})$$

where ρ_i is the material density at some initial time t_i . Recalling that r is a Lagrangian coordinate, we see that equation (B3) states that the number of neutrinos in a given mass element is conserved and that their energies change with time in accordance with

$$\omega(t) \propto [\rho(t)]^{1/3}. \quad (\text{B4})$$

This result is not surprising, since this is just how an isotropically distributed relativistic gas behaves under an adiabatic change of volume.

When the neutrino mean free paths become large compared with other relevant length scales, the term (B1) in the MGFLDA is not expected to correctly describe the behavior of $\psi^{(0)}$ under a compression or an expansion of the matter. In the limit of infinite neutrino mean free paths, for example, the neutrinos would exert no stress on the matter and, contrary to the implication of equation (B1), the matter would do no work on the neutrinos. The problem with equation (B1) stems from the fact that, like the other terms in the diffusion equation, its derivation from the Boltzmann equation involved only the lowest order moments of the latter. All moments of the Boltzmann equation become important when the neutrino mean free paths are large, however. In the MGFLDA, the transition from diffusion to the limit of large mean free paths is accomplished by means of a flux limiter. In Appendix A it was shown that a consistent treatment of the energy exchange between matter and neutrinos for arbitrary neutrino mean free paths could be achieved by assuming that only a fraction, $\eta(r, \omega)$, of the neutrinos at r with energy ω are affected by the matter compression or expansion, i.e., that the evolution of $\psi^{(0)}$ for this fraction, $\eta(r, \omega)$, of neutrinos is described by equation (A27), and that the evolution of $\psi^{(0)}$ for the remaining fraction, $1 - \eta(r, \omega)$, is described by equation (A27) without the term (B1). (Hereafter the argument r will be omitted from η). The quantity $\eta(\omega)$ is unity in the very neutrino-opaque regions, where the neutrino mean free path is small and flux limiting is negligible, and approaches zero in the very neutrino-transparent regions, where flux limiting is very important.

The total energy of the neutrinos trapped inside a collapsing stellar core can reach values of the order of 10^{52} ergs at maximum compression. Because of the rather coarse zoning of the neutrino energy (i.e., typically 10 energy zones as compared with ~ 50 –100 mass zones), a difference scheme for equation (B2) that is not explicitly designed to conserve neutrino number exactly and to ensure the proper neutrino energy behavior given by equation (B4) could be inaccurate enough to distort the calculation significantly. Another constraint that must be satisfied is the Pauli exclusion principle requirement that $\psi^{(0)}(\omega)$ not exceed unity. A final constraint is that only a fraction $\eta(\omega)$, given by equation (A59), of the neutrinos of energy ω are affected by the matter compression or expansion in order that the energy exchange between matter and neutrinos be treated consistently. A difference scheme satisfying all of the above criteria will now be described. The treatment of the fraction $\eta(\omega)$ of neutrinos affected by the matter compression or expansion will first be derived, followed by a discussion of the treatment of the remaining fraction, $1 - \eta(\omega)$, of neutrinos unaffected by the matter compression or expansion.

Consider the neutrinos in a given mass zone $j - 1/2$ (i.e., enclosed between zones $j - 1$ and j), energy zone k , at the time cycle n [hereafter referred to as the $(j - 1/2, k, n)$ neutrinos], and consider their behavior under matter compression. In the absence of microphysics and transport, the number of $(j - 1/2, k, n)$ neutrinos is conserved. Under compression, however, some of the $(j - 1/2, k, n)$ neutrinos will be transferred to the $k + 1$ energy zone so that the correct average energy behavior, expressed by equation (B4), will occur. Conservation of the fraction of the $(j - 1/2, k, n)$ neutrinos affected by the matter compression is ensured by writing

$$\begin{aligned} & \frac{4\pi}{(2\pi\hbar c)^3} \frac{M_{j-1/2}}{\rho_{j-1/2}^{n+1}} \left[\left(\eta_{j-1/2, k}^n \psi_{j-1/2, k}^{(0)n} - \delta^{(-)} \psi_{j-1/2, k}^{(0)n+1/2} \right) \omega_k^2 \Delta\omega_k + \delta^{(+)} \psi_{j-1/2, k+1}^{(0)n+1/2} \omega_{k+1}^2 \Delta\omega_{k+1} \right] \\ &= \frac{4\pi}{(2\pi\hbar c)^3} \frac{M_{j-1/2}}{\rho_{j-1/2}^n} \eta_{j-1/2, k}^n \psi_{j-1/2, k}^{(0)n} \omega_k^2 \Delta\omega_k, \end{aligned} \quad (\text{B5})$$

where $M_{j-1/2}$ and $\rho_{j-1/2}$ are, respectively, the rest mass and the rest mass density of the matter between $j - 1$ and j , $\delta^{(-)} \psi_{j-1/2, k}^{(0)n+1/2}$ and $\delta^{(+)} \psi_{j-1/2, k+1}^{(0)n+1/2}$ are, respectively, the amount by which $\psi_{j-1/2, k}^{(0)n}$ is decreased and $\psi_{j-1/2, k+1}^{(0)n}$ is increased during the time

interval from t^n to t^{n+1} as a result of the compression of the matter, and $\eta_{j-1/2,k}^n$ is the mass-zone-centered average of expression (A59). The algebraic sum of the first two terms on the left-hand side of equation (B5) gives the number of $(j-1/2, k, n)$ neutrinos affected by the matter compression that are still in $(j-1/2, k)$ at time cycle $n+1$; the third term gives the number of these neutrinos that become $(j-1/2, k+1)$ neutrinos by time cycle $n+1$; and the right-hand side of equation (B5) gives the number of $(j-1/2, k, n)$ neutrinos affected by the matter compression.

The correct average energy behavior of the $(j-1/2, k, n)$ neutrinos affected by the matter compression is ensured by writing

$$\begin{aligned} & \frac{4\pi}{(2\pi\hbar c)^3} \frac{M_{j-1/2}}{\rho_{j-1/2}^{n+1}} \left[\left(\eta_{j-1/2,k}^{(0)} - \delta^{(-)} \psi_{j-1/2,k}^{(0)n+1/2} \right) \omega_k^3 \Delta\omega_k + \delta^{(+)} \psi_{j-1/2,k+1}^{(0)n+1/2} \omega_{k+1}^3 \Delta\omega_{k+1} \right] \\ &= \left(\frac{\rho_{j-1/2}^{n+1}}{\rho_{j-1/2}^n} \right)^{1/3} \frac{4\pi}{(2\pi\hbar c)^3} \frac{M_{j-1/2}}{\rho_{j-1/2}^n} \eta_{j-1/2,k}^{(0)} \psi_{j-1/2,k}^{(0)n} - \frac{4\pi}{(2\pi\hbar c)^3} \frac{M_{j-1/2}}{\rho_{j-1/2}^{n+1}} \Delta^{(+)} \psi_{j-1/2,k}^{(0)n+1/2} \omega_k^2 \Delta\omega_k (\omega_k - \omega_{k-1}). \end{aligned} \quad (B6)$$

The algebraic sum of the first two terms on the left-hand side of equation (B6) gives the energy at time cycle $n+1$ of the $(j-1/2, k, n)$ neutrinos affected by the matter compression that are still in $(j-1/2, k)$ at $n+1$, the third term gives the energy at time cycle $n+1$ of the $(j-1/2, k, n)$ neutrinos affected by the matter compression that become $(j-1/2, k+1)$ neutrinos at $n+1$ and the first term on the right-hand side gives the energy at time cycle n of the $(j-1/2, k, n)$ neutrinos affected by the matter compression multiplied by the factor $(\rho_{j-1/2}^{n+1}/\rho_{j-1/2}^n)^{1/3}$ which accounts for the energy increase of these neutrinos, as dictated by equation (B4), in going from time cycle n to time cycle $n+1$. The quantity $\Delta^{(+)} \psi_{j-1/2,k}^{(0)n+1/2}$ is given by

$$\frac{4\pi}{(2\pi\hbar c)^3} \frac{M_{j-1/2}}{\rho_{j-1/2}^{n+1}} \left(\Delta^{(+)} \psi_{j-1/2,k}^{(0)n+1/2} \omega_k^2 \Delta\omega_k = \Delta^{(-)} \psi_{j-1/2,k-1}^{(0)n+1/2} \omega_{k-1}^2 \Delta\omega_{k-1} \right) \quad (B7)$$

and has the following significance. The numerical scheme for computing the change in the occupation probability of neutrinos in each energy zone due to matter compression or expansion begins, for each mass zone, with the lowest energy zone and works sequentially upward to the highest. The quantity $\Delta^{(-)} \psi_{j-1/2,k-1}^{(0)n+1/2}$ appearing in equation (B7) represents the amount by which the average occupation probability, $\psi_{j-1/2,k-1}^{(0)n+1/2}$, was computed to exceed unity in $(j-1/2, k-1)$ at time cycle $n+1$ as a result of the matter compression. The quantity $\Delta^{(-)} \psi_{j-1/2,k-1}^{(0)n+1/2}$ is zero if the occupation probability, $\psi_{j-1/2,k-1}^{(0)n+1}$, is not computed to exceed unity. The right-hand side of equation (B7) therefore represents the number of neutrinos that should have been added $(j-1/2, k-1)$ at time cycle $n+1$ but were added to $(j-1/2, k)$ instead to avoid violating the Pauli exclusion principle for $(j-1/2, k-1)$. The quantity $\Delta^{(+)} \psi_{j-1/2,k}^{(0)n+1/2}$ is the resulting change in $\psi_{j-1/2,k}^{(0)n+1}$. The energy error made by increasing $\psi_{j-1/2,k}^{(0)n+1}$ by $\Delta^{(+)} \psi_{j-1/2,k}^{(0)n+1/2}$ instead of increasing $\psi_{j-1/2,k-1}^{(0)n+1}$ by $\Delta^{(-)} \psi_{j-1/2,k-1}^{(0)n+1/2}$ is given by the positive magnitude of the last term on the right-hand side of equation (B6). This term is subtracted from the first term on the right-hand side of equation (B6) in order to eliminate this energy error. If $(j-1/2, k)$ is, in turn, computed to become overfilled at time cycle $n+1$, the neutrinos overfilling $(j-1/2, k)$ are added in a similar fashion to $(j-1/2, k+1)$, and so on, until, for high enough k , overfilling does not occur.

Solving equations (B5) and (B6) for the quantity $\delta^{(-)} \psi_{j-1/2,k}^{(0)n+1/2}$, and a similar set of equations with $k \rightarrow k-1$ for the quantity $\delta^{(+)} \psi_{j-1/2,k}^{(0)n+1/2}$, the net change, $\Delta \psi_{j-1/2,k}^{(0)n+1/2}$, in $\psi_{j-1/2,k}^{(0)n}$ in going from time step n to time step $n+1$ due to matter compression is given by

$$\begin{aligned} \Delta \psi_{j-1/2,k}^{(0)n+1/2} &= \delta^{(+)} \psi_{j-1/2,k}^{(0)n+1/2} - \delta^{(-)} \psi_{j-1/2,k}^{(0)n+1/2} + \Delta^{(+)} \psi_{j-1/2,k}^{(0)n+1/2} \\ &= (1 - \delta_{kN_E}) \left\{ \left(\frac{\rho^{n+1}}{\rho^n} - 1 - \frac{\omega_k}{\omega_{k+1}} \left[\left(\frac{\rho^{n+1}}{\rho^n} \right)^{4/3} - 1 \right] \right) \right. \\ &\quad \times \eta_k^n \psi_k^{(0)} \Big|_{j-1/2} \left(1 - \frac{\omega_k}{\omega_{k+1}} \right)^{-1} \\ &\quad + (1 - \delta_{k1}) \left\{ \left[\left(\frac{\rho^{n+1}}{\rho^n} \right)^{4/3} - \frac{\rho^{n+1}}{\rho^n} \right] \eta_{k-1}^n \psi_{k-1}^{(0)} \Big|_{j-1/2} \frac{\omega_{k-1}^3 \Delta\omega_{k-1}}{\omega_k^3 \Delta\omega_k} \frac{1 - \delta_{k(N_E-1)}}{1 - \omega_{k-1}/\omega_k} \right. \\ &\quad \left. + \Delta^{(+)} \psi_{j-1/2,k}^{(0)n+1/2} \frac{\omega_k - \omega_{k-1}}{\omega_{k+1} - \omega_k} (1 - \delta_{kN_E}) \right\} \\ &\quad - \delta_{k(N_E-1)} \left[\left(\frac{\rho^{n+1}}{\rho^n} \right)^{4/3} - \left(\frac{\rho^{n+1}}{\rho^n} \right) \right] \eta_{N_E}^n \psi_{N_E}^{(0)} \Big|_{j-1/2} \frac{\omega_{N_E}^2 \Delta\omega_{N_E}}{\omega_{N_E-1}^2 \Delta\omega_{N_E-1}} \left(1 - \frac{\omega_{N_E-1}}{\omega_{N_E}} \right)^{-1} \\ &\quad - (1 - \delta_{k1})(1 - \delta_{k2}) \Delta^{(+)} \psi_{j-1/2,k-1}^{(0)n+1/2} \frac{\omega_{k-1} - \omega_{k-2}}{\omega_k - \omega_{k-1}} \frac{\omega_{k-1}^2 \Delta\omega_{k-1}}{\omega_k^2 \Delta\omega_k} + (1 - \delta_{k1}) \Delta^{(+)} \psi_{j-1/2,k}^{(0)n+1/2} \\ &\quad + \delta_{kN_E} \left\{ \left[\left(\frac{\rho^{n+1}}{\rho^n} \right)^{4/3} - \frac{\rho^{n+1}}{\rho^n} \right] \left(1 - \frac{\omega_{N_E-1}}{\omega_{N_E}} \right)^{-1} + \left(\frac{\rho^{n+1}}{\rho^n} - 1 \right) \right\} \\ &\quad \times \eta_{N_E}^n \psi_{N_E}^{(0)} \Big|_{j-1/2}, \end{aligned} \quad (B8)$$

where all factors standing to the left of the vertical lines with subscript $j - 1/2$ are understood to have that subscript affixed to them, when appropriate. A similar derivation for the case in which the zone $j - 1/2$ is expanding yields a result that can be obtained from equation (B8) by the substitutions $k - i \rightarrow k + i$, $N - i \rightarrow 1 + i$, and $1 + i \rightarrow N - i$ ($i = -1, 0$, or 1 as is appropriate) for all terms not involving $\Delta^{(+)}\psi_{j-1/2}^{(0)}$. Terms involving $\Delta^{(+)}\psi_{j-1/2}^{(0)}$ are unchanged.

Consider now the fraction, $1 - \eta(\omega)$, of neutrinos unaffected by the matter compression or expansion. It was argued above that a consistent treatment of neutrino-matter energy exchange requires that the evolution of $\psi^{(0)}$ for this fraction of the neutrinos should be described by equation (A27) without the last term (viz., expression [B1]) on the left-hand side. The remaining terms on the left-hand side of this equation (with $\lambda^{(t)}$ replaced by $\Lambda^{(t)}$) are just the flux-limited diffusion terms appropriate for a fixed reference frame. Equation (A27) (with the last term on the left-hand side omitted) is inconsistent as it stands because the terms on the right-hand side are tied to the moving matter. As discussed before, the last term on the left-hand side of equation (A27) corrects, when included, for the motion of the matter only in the region of small neutrino mean free paths. In contrast, equation (A27) (with the last term on the left-hand side omitted) can be expected to give an accurate description of $\psi^{(0)}$ in a fixed frame in the limit of large neutrino mean free paths [which is when the quantity $1 - \eta(\omega)$ becomes significant] because the terms on the right-hand side are small in this limit and do not appreciably influence the description.

When equation (A27) (with the last term on the left-hand side omitted) is differenced, however, it is with respect to a moving frame. Now the change in $\psi^{(0)}$ in a given mass zone depends, in part, on the flux of neutrinos through the inner and outer surfaces of that zone. A correction must be made to account for the fact that these surfaces are moving with the matter while the flux of the fraction, $1 - \eta(\omega)$, of the neutrinos considered here is computed for a fixed reference frame. To order v/c , the number flux F'_k of neutrinos in the k th energy zone that traverse a surface moving with the matter is given in terms of quantities referred to the fixed frame by

$$\begin{aligned} F'_k &= \frac{2\pi c}{(2\pi\hbar c)^3} \int_{-1}^1 \omega_k'^2 \Delta\omega_k f'(\omega', \mu') \mu' d\mu' \\ &= \frac{2\pi c}{(2\pi\hbar c)^3} \int_{-1}^1 \omega_k^2 \Delta\omega_k \left(1 - 3\frac{v}{c}\mu\right) f(\omega, u) \left[\mu - \frac{v}{c}(1 - \mu^2)\right] \left(1 + 2\frac{v}{c}\mu\right) d\mu \\ &= \frac{4\pi c}{3(2\pi\hbar c)^3} \omega_k^2 \Delta\omega_k \left(\psi^{(1)} - 3\frac{v}{c}\psi^{(0)}\right), \end{aligned} \quad (\text{B9})$$

where the unprimed and primed quantities refer to the fixed and matter frame, respectively; the Lorentz invariance of the neutrino occupation probability, $f(\omega, \mu)$, has been used; and the expansion (A10) of $f(\omega, \mu)$ has been used. Equation (B9) is the expression that is used here to compute the number flux of the fraction, $1 - \eta(\omega)$, of neutrinos unaffected by the matter compression or expansion through the moving mass-zone boundaries.

II. CHANGE IN $\psi^{(0)}$, $\psi^{(1)}$, T , AND Y_e DUE TO MICROPHYSICS AND TRANSPORT

The equations describing the evolution of $\psi^{(0)}$ and $\psi^{(1)}$ for each neutrino type are the MGFLDA equations (A25), (A27), and (A31), without the last term on the left-hand side of equation (A27). This latter term gives the change in $\psi^{(0)}$ due to the compression or expansion of the matter, and its numerical treatment has been the subject of the preceding section. In obtaining the solutions of equations (A25), (A27), and (A31) for $\psi^{(0)}$ and $\psi^{(1)}$, it is convenient to simultaneously and additionally obtain the change in the temperature T and the electron fraction Y_e of the matter due to neutrino-matter interactions. This requires that equations (A25), (A27), and (A31) be supplemented by two additional equations. One of these additional equations can be taken to be equation (A54) without the second term on the left-hand side, i.e.,

$$\frac{\partial}{\partial t} \left(\frac{E}{\rho} \right) = \frac{1}{\rho} \left(\frac{\partial E}{\partial t} \right)_{\nu \rightarrow \text{mat}} \quad (\text{B10})$$

where, as before, E and ρ denote the energy density and the rest-mass density of the matter, and where the right-hand side of equation (B10) is given by the negative of the right-hand side of equation (A53). The second term on the left-hand side of equation (A54) which we neglect here is used elsewhere to advance the matter temperature in accordance with hydrodynamics. Equation (B10) can be rewritten in the following more convenient form:

$$\frac{\partial}{\partial T} \left(\frac{E}{\rho} \right) \frac{\partial T}{\partial t} + \frac{\partial}{\partial Y_e} \left(\frac{E}{\rho} \right) \frac{\partial Y_e}{\partial t} = \frac{1}{\rho} \left(\frac{\partial E}{\partial t} \right)_{\nu \rightarrow \text{mat}}, \quad (\text{B11})$$

which gives a relation between the change in Y_e and the change in T . The form of equation (B11) is justified by the assumption that the matter is in nuclear statistical equilibrium and therefore the energy density E of the matter depends only on ρ , T , and Y_e . The matter density ρ does not change in this phase of the calculation.

The second additional equation needed is one giving the change in Y_e due to the absorption and emission of neutrinos. This equation is a consequence of lepton number conservation, i.e., the fact that the absorption of an electron-type neutrino or

antineutrino gives rise to an electron or a positron, respectively, and is given by

$$\frac{\partial Y_e}{\partial t} = \epsilon \frac{1}{N_A \rho} \frac{4\pi}{(2\pi\hbar c)^3} \int_0^\infty \omega^2 d\omega \left\{ j(\omega) [1 - \psi^{(0)}(\omega)] - \frac{\psi^{(0)}(\omega)}{\lambda^{(a)}(\omega)} \right\}, \quad (\text{B12})$$

where N_A is Avogadro's number, $j(\omega)$ and $\lambda^{(a)}(\omega)$ are defined in equation (A5) and derived in Appendix C, and ϵ is 1 for electron neutrinos, -1 for electron antineutrinos, and zero for the thermal neutrinos. The absorption and emission of muon and tau neutrinos can occur by processes such as $\nu_\mu + n \rightleftharpoons \mu^- + p$ and $\nu_\tau + n \rightleftharpoons \tau^- + p$. For the former reaction to proceed to the right, the temperature or one of the particle chemical potentials must be of the order of $m_\mu c^2 = 106$ MeV, neither of which occurs in the stages of the core collapse considered here. For the reaction to proceed to the left, muons must be present. Thermally produced muon pairs will have a number fraction (muon-to-baryon ratio) of $3 \times 10^{-4} (T^{3/2}/\rho_{14}) \exp(-105.66/T)$, where the temperature T is in MeV. For typical core-collapse trajectories the muon number fraction is a maximum in the deep core and never exceeds about 10^{-4} . Muons can also be produced by reactions of the type $\bar{\nu}_e + e^- \rightarrow \bar{\nu}_\mu + \mu^-$ when the electron chemical potential exceeds $m_\mu c^2$, as it does in the deep core. However, the electron antineutrino number fraction is very small there. If this process were to proceed at a significant rate, it would thermalize some of the tremendous electron zero-point energy with potentially important dynamical consequences. Processes involving muons or taus in initial or final states are ignored here, although the possible influence of muonic processes (the taus are too massive to be important here) on the dynamics of core collapse has not been adequately explored to the author's knowledge. Referring to equation (B12) again, to be rigorous the quantity Y_e ($= Y_{e^-}$) on the left-hand side should be replaced by $Y_{e^-} - Y_{e^+}$. However, positrons are highly suppressed in the very electron-degenerate conditions encountered here, so $Y_{e^+} \ll Y_{e^-}$, and the replacement of Y_e by $Y_{e^-} - Y_{e^+}$ is not necessary. The production of a positron is quickly followed by its annihilation with an electron, the net result being the disappearance of an electron.

The following difference scheme is used for each neutrino type to advance $\psi^{(0)}$, T , and Y_e as dictated by equations (A27), (A31), (B11), and (B12). Let $U_{j,k}^{n+1/2}$ denote the solution matrix for a given neutrino type for the time step $t^n \rightarrow t^{n+1}$, that is,

$$U_{j,k}^{n+1/2} = \begin{cases} \Delta \psi_{j-1/2,k}^{(0)n+1/2}, & 1 \leq k \leq N_E, \quad 2 \leq j \leq N_M \\ \Delta T_{j-1/2}^{n+1/2}, & k = N_E + 1, \quad 2 \leq j \leq N_M \\ \Delta (Y_e)_{j-1/2}^{n+1/2}, & k = N_E + 2, \quad 2 \leq j \leq N_M, \end{cases} \quad (\text{B13})$$

where $\Delta \psi_{j-1/2,k}^{(0)n+1/2}$, $\Delta T_{j-1/2}^{n+1/2}$, and $\Delta (Y_e)_{j-1/2}^{n+1/2}$ are the changes, respectively, in $\psi_{j-1/2,k}^{(0)}$, $T_{j-1/2}$, and $(Y_e)_{j-1/2}$ during this time step. The difference equations for $U_{j,k}^{n+1/2}$ were obtained by backward differencing equations (A27), (A31), (B11), and (B12). These difference equations couple the energy zones corresponding to each mass zone through the right-hand sides of equations (B11) and (B12), and through the neutrino-electron scattering terms on the right-hand side of equation (A27). In addition, these equations couple each mass zone to the two adjacent mass zones through the radial derivatives appearing on the left-hand side of equation (A27). The $U_{j,k}^{n+1/2}$ thus satisfy a difference equation of the form

$$\sum_{k'=1}^{N_E+2} A_{j,k,k'}^n U_{j,k'}^{n+1/2} + D_{j,k}^n U_{j-1,k}^{n+1/2} + E_{j,k}^n U_{j+1,k}^{n+1/2} + C_{j,k}^n = 0, \quad (\text{B14})$$

where $A_{j,k,k'}^n$, $D_{j,k}^n$, $E_{j,k}^n$, and $C_{j,k}^n$ are numerical coefficients obtained from equations (A27), (A31), (B11), and (B12). As a consequence of the backward differencing, these coefficients also involve the derivatives at time t^n of the right-hand sides of equations (A27), (B11), and (B12) with respect to T , Y_e , and $\psi_k^{(0)}$. These derivatives were obtained numerically by center differencing when analytic expressions were unobtainable. Note that the quantities $D_{j,k}^n$ and $E_{j,k}^n$ are zero for $N_E + 1 \leq k \leq N_E + 2$, since neither equation (B11) nor equation (B12), from which these quantities were derived, couple adjacent mass zones.

As it stands, equation (B14) represents $N_M \times (N_E + 2)$ coupled equations. The form of the coupling makes possible an elimination scheme which renders the solution of equation (B14) practicable. The derivation of this scheme begins with the following assumed recursion equation for the $U_{j,k}^{n+1/2}$:

$$\sum_{k'=1}^{N_E+2} R_{j-1,k,k'}^n U_{j,k'}^{n+1/2} + S_{j-1,k}^n = U_{j-1,k}^{n+1/2}. \quad (\text{B15})$$

Substitution of equation (B15) in equation (B14) to eliminate the term involving $U_{j-1,k}^{n+1/2}$ yields

$$E_{j,k}^n U_{j+1,k}^{n+1/2} + D_{j,k}^n S_{j-1,k}^n + C_{j,k}^n = - \sum_{k'=1}^{N_E+2} B_{j,k,k'}^n U_{j,k'}^{n+1/2}, \quad (\text{B16})$$

where

$$B_{j,k,k'}^n = A_{j,k,k'}^n + D_{j,k}^n R_{j-1,k,k'}^n. \quad (\text{B17})$$

A comparison of equations (B16) and (B15) (with $j+1$ for j in the latter) results in

$$R_{j,k,k'} = -\left(B_{j,k',k}^{-1}\right)^n E_{j,k'}^n \quad (\text{B18})$$

and

$$S_{j,k}^n = -\sum_{k'=1}^{N_E+2} \left(B_{j,k',k}^{-1}\right)^n \left(D_{j,k'}^n S_{j-1,k'} + C_{j,k'}\right), \quad (\text{B19})$$

where $(B_{j,k',k}^{-1})^n$ is defined by the relation

$$\sum_{k'=1}^{N_E+2} \left(B_{j,k',k}^{-1}\right)^n B_{j,k',k''}^n = \delta_{k,k''}. \quad (\text{B20})$$

The procedure for computing the solution matrix, $U_{j,k}^{n+1/2}$, begins with the computation of the arrays $A_{j,k,k'}^n$, $D_{j,k}^n$, $E_{j,k}^n$, and $C_{j,k}^n$. Then beginning at $j=2$, the matrix $B_{2,k,k'}$ given by

$$B_{2,k,k'}^n = A_{2,k,k'}^n \quad (\text{B21})$$

is inverted so that $R_{2,k,k'}$ and $S_{2,k}$ may be obtained from the equations

$$R_{2,k,k'}^n = -\left(B_{2,k',k}^{-1}\right)^n E_{j,k'}^n \quad (\text{B22})$$

and

$$S_{2,k}^n = -\sum_{k'=1}^{N_E+2} \left(B_{2,k',k}^{-1}\right)^n C_{2,k'}, \quad (\text{B23})$$

where equations (B21), (B22), and (B23) are derived, respectively, from equations (B17), (B18), and (B19) with $j=2$ and with $D_{2,k}$ set to zero. (The quantities $D_{2,k}$, relating $U_{2,k}$ to $U_{1,k}$, are set to zero as a consequence of the central boundary condition; see below.) Equation (B17) is then used to compute $B_{3,k,k'}$ which, after inversion, is used to compute $R_{3,k,k'}$ and $S_{3,k}$ from equations (B18) and (B19), respectively. The procedure continues until all the elements of the arrays $R_{j,k,k'}$ and $S_{j,k}$ have been computed. Equation (B15) and the surface boundary condition (discussed below) provide, for each k in the range $1 \leq k \leq N_E$, two equations relating $U_{N_M+1,k}^{n+1/2}$ and $U_{N_M,k}^{n+1/2}$ from which $U_{N_M,k}^{n+1/2}$ can be obtained. (The quantity $U_{N_M+1,k}^{n+1/2}$ is $\Delta\psi_{N_M+1/2,k}^{(0)n+1/2}$, the change in $\psi_{N_M+1/2,k}^{(0)n}$ during $\Delta t^{n+1/2}$, where $\psi_{N_M+1/2,k}^{(0)n}$ is defined at a subsidiary mass zone just outside the outer boundary of the mass grid.) The quantities $U_{N_M,k}^{n+1/2}$ for $N_E+1 \leq k \leq N_E+2$ can be obtained directly from equation (B15) without knowledge of the corresponding $U_{N_M+1,k}^{n+1/2}$, since adjacent mass zones are uncoupled for these values of k and the $R_{N_M,k,k'}$ are therefore zero. Having computed the $U_{N_M,k}^{n+1/2}$, we then compute the rest of the $U_{j,k}^{n+1/2}$ for $j < N_M$ recursively using equation (B15).

III. BOUNDARY CONDITIONS

The MGFLDA is second order in space and therefore requires two boundary conditions for each energy group. Physical considerations dictate that one boundary condition be given at the center and the other at the surface. The central boundary condition is trivial; the area of the inner surface of the central mass shell is zero, so the neutrino flux across this surface is taken to be zero. (Symmetry considerations would also require this boundary condition.) This is accomplished by setting $D_{2,k}$ to zero in equations (B17) and (B19).

The surface boundary condition is more tricky. The simple angular dependence of the neutrino occupation probability prescribed by the MGFLDA and given by equation (A10) means that a number of physically reasonable conditions that one might wish to impose at the surface cannot be simultaneously satisfied. Thus, a standard condition imposed at the surface is the Marshak condition (Pomraning 1973), stating that the normal component of the inwardly directed flux be equal to that given by the exact conditions, which, in the present context, is zero. This would require that

$$0 = \int_{\mu < 0} \mu f(t, r, \mu, \omega) d\Omega = \int_{\mu < 0} \mu [\psi^{(0)}(t, r, \omega) + \mu \psi^{(1)}(t, R, \omega)] d\eta, \quad (\text{B24})$$

$$\psi^{(1)}(t, R, \omega) = \frac{3}{2} \psi^{(0)}(t, R, \omega), \quad (\text{B25})$$

where R is the radius of the surface and ω and μ are defined immediately below equation (A1). On the other hand, if most of the neutrinos flowing through the surface have undergone their last interaction much closer to the center (i.e., if the region of optical depth unity from the surface is at a radius $r \ll R$), then the neutrino distribution will be very forward-peaked. In the limit that $f(t, R, \mu, \omega) = K(t, R, \omega) \delta(1 - \mu)$, referred to as the radially streaming limit (δ is the Dirac delta function), it follows that

$$\psi^{(1)}(t, R, \omega) = 3\psi^{(0)}(t, R, \omega). \quad (\text{B26})$$

The problem is to choose the surface boundary condition from among a number of physically reasonable candidates. An *a priori* criterion for selection not being available, it was decided to subject a number of candidates to some steady state numerical tests. These are discussed in Appendix E. In the process it was found that the MGFLDA is remarkably insensitive to the exact surface boundary condition imposed, insofar as the results of the steady state numerical tests are representative. The solutions for $\psi^{(1)}$, which is related to the net flux, were almost independent of the surface boundary condition, while the solutions for $\psi^{(0)}$ were such as to produce the $\psi^{(1)}$, and differed from each other only near the surface. Far more important factors in producing accurate solutions seem to be the numerical treatment of the diffusion coefficient flux limiter (A31) (Bruenn, Buchler, and Yueh 1978a), and, possibly, the flux-limiting scheme itself. The flux-limiting scheme of Levermore and Pomraning (1981) is currently under investigation as a suitable scheme for neutrino transport during gravitational collapse.

The surface boundary condition used in the collapse calculations was taken to be

$$\psi_{N_M, k}^{(0)} = K_k \psi_{N_M, k}^{(1)}, \quad (\text{B27})$$

where

$$\psi_{N_M, k}^{(0)} = \frac{1}{2} \left(\psi_{N_M - 1/2, k}^{(0)} + \psi_{N_M + 1/2, k}^{(0)} \right), \quad (\text{B28})$$

$$K_k = 0.5774 \sin \theta_L + \frac{0.6667 \cos \theta_L}{1 + \cos \theta_L}, \quad (\text{B29})$$

$$\theta_L = \sin^{-1}(d_k/R), \quad (\text{B30})$$

and d_k is given by the solution of the equation

$$\int_{d_k}^R \frac{dr}{\lambda_k(r)} = \frac{2}{3} \quad (0 \leq d_k \leq R), \quad (\text{B31})$$

where $\lambda_k(r)$ is the neutrino mean free path at radius r and neutrino energy ω_k . The quantity $\psi_{N_M + 1/2, k}^{(0)}$ is defined on an extra “imaginary” mass zone just outside the outer boundary.

The function K_k has been chosen to give the exact relation between $\psi_{N_M, k}^{(0)}$ and $\psi_{N_M, k}^{(1)}$ in two limiting cases represented by $d_k = R$ and $d_k = 0$, respectively.

When $d_k \approx R$, the outer layers of the core are optically thick to neutrinos and the transport problem approaches that of an optically thick planar system, specifically that of a half-space. The dominant opacity source in the outer core before the passage of the bounce shock is the conservative scattering of neutrinos on nuclei for which

$$\frac{d\sigma}{d \cos \theta} = 1 + \cos \theta \quad (\text{B32})$$

at the low neutrino energies of relevance here (Tubbs and Schramm 1975, and Appendix C below), where θ is the angle between the directions of the incident and scattered neutrino. (At higher energies [≥ 25 MeV] the coherent scattering of neutrinos on nuclei becomes more forward-peaked because of the form factor of the composite target.) After the passage of the bounce shock the nuclei are dissociated by the high postshock temperature, and the dominant opacity sources become absorption on neutrons and protons for electron-type neutrinos and antineutrinos, respectively, and neutrino-nucleon scattering for all the thermal neutrinos. The former process is only very mildly anisotropic, owing to enhanced neutrino blocking for emission in the streaming direction. The latter processes are, to good approximation, of the form

$$\frac{d\sigma}{d \cos \theta} \propto 1 + \alpha \cos \theta, \quad (\text{B33})$$

where α is about -0.13 for neutrino-proton scattering, and about -0.033 for neutrino-neutron scattering (see Appendix C). These scattering processes are thus almost isotropic as well. The coefficient 0.5774 in equation (B26) was chosen so that in the limit $d_k = R$ (opaque outer core) the value of K_k becomes appropriate for an isotropic, conservative, plane-parallel, scattering atmosphere (Chandrasekhar 1960) and the radiative equilibrium, plane-parallel, gray atmosphere (Mihalas 1970). While this limit does not correspond exactly to the neutrino transport conditions in the outer core either before or after shock propagation, it is a fair approximation. Furthermore, this limit is never closely approached in an actual calculation.

The other limiting case is more important and occurs when d_k approaches zero. In this limit the neutrinos propagate without interaction from the deep interior. By the time they reach the outer boundary their propagation directions are confined to a narrow cone centered about the surface normal. If these neutrinos originated from an opaque, isotropically emitting surface of radius d_k , then

$$\psi_{N_M, k}^{(0)} = \frac{2}{3} \frac{1}{1 + \cos \theta_L} \psi_{N_M, k}^{(1)} \quad (\text{B34})$$

This is the limit approached in equation (B29) when d_k approaches zero.

IV. STABILITY PROBLEMS

The numerical scheme described in this appendix developed stability problems that were traced to the explicit numerical solution for $\psi^{(1)}$ obtained from equation (A25). Recall that the numerical solution for $\psi^{(1)}$ was obtained from equation (A25) only after the solutions for $\psi^{(0)}$, T , and Y_e were obtained from equations (A27), (B11), and (B12). This meant that quantities on the right-hand side of equations (A25) and (A27) depending on $\psi^{(1)}$, e.g., the quantities given in equations (A35), (A37), (A39), (A41), (A42), (A44), and (A46), had to be evaluated using the values of the $\psi_{j,k}^{(1)}$ at the beginning of the time step.

It was found that this stability problem could be eliminated by setting to zero the first Legendre coefficients associated with neutrino-electron scattering and neutrino thermal production except in the outer part of the core for which $\tau_k \leq 1$, where τ_k is the neutrino optical depth measured inward from the surface for energy zone k . The region $\tau_k \leq 1$ in the outer core is where the first Legendre moments are most important, since the ratio of $\psi^{(1)}$ to $\psi^{(0)}$ is largest there. However, setting the first Legendre coefficients to zero in the opaque region of the core is an unfortunate requirement, and a more sophisticated numerical scheme will be adopted for future investigations that will make this procedure unnecessary. One possibility would be to solve for $\psi^{(1)}$ implicitly together with $\psi^{(0)}$, T , and Y_e . This would certainly work, but it would almost double the size of the matrices that would have to be inverted during the course of the solution. Another possibility is to alternate the solution of $\psi^{(0)}$ and $\psi^{(1)}$. (An analogous approach was used by Falk and Arnett 1977 in a different context, although their energy zones were not coupled.) Either scheme would have the additional advantage that it would then be possible to retain the time derivative of $\psi^{(1)}$ (cf. eq. [A11]).

APPENDIX C

DERIVATIONS OF THE WEAK INTERACTION RATES

In this appendix brief derivations are given of the zeroth and first moments of the neutrino-matter interaction rates used in the core-collapse calculations. These moments are tied to the neutrino evolution equations through equations (A5), (A6), (A33), (A8), (A40), (A9), and (A42). The “standard theory” of electroweak interactions as proposed by Weinberg (1967, 1972) and Salam (1969) is used in the calculation of these rates. (Recent reviews of the standard theory are given by Bilenki 1982 and Quigg 1983.) Expressions for most of the rates derived here have been given elsewhere (Tubbs and Schramm 1975; Yueh and Buchler 1976b, 1977; Lamb and Pethick 1976; Bludman and Van Riper 1978). There are a number of reasons for including a discussion of the rates here: (1) there are some differences (minor differences in most cases) in the rates used here and those found in the above references; (2) moments of the rates are needed here, and, with the exception of Yueh and Buchler (1977), these are not found in the above references; and (3) the rates for the pair annihilation process have not been given at all in the literature in a form which is suitable for a multienergy zone calculation. The first section contains some general expressions for the rates. This is followed by specific discussions of neutrino absorption on nucleons in § II, neutrino absorption on nuclei in § III, neutrino-nucleon scattering in § IV, coherent neutrino scattering on nuclei in § V, neutrino-electron scattering in § VI, and the pair annihilation process in § VII.

I. SOME GENERAL EXPRESSIONS

To avoid a plethora of \hbar 's and c 's, “natural” units will be used (i.e., $\hbar = 1$, $c = 1$), with the exception that the final moments will be given in cgs units. The notation used here will follow the conventions of Bjorken and Drell (1964, 1965). Following Shalitin (1978), let

$$r = r(p_i + p_j \rightarrow p'_k + p'_l) \quad (\text{C1})$$

denote the final spin-summed, initial spin-averaged reaction rate between particles in definite translational states, i.e.,

$$rdn(\hat{p}_i)dn(\hat{p}_j)\left[d^3p'_k/(2\pi)^3\right]\left[d^3p'_l/(2\pi)^3\right]$$

is the reaction rate per unit volume between $dn(\hat{p}_i)$ and $dn(\hat{p}_j)$ particles of types i and j , respectively, in which the products (particles of types k and l) are found in the momentum-space elements $d^3p'_k$ and $d^3p'_l$. The 4-momentum of a neutrino will be denoted by $q = (\bar{q}, \omega)$, and that of a particle (other than a neutrino) of type i by $p_i = (\bar{p}_i, E_i)$. The occupation probability of the neutrino will be denoted, as before, by $f(\mu, \omega)$, and that of particles of type i by $F_i(E_i)$; the latter is assumed to be Fermi-Dirac, i.e.,

$$F_i(E_i) = 1/[1 + \exp \beta(E_i - \mu_i)], \quad (C2)$$

where μ_i is the chemical potential including rest mass of the type i particles (μ_i^0 will denote the corresponding chemical potential without the rest mass included), and $\beta = 1/kT$. Hereafter, $i = e, e^+, p, n, N, A$ refer, respectively to electrons, positrons, protons, neutrons, nucleons, and nuclei. The matter (everything but the neutrinos) is assumed to be in nuclear statistical equilibrium. The quantities n_i and M_i will refer to the number density and mass of particle i , respectively.

The reaction rate, $r(p_i + p_j \rightarrow p'_k + p'_l)$ is related to the reaction rate for the inverse process, $r(p'_k + p'_l \rightarrow p_i + p_j)$, by the reciprocity relation

$$(2s_i + 1)(2s_j + 1)r(p_i + p_j \rightarrow p'_k + p'_l) = (2s_k + 1)(2s_l + 1)r(p'_k + p'_l \rightarrow p_i + p_j), \quad (C3)$$

where s_i is the spin of particle i , etc. ($s = 0$ for neutrinos). In terms of the reaction rate r , the emissivity $j(\omega)$ and absorptivity $1/\lambda^{(a)}(\omega)$ given in equation (A5), and the scattering and thermal production and absorption kernels given in equations (A6), (A8), and (A9), are given by

$$\left\{\begin{array}{l} j(\omega) \\ 1/\lambda^{(a)}(\omega) \end{array}\right\} = \int \frac{d^3p_p}{(2\pi)^3} \int \frac{d^3p_n}{(2\pi)^3} \int \frac{d^3p_e}{(2\pi)^3} \left\{ \begin{array}{l} 2F_p(E_p)[1 - F_n(E_n)]2F_e(E_e)r(p_p + p_e \rightarrow p_n + q) \\ [1 - F_p(E_p)][1 - F_e(E_e)]r(p_n + q \rightarrow p_p + p_e) \end{array} \right\}, \quad (C4)$$

$$R_{\text{NES,IS}}^{\text{in}} = \int \frac{d^3p_t}{(2\pi)^3} \int \frac{d^3p'_t}{(2\pi)^3} \left\{ \begin{array}{l} [1 - F_t(E_t)]2F_t(E'_t)r(p'_t + q' \rightarrow p_t + q) \\ 2F_t(E_t)[1 - F_t(E'_t)]r(p_t + q \rightarrow p'_t + q') \end{array} \right\}, \quad (C5)$$

$$R_{\text{TP}}^{\text{p}} = \int \frac{d^3p_e}{(2\pi)^3} \int \frac{d^3p'_e}{(2\pi)^3} \left\{ \begin{array}{l} 2F_e(E_e)2F_{e^+}(E_{e^+})r(p_e + p_{e^+} \rightarrow q + q') \\ [1 - F_e(E_e)][1 - F_{e^+}(E_{e^+})](q + q' \rightarrow p_e + p_{e^+}) \end{array} \right\}, \quad (C6)$$

where p_t and p'_t refer to the momenta of the target particle and q and q' are the in and out beam neutrino momenta in equation (C5), and where q and q' are the momenta of the neutrino and antineutrino in equation (C6). The following relations follow from equations (C3)–(C6):

$$1/\lambda^{(a)}(\omega) = \exp \{ \beta[\omega - (\mu_p + \mu_e - \mu_n)] \} j(\omega) \quad (\text{electron-type neutrino}), \quad (C7)$$

$$\begin{aligned} 1/\lambda^{(a)}(\omega) &= \exp \{ \beta[\omega - (\mu_n - \mu_p + \mu_{e^+})] \} j(\omega) \\ &= \exp \{ \beta[\omega - (\mu_n - \mu_p - \mu_e)] \} j(\omega) \quad (\text{electron-type antineutrinos}), \end{aligned} \quad (C8)$$

$$R_{\text{NES,IS}}^{\text{in}}(\omega, \omega', \cos \theta) = \exp [\beta(E_t - E'_t)] R_{\text{NES,IS}}^{\text{out}}(\omega, \omega', \cos \theta) \quad (\text{all neutrino types}), \quad (C9)$$

and

$$R_{\text{TP}}^a(\omega, \omega', \cos \theta) = \exp [\beta(E_e + E_{e^+})] R_{\text{TP}}^p(\omega, \omega', \cos \theta) \quad (\text{all neutrino-type pairs}). \quad (C10)$$

II. NEUTRINO ABSORPTION ON NUCLEONS

a) $\nu_e + n \rightleftharpoons c + p$ (Electron-Type Neutrino Absorption on Neutrons)

The matrix element for this process is given by

$$M = \frac{G}{\sqrt{2}} \bar{u}_p(p_p) \gamma^\mu (g_V - g_A \gamma_5) u_n(p_n) \bar{u}_e(p_e) \gamma_\mu (1 - \gamma_5) u_\nu(q), \quad (C11)$$

where the virtual strong interaction processes enter the nucleon charged current as form factors which, in the zero momentum transfer limit, are the constants $g_V = 1$ and $g_A = 1.23$. (This well-known fact is mentioned now to serve a discussion below of the nucleon neutral current.) From equation (C11) the transition rate, $r(q + p_n \rightarrow p_e + p_p)$, is given by

$$r = \frac{G^2}{\omega E_e E_p E_n} (2\pi)^4 \delta^4(q + p_n - p_e - p_p) \left[(g_V + g_A)^2 p_p \cdot p_e p_n \cdot q + (g_V - g_A)^2 p_p \cdot q p_n \cdot p_e - (g_V^2 - g_A^2) M_n M_p p_e \cdot q \right]. \quad (\text{C12})$$

Yueh and Buchler (1976b) have reduced equation (C4) to a double integral taking into account the thermal distribution and recoil of the nucleons. An analytic approximation of equation (C4) was obtained by Tubbs and Schramm (1975) by taking $F_p(E_p) = 0$, $F_n(E_n) = n_n \delta^3(\bar{p}_n)$, and the low-energy restriction $\omega \ll M_n$. An alternative analytic approximation is derived here by replacing the delta function in equation (C12) by $\delta^3(\bar{p}_n - \bar{p}_p) \delta(\omega + E_n - E_e - E_p)$, i.e., by ignoring the momentum transferred to the nucleon. Performing the integrations in equations (C4) with the assumption that $|\bar{p}_n| \ll M_n$ and $|\bar{p}_p| \ll M_p$ gives the result

$$1/\lambda^{(a)}(\omega) = \frac{G^2}{\pi} \eta_{np} (g_V^2 + 3g_A^2) [1 - F_e(\omega + Q)] (\omega + Q)^2 \left[1 - \frac{M_e^2}{(\omega + Q)^2} \right]^{1/2}, \quad (\text{C13})$$

where $Q = M_n - M_p = 1.2935$ MeV, and

$$\begin{aligned} \eta_{np} &= \int \frac{2 d^3 p}{(2\pi)^3} F_n(E) [1 - F_p(E)] \\ &= \int \frac{2 d^3 p}{(2\pi)^3} \frac{\exp[\beta(E - \mu_n^0)] - \exp[\beta(E - \mu_p^0)]}{\exp[\beta(\mu_p^0 - \mu_n^0)] - 1} F_n(E) F_p(E) \\ &= \frac{1}{\exp[\beta(\mu_p^0 - \mu_n^0)] - 1} \int \frac{2 d^3 p}{(2\pi)^3} [F_p(E) - F_n(E)] \\ &= (n_p - n_n) / (\exp[\beta(\mu_p^0 - \mu_n^0)] - 1), \end{aligned} \quad (\text{C14})$$

where we have taken $E = p^2/2M$ ($M \approx M_n \approx M_p$). The quantity η_{np} takes into account the nucleon final state blocking and is equal to n_n in the nondegenerate regime (where blocking is not important), but becomes smaller than n_n when the nucleons become degenerate. Graphs of η_{np}/n_n and η_{pn}/n_p , where the latter is defined by the replacement $n \leftrightarrow p$ in equation (C14), as a function of density for different material entropies are given in Figure 34. Equation (C13) for $1/\lambda^{(a)}$ differs from the equivalent expression in Tubbs and Schramm (1975) by the replacement $\eta_{np} \rightarrow n_n$ in the latter. This difference does not have a large effect on the results of collapse calculations because it becomes significant only when the free nucleons (free protons, in this case) become degenerate. Free nucleon degeneracy occurs only at very high densities, particularly above nuclear densities where nuclei no longer bind up an appreciable fraction of the nucleons, and at these high densities neutrinos are trapped and very accurate values for the rates are not important.

An application of (C8) to equation (C13) gives

$$j(\omega) = \frac{G^2}{\pi} \eta_{pn} (g_V^2 + 3g_A^2) F_e(\omega + Q) (\omega + Q)^2 \left[1 - \frac{M_e^2}{(\omega + Q)^2} \right]^{1/2}. \quad (\text{C15})$$

The factor G^2 in expressions (C13) and (C15) is the Fermi constant [$G = (1.015 \pm 0.03) \times 10^5 M_p^{-2}$] with the value

$$G^2 = \left[\frac{1}{(\hbar c)^4} \right] G^2 = 5.18 \times 10^{-44} \text{ MeV}^{-2} \text{ cm}^2, \quad (\text{C16})$$

giving $1/\lambda^{(a)}(\omega)$ and $j(\omega)$ the required units of cm^{-1} .

b) $\bar{\nu}_e + p \xrightarrow{} e^+ + n$ (Electron-Type Antineutrino Absorption on Protons)

The matrix element for this process is given by

$$M = \frac{G}{\sqrt{2}} \bar{u}_n(p_n) \gamma^\mu (g_V - g_A \gamma_5) u_p(p_p) \bar{\nu}_e(p_{e^+}) \gamma_\mu (1 - \gamma_5) v_\nu(q), \quad (\text{C17})$$

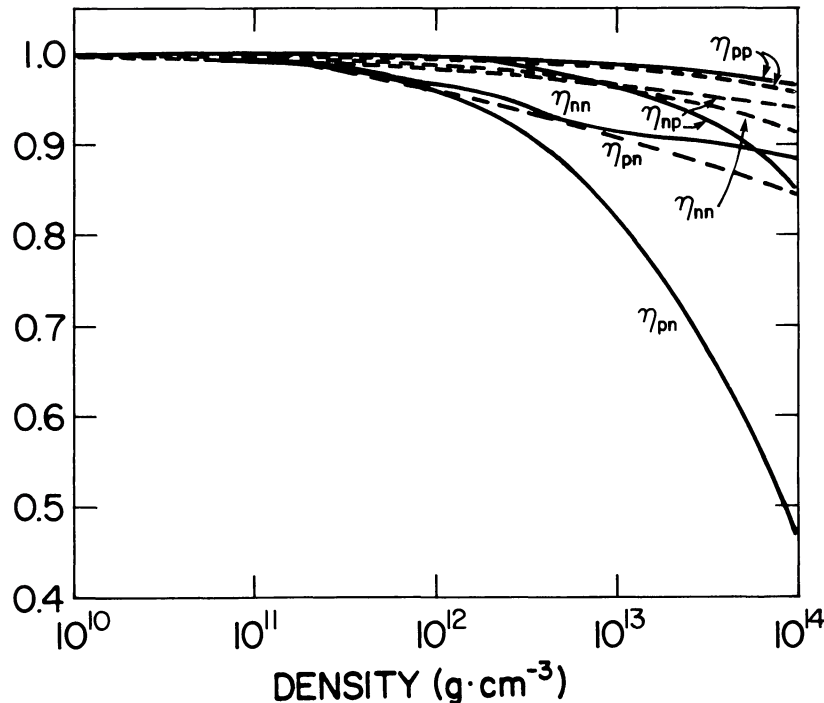


FIG. 34.—The nucleon final-state inhibition factors η_{nn} , η_{np} , η_{pn} , and η_{pp} as a function of density for matter entropies equal to 1.5 (solid lines) and 8 (dashed lines).

which gives rise to the transition rate, $r(q + p_p \rightarrow p_{e^+} + p_n)$,

$$r = \frac{G^2}{\omega E_{e^+} E_p E_n} (2\pi)^4 \delta^4(q + p_p - p_{e^+} - p_n) \left[(g_V + g_A)^2 p_p \cdot q p_n \cdot p_{e^+} + (g_V - g_A)^2 p_n \cdot q p_p \cdot p_{e^+} - (g_V^2 - g_A^2) M_n M_p p_{e^+} \cdot q \right]. \quad (\text{C18})$$

Proceeding as above results in

$$1/\lambda^{(a)}(\omega) = \frac{G^2}{\pi} \eta_{pn} (g_V^2 + 3g_A^2) [1 - F_{e^+}(\omega - Q)] (\omega - Q)^2 \left[1 - \frac{M_e^2}{(\omega - Q)^2} \right] \Theta(\omega - Q - M_e) \quad (\text{C19})$$

and

$$j(\omega) = \frac{G^2}{\pi} \eta_{np} [g_V^2 + 3g_A^2] F_{e^+}(\omega - Q) (\omega - Q)^2 \left[1 - \frac{M_e^2}{(\omega - Q)^2} \right] \Theta(\omega - Q - M_e), \quad (\text{C20})$$

where the threshold of $\omega = Q + M_e$ for the antineutrino absorption and emission by free nucleons is incorporated in the Θ -function [$\Theta(x) = 0$, $x < 0$; $\Theta(x) = 1$, $x > 0$].

III. $\nu_e + A' \leftrightarrows A + e$ (NEUTRINO ABSORPTION ON NUCLEI)

The details of this process are still obscure because the nuclei involved are far from the valley of β -stability and little is known about their detailed structure. Consider first the inverse process, electron capture on nuclei. The matrix element is

$$M = \frac{G}{\sqrt{2}} J^\mu \bar{u}_v(q) \gamma_\mu (1 - \gamma_5) u_e(p_e), \quad (\text{C21})$$

where $J^\mu = \langle A' | \hat{J}^\mu(0) | A \rangle$ [$A = (N, Z)$, $A' = (N+1, Z-1)$], and where the current operator has been transformed to the origin (nuclear center of mass) by the translational invariance property, $\hat{J}^\mu(x) = e^{-i\hat{p} \cdot x} \hat{J}^\mu(0) e^{i\hat{p} \cdot x}$, where \hat{p} is the total 4-momentum

operator. The transition rate $r(p_e + p_A \rightarrow q + p_{A'})$ is found to be

$$\begin{aligned} r &= \frac{G^2}{2\omega E_e} (2\pi)^4 \delta(p_e + p_A - q - p_{A'}) \frac{1}{2J_A + 1} \sum_{m_A} \sum_{m_{A'}} J^\mu J^{*\alpha} [q_\mu(p_e)_\alpha + q_\alpha(p_e)_\mu - q \cdot p_e g_{\mu\alpha} - i\epsilon_{\beta\mu\delta\alpha} q^\beta p_e^\delta] \\ &= \frac{G^2}{2} (2\pi)^4 \delta(p_e + p_A - q - p_{A'}) \frac{1}{2J_A + 1} \sum_{m_A} \sum_{m_{A'}} \left[|J^0|^2 (1 + \bar{v}_e \cdot \hat{q}) + |\bar{J}|^2 \left(1 - \frac{1}{3} \bar{v}_e \cdot \hat{q}\right) \right], \end{aligned} \quad (\text{C22})$$

where $\epsilon_{\alpha\beta\gamma\delta}$ is a completely antisymmetric tensor with $\epsilon_{0123} = 1$, where $\bar{v}_e = \bar{p}_e/E_e$, $\hat{q} = \bar{q}/\omega$, and where some of the missing steps can be found in Eder (1968) and Konopinski (1966). Neglecting Coulomb correction in the electron wave functions and using the zero-momentum transfer form factor limits, the nuclear current can be expressed as

$$\begin{aligned} \langle A' | \hat{J}^\mu(0) | A \rangle &= \langle A' | \sum_{j=1}^A \gamma^{0(j)} \gamma^{\mu(j)} (g_V - g_A \gamma_5^{(j)}) \tau_-^{(j)} \exp[i(\bar{q} - \bar{p}_e) \cdot \bar{r}(j)] | A \rangle, \\ &\xrightarrow{\text{allowed}} \begin{cases} \langle A' | \sum_{j=1}^A g_v \tau_-^{(j)} | A \rangle, & \mu = 0 \\ -\langle A' | \sum_{j=1}^A g_A \sigma^{\mu(j)} \tau_-^{(j)} | A \rangle, & \mu = 1, 2, 3, \end{cases} \end{aligned} \quad (\text{C23})$$

where τ_- is the isospin lowering operator, and σ^μ ($\mu = 1, 2, 3$) is the μ th Pauli spin operator, and where the usual approximations [$(\bar{q} - \bar{p}_e) \cdot \bar{r}^{(j)} \ll 1$, nonrelativistic description of nuclear constituents] for allowed transitions have been made to obtain the final expressions.

To proceed, observe that nuclei in the collapsing core, being neutron-rich, have ground states corresponding to the lowest isospin component in the multiplet (i.e., $T_3 = -T$). Electron capture from the ground state must therefore increase the total nuclear isospin quantum number (Fuller 1982). Other transitions must take place through a thermal population of excited states. Only the Gamow-Teller (GT) operator ($\sigma^\mu \tau_-$) connects states of different isospin, in the allowed approximation, so only $|\bar{J}|^2$ is nonzero in equation (C22) for allowed electron capture reactions through the parent ground state. These electron capture reactions are dominated by the $1f_{7/2} \rightarrow 1f_{5/2}$ GT resonance, as pointed out by Bethe *et al.* (1979), unless this reaction is blocked by the absence of appropriate neutron holes, which occurs when $N \geq 40$ ($N \geq 38$ if the $p_{1/2}$ shell lies above the $f_{5/2}$ shell) (Fuller 1982; see also Van Riper and Lattimer 1981). Fuller, Fowler, and Newman (1982) have estimated the nuclear spin sums for this transition as

$$\frac{1}{2J_A + 1} \sum_{m_A} \sum_{m_{A'}} |\bar{J}|^2 = \frac{N_p N_h}{2J_{A'} + 1} \frac{12}{7} = \frac{2}{7} N_p N_h, \quad (\text{C24})$$

where N_p is the number of protons in the single-particle $1f_{7/2}$ level and N_h is the number of neutron holes in the single-particle $1f_{5/2}$ level. As a crude estimate of N_p and N_h , a zero-order shell model predicts that

$$N_p(Z) = \begin{cases} 0, & Z < 20 \\ Z - 20, & 20 < Z < 28 \\ 8, & Z > 28, \end{cases} \quad (\text{C25})$$

$$N_h(N) = \begin{cases} 6, & N < 34 \\ 40 - N, & 34 < N < 40 \\ 0, & N > 40. \end{cases} \quad (\text{C26})$$

Using equations (C24)–(C26) in equation (C22), the result in equation (C4), and proceeding as in the case of neutrino absorption on neutrons, we obtain

$$j(\omega) = \frac{G^2}{\pi} n_A g_A^2 \frac{2}{7} N_p(Z) N_h(N) F_e(\omega + Q') (\omega + Q')^2 \left[1 - \frac{M_e^2}{(\omega + Q')^2} \right]^{1/2}, \quad (\text{C27})$$

where

$$Q' = M_{A'}^* - M_A = M_{A'} - M_A + \Delta \approx \mu_n - \mu_p + \Delta, \quad (\text{C28})$$

the latter expression holding if A is the mean nucleus (e.g., Fuller 1982, eq. [26]). The quantity $\Delta = M_A^* - M_{A'}$ is the energy of the neutron $1f_{5/2}$ state above the ground state; its value has been estimated to be about 3 MeV (Bethe *et al.* 1979; Fuller, Fowler, and Newman 1982), and its value is assumed to be 3 MeV for all nuclei in the work. The numerical value of G^2 is again given by equation (C16) so that $j(\omega)$ will have the required units of cm^{-1} . Expression (C27) is similar to, though not identical with, to electron capture rates given by Epstein and Pethick (1981), Van Riper and Lattimer (1981), Bludman, Lichtenstadt, and Hayden (1982), and Bowers and Wilson (1982a), although only the latter is expressed in a form suitable for a multienergy neutrino calculation.

The inverse mean free path, $1/\lambda^{(a)}(\omega)$, corresponding to the inverse reaction, $\nu + A' \rightarrow e + A$, can be obtained from equation (C27) by an application of equation (C7). The result is

$$1/\lambda^{(a)}(\omega) = \frac{G^2}{\pi} n_A \exp [\beta(\mu_n - \mu_p - Q')] g_A^2 \frac{2}{7} N_p(Z) N_n(N) [1 - F_e(\omega + Q')] (\omega + Q')^2 \left[1 - \frac{M_e^2}{(\omega + Q')^2} \right]^{1/2}. \quad (\text{C29})$$

As one would expect, the product in equation (29) of n_A and the exponential factor is just the number density of GT resonance-excited A' nuclei.

Bowers and Wilson (1982a), in their numerical treatment of electron capture on nuclei, modify the threshold energy for capture by a temperature-dependent factor to take into account the possibility of thermal re-excitation accompanying thermal de-excitation at high temperatures. In the numerical treatment employed here, where a given quantity of energy resides in either one of the neutrino fields or in the matter, such a factor is unnecessary. The matter is assumed to be in nuclear statistical equilibrium and therefore to equilibrate instantaneously to changes in energy or lepton number. The energy of the neutrino resulting from an electron capture is $E_e - Q'$ regardless of how the matter equilibrates after the capture.

IV. $\nu + N \rightleftharpoons \nu + N$ (NEUTRINO-NUCLEON SCATTERING)

Neutrino-nucleon scattering proceeds by the exchange of the neutral Z boson only. Different neutrino or antineutrino types will not be distinguished in this or the next section, since the reaction rate is the same for all types. The matrix element is given by

$$M = \frac{G}{\sqrt{2}} [\bar{u}_N(p'_N) \gamma^\mu (h_V^N - h_A^N \gamma_5) u_N(p_N)] [\bar{u}_\nu(q') \gamma_\mu (1 - \gamma_5) u_\nu(q)], \quad (\text{C30})$$

where N refers to a proton ($N = p$) or a neutron ($N = n$). The quantities h_V^N and h_A^N are the neutral nucleon current form factors in the limit of zero-momentum transfer, and arise, as in the nucleon charged currents, by virtual strong interaction processes. (The electromagnetic current also makes a contribution to the proton neutral current.) In the standard theory (e.g., Bilenki 1982)

$$h_V^p = \frac{1}{2} - 2 \sin^2 \theta_W, \quad (\text{C31})$$

$$h_A^p = \frac{1}{2} g_A, \quad (\text{C32})$$

$$h_V^n = -\frac{1}{2}, \quad (\text{C33})$$

$$h_A^n = -\frac{1}{2} g_A, \quad (\text{C34})$$

Matrix element (C30) differs from that used in prior derivations of the scattering rate in that the prior derivations have taken $h_A^n = -\frac{1}{2}$. Using equation (C30) the reaction rate $r(q + p_N \rightarrow q' + p'_N)$ is found to be

$$r = \frac{G^2}{\omega \omega' E_N E'_N} (2\pi)^4 \delta^4(q + p_N - q' - p'_N) \left\{ (h_V^N + h_A^N)^2 p_N \cdot q p'_N \cdot q' + (h_V^N - h_A^N)^2 p'_N \cdot q p_N \cdot q' - [(h_V^N)^2 - (h_A^N)^2] M_N^2 q \cdot q' \right\}. \quad (\text{C35})$$

Making the isoenergetic, zero-momentum transfer approximation [$\delta^4(q + p_N - q' - p'_N) \rightarrow \delta(\omega - \omega') \delta(\bar{p}_N - \bar{p}'_N)$], and assuming that $|\bar{p}_N|^2/E_N^2 \ll 1$, equations (C5) and (C35) give

$$R_{IS,N}^{\{in\}} = R_{IS,N} = 2\pi G^2 \eta_{NN} \left\{ (h_V^N)^2 + 3(h_A^N)^2 + [(h_V^N)^2 - (h_A^N)^2] \cos \theta \right\} \delta(\omega - \omega'), \quad (\text{C36})$$

where $\theta = \hat{\mathbf{q}} \cdot \hat{\mathbf{q}'} \text{ and}$

$$\begin{aligned}\eta_{NN} &= \int \frac{2 d^3 p_N}{(2\pi)^3} F_N(E_N) [1 - F_N(E_N)] \\ &= \int \frac{2 d^3 p_N}{(2\pi)^3} \frac{\exp [\beta(E_N - \mu_N)]}{[1 + \exp [\beta(E_N - \mu_N)]]^2} \\ &= \frac{1}{\beta} \frac{\partial n_N}{\partial \mu_N} \\ &\rightarrow \begin{cases} n_N, & \text{nondegenerate } N \\ \frac{3}{2} n_N / (\beta \mu_N), & \text{degenerate } N. \end{cases} \end{aligned} \quad (C37)$$

Graphs of η_{nn} and η_{pp} versus density for various material entropies are shown in Figure 34. As with the factors η_{np} and η_{pn} introduced in the neutrino-nucleon absorption and emission rates, η_{NN} is equal to n_N when the nucleons N are nondegenerate, but decreases due to final state blocking when the nucleons become degenerate.

The zeroth and first Legendre coefficients of $R_{IS,N}^0$, defined in equation (A40), where $R_{IS,N} = R_{IS,N}^0 \delta(\omega - \omega')$, are given by

$$\Phi_{0,IS}^N(\omega) = 4\pi G^2 \eta_{NN} [(h_V^N)^2 + 3(h_A^N)^2], \quad (C38)$$

$$\Phi_{1,IS}^N(\omega) = \frac{4\pi}{3} G^2 \eta_{NN} [(h_V^N)^2 - (h_A^N)^2]. \quad (C39)$$

The constant G^2 must take the value

$$G^2 = \left(\frac{1}{h}\right) G^2 = 1.2 \times 10^{-65} \text{ MeV cm}^3 \text{ s}^{-1}, \quad (C40)$$

so that the $\Phi_{l,IS}$ will have units of $\text{MeV cm}^3 \text{ s}^{-1}$, and B_{IS} (eq. [A8]) will have units of cm^{-1} . When account is taken of the minor differences in the definitions of the scattering kernels, the results given by equations (C38) and (C39) reduce to the corresponding expressions given by Yueh and Buchler (1977) if $\eta_{NN} \rightarrow n_N$ and $h_A^n = -g_A/2 \rightarrow -\frac{1}{2}$. The rates for neutrino-neutron scattering derived here are therefore substantially greater (about 40%), unless neutron degeneracy forces η_{nn} below n_n , than previously published rates.

V. $\nu + A \rightleftharpoons \nu + A$ (COHERENT SCATTERING OF NEUTRINOS ON NUCLEI)

An expression for the coherent neutrino-nuclei scattering transition rate, $r(q + p_A \rightarrow q' + p'_A)$, can be obtained from expression (C22) for the nuclear electron capture transition rate by making the lepton variable changes $p_e \rightarrow q$, $q \rightarrow q'$, multiplying by a factor of 2 because the spin-sum average is now over an incident neutrino instead of an electron, and replacing the charged nuclear current, J_z^μ , by the neutral nuclear current, J_z^μ . The result is

$$r = G^2 (2\pi)^4 \delta(q + p_A - q' - p'_A) \frac{1}{2J_A + 1} \sum_{m_A} \sum_{m'_A} \left[(J_z^0)^2 (1 + \hat{\mathbf{q}} \cdot \hat{\mathbf{q}'}) + |\bar{J}|^2 (1 - \frac{1}{3} \hat{\mathbf{q}} \cdot \hat{\mathbf{q}'}) \right]. \quad (C41)$$

The neutral current, J_z^μ , is given by

$$\begin{aligned} J_z^\mu &= \langle A | J_z^\mu(0) | A \rangle = \langle A | \sum_{j=1}^A \gamma^{\mu(j)} [h_V^{N(j)}(s^2) - h_A^{N(j)}(s^2) \gamma_5^{(j)}] \exp[i(\bar{\mathbf{q}}' - \bar{\mathbf{q}}) \cdot \bar{\mathbf{r}}^{(j)}] | A \rangle \\ &= \langle A | \sum_{j=1}^A \delta^{\mu(j)} [C_{\nu 0} + C_{\nu 1} \tau_3^{(j)} - \gamma_5^{(j)} (C_{A 0} + C_{A 1} \tau_3^{(j)})] | A \rangle \exp(-bs^2), \\ &\xrightarrow{\text{NR}} \begin{cases} \langle A | \sum_{j=1}^A (C_{\nu 0} + C_{\nu 1} \tau_3^{(j)}) | A \rangle \exp(-bs^2), & \mu = 0 \\ -\langle A | \sum_{j=1}^A (C_{A 0} + C_{A 1} \tau_3^{(j)}) \sigma^{\mu(j)} | A \rangle \exp(-bs^2), & \mu = 1, 2, 3, \end{cases} \end{aligned} \quad (C42)$$

where the current operator has been written as sums of isoscalar and isovector components, with $C_{x0} = \frac{1}{2}(h_x^p + h_x^n)$, $C_{x1} = (h_x^p - h_x^n)$, $x = V$ or A , and where the details of the nuclear wave function have been absorbed in the assumed Gaussian form factor with $b = \frac{1}{6}\langle r^2 \rangle \approx 4.8 \times 10^{-6} A^{2/3}$ MeV $^{-2}$ (Freedman 1974; Tubbs and Schramm 1975) and where $s^2 = 2q \cdot q' = 2\omega^2(1 - \cos \theta)$ ($\cos \theta = \hat{q} \cdot \hat{q}'$) is the invariant squared momentum transfer. The last expression in equation (C42) gives the nonrelativistic (NR) limit. For any nucleus (in the nonrelativistic limit) the Fermi part of the nuclear current is $J_z^0 = [AC_{V0} + \frac{1}{2}(N-Z)C_{V1}] \exp(-bs^2)$. The Gamow-Teller part is zero for spin zero nuclei and is expected to be small relative to the Fermi part for most other nuclei because $C_{A0} = 0$ in the standard theory. With the Fermi part of the nuclear current only in equation (C41), use of equation (C41) in equation (C5) gives

$$\begin{aligned} R_{IS,A}^{\{in\}_{out}} &= R_{IS,A} \\ &= 2\pi G^2 n_A A^2 \left(C_{V0} + \frac{1}{2} \frac{N-Z}{A} C_{V1} \right)^2 (1 - \cos \theta) \exp[-4b\omega^2(1 - \cos \theta)] \delta(\omega - \omega'), \end{aligned} \quad (C43)$$

where the isoenergetic zero-momentum transfer approximation has been made and the nuclei were assumed nondegenerate. The zero and first Legendre coefficients of $R_{IS,A}^{(0)}$ (eq. [A40]), where $R_{IS,A}^{(0)} \delta(\omega - \omega') = R_{IS,A}$, are given by

$$\Phi_{0,IS}^A(\omega) = 2\pi G^2 n_A A^2 \left(C_{V0} + \frac{1}{2} \frac{N-Z}{A} C_{V1} \right)^2 \frac{2y - 1 + e^{-2y}}{y^2}, \quad (C44)$$

$$\Phi_{1,IS}^A(\omega) = 2\pi G^2 n_A A^2 \left(C_{V0} + \frac{1}{2} \frac{N-Z}{A} C_{V1} \right)^2 \frac{2 - 3y + 2y^2 - (2+y)e^{-2y}}{y^3}, \quad (C45)$$

where $y = 4b\omega^2$. The constant G^2 is again given by equation (C40). Expressions (C44) and (C45) for $\Phi_{0,IS}^A$ and $\Phi_{1,IS}^A$ agree with the corresponding expressions in Yueh and Buchler (1977), allowance being made for minor differences in the definitions of some quantities, except that the y^3 in the denominator in expression (C45) is y^2 in Yueh and Buchler.

VI. $\nu + e \rightleftharpoons \nu + e$ (NEUTRINO-ELECTRON SCATTERING [NES])

First consider the NES of electron-type neutrinos. This proceeds by the exchange of both a charged boson, giving rise to the matrix element

$$M_w = \frac{G}{\sqrt{2}} [\bar{u}_\nu(q') \gamma^\mu (1 - \gamma_5) u_e(p_e)] [\bar{u}_e(p'_e) \gamma_\mu (1 - \gamma_5) u_\nu(q)], \quad (C46)$$

and a neutral boson, giving rise to the matrix element

$$M_z = \frac{G}{\sqrt{2}} [\bar{u}_\nu(q') \gamma^\mu (1 - \gamma_5) u_\nu(q)] [\bar{u}_e(p'_e) \gamma_\mu (a - b\gamma_5) u_e(p_e)], \quad (C47)$$

where $a = -\frac{1}{2} + 2 \sin^2 \theta_W$ and $b = -\frac{1}{2}$ according to the standard theory. First reordering equation (C46) (Marshak and Ryan 1969) and adding it to equation (C47) gives the total matrix element,

$$M = \frac{G}{\sqrt{2}} [\bar{u}_\nu(q') \gamma^\mu (1 - \gamma_5) u_\nu(q)] [\bar{u}_e(p'_e) \gamma_\mu (C_V - C_A \gamma_5) u_e(p_e)], \quad (C48)$$

where $C_V = a + 1 = \frac{1}{2} + 2 \sin^2 \theta_W$, $C_A = b + 1 = \frac{1}{2}$. The transition rate, $r(q + p_e \rightarrow q' + p'_e)$, is given by

$$r = \frac{G^2}{\omega \omega' E_e E'_e} (2\pi)^4 \delta^4(q + p_e - q' - p'_e) [(C_V + C_A)^2 p_e \cdot q p'_e \cdot q' + (C_V - C_A)^2 p'_e \cdot q p_e \cdot q' - M_e^2 (C_V^2 - C_A^2) q' \cdot q]. \quad (C49)$$

For relativistic electrons the last term in equation (C49) is expected to be much smaller than the first two and is neglected here. The expressions for $R_{NES}^{\{in\}_{out}}$ were obtained by using equation (C49) in equation (C5), assuming extremely relativistic electrons ($E_e = |\bar{p}_e|$), and integrating over \bar{p}' and then over \bar{p} as detailed in Yueh and Buchler (1976a, b). The first two Legendre

coefficients of $R_{\text{NES}}^{\{\text{in out}\}}$, as defined in equation (A33), were obtained as detailed in Yueh and Buchler (1976b, 1977) and are given by

$$\begin{aligned} \Phi_{l,\text{NES}}^{\{\text{in out}\}} = & \frac{G^2}{\pi\omega^2\omega'^2} \int dE_e F_e(E_e) [1 - F_e(E_e + \omega - \omega')] \left\{ \begin{array}{c} \exp[-\beta(\omega - \omega')] \\ 1 \end{array} \right\} \\ & \times [(C_V + C_A)^2 H_l^I(\omega, \omega', E_e) + (C_V - C_A)^2 H_l^{II}(\omega, \omega', E_e)], \end{aligned} \quad (\text{C50})$$

where the functions H_l^I and H_l^{II} for $l=0$ and $l=1$ are as given in Yueh and Buchler (1977), except that $E^4\omega$ and $E^3\omega^2$ in their equation (A5') should be $E^4\omega'$ and $E^3\omega'^2$, and $\omega\omega'^4$ in their equation for $b_1^I(\omega, \omega')$ should be $\omega\omega'^3$. The constant G^2 in equation (C50) has the value

$$G^2 = [c(\hbar c)^2] G^2 = 1.55 \times 10^{-33} \text{ cm}^3 \text{ MeV}^{-2} \text{ s}^{-1}, \quad (\text{C51})$$

which gives B_{NES} in equation (A6) the required units of cm^{-1} .

The NES of electron-type antineutrinos is a crossed channel (Berestetskii, Lifshitz, and Pitaevskii 1971) of the NES of electron-type neutrinos, and the matrix elements are related by the substitution $q \leftrightarrow -q'$. This is equivalent to replacing C_A by $-C_A$ in equation (C50). The NES of muon and tau neutrinos proceeds by the exchange of a neutral boson only (to conserve lepton numbers at each vertex), and the corresponding matrix element is given by expression (C47) alone. Thus C_V and C_A in equation (C50) should be replaced by $C_V - 1$ and $C_A - 1$, respectively, for this process. Finally, the NES of muon and tau antineutrinos is obtained by replacing C_V and C_A in equation (C50) by $C_V - 1$ and $C_A - 1$, respectively, and then changing the sign of $C_A - 1$.

VII. $e^- + e^+ \rightleftharpoons \nu + \bar{\nu}$ (NEUTRINO PRODUCTION FROM PAIR ANNIHILATION)

The cross section and energy loss rate for this process have been computed using the V - A theory by Chiu and Stabler (1961) and in the standard theory by Discus (1972). Since these results are not directly applicable to a multienergy treatment of neutrinos, a derivation of the production and absorption kernels and their zero and first Legendre coefficients is presented here.

Consider first the production of electron-type neutrino pairs. This reaction is the cross channel of NES, and the transition rate, $r(p_e + p_{e^+} \rightarrow q + q')$, can be obtained immediately from the transition rate (C49) for NES by the substitution $p'_e \rightarrow -p_{e^+}$, $q \rightarrow -q$, relabeling the final neutrino and antineutrino momenta by q and q' , respectively, and multiplying the resultant expression by $\frac{1}{2}$ because the initial spin-sum average is now over an electron and a positron rather than an electron and a neutrino. The result is

$$r = \frac{1}{2} \frac{G^2}{\omega\omega'E_eE_{e^+}} (2\pi)^4 \delta(q + q' - p_e - p_{e^+}) [(C_V + C_A)^2 p_{e^+} \cdot q p_e \cdot q' + (C_V - C_A)^2 p_e \cdot q p_{e^+} \cdot q' + M_e^2 (C_V^2 - C_A^2) q \cdot q']. \quad (\text{C52})$$

In the $C_V = C_A = 1$ limit (V - A theory), the expression reduces to the expression given and briefly discussed in Yueh and Buchler (1976b). For relativistic electrons the last term in equation (C61) is expected to be much smaller than the first two terms and will be neglected here. The production and absorption kernels are obtained from equations (C6), (C3) and (C52), and are given by

$$R_a^{\{p\}}(\omega, \omega', \cos\theta) = (C_V + C_A)^2 R_I^{\{p\}}(\omega, \omega', \cos\theta) + (C_V - C_A)^2 R_{II}^{\{p\}}(\omega, \omega', \cos\theta), \quad (\text{C53})$$

where

$$R_I^{\{p\}} = \frac{2G^2}{\omega\omega'E_eE_{e^+}} \frac{1}{(2\pi)^2} \int d^3p_e \left\{ \frac{F_e(E_e)}{1 - F_e(E_e)} \right\} \int d^3p_{e^+} \left\{ \frac{F_{e^+}(E_{e^+})}{1 - F_{e^+}(E_{e^+})} \right\} \delta^4(q + q' - p_e - p_{e^+}) p_e \cdot q' p_{e^+} \cdot q, \quad (\text{C54})$$

$$R_{II}^{\{p\}}(\omega, \omega', \cos\theta) = R_I^{\{p\}}(\omega', \omega, \cos\theta), \quad (\text{C55})$$

where $\cos\theta = \hat{q} \cdot \hat{q}'$. Assuming extremely relativistic electrons ($E_e = |\bar{p}_e|$) and positrons ($E_{e^+} = |p_{e^+}|$), and integrating over \bar{p}_{e^+} and then over \bar{p} , as described in Yueh and Buchler (1976a, b) for NES, we obtain, after much algebra,

$$R_I^{\{p\}} = \int_0^{\omega + \omega'} dE_e \left\{ \frac{F_e(E_e) F_{e^+}(\omega + \omega' - E_e)}{[1 - F_e(E_e)][1 - F_{e^+}(\omega + \omega' - E_e)]} \right\} \frac{2G^2}{2\pi} \frac{1}{\omega\omega'} (A + BE_e + CE_e^2) \Theta(D), \quad (\text{C56})$$

where

$$A = \omega'^2 y [(\omega' + \omega \cos \theta)^2 - \frac{1}{2} \omega^2 \sin^2 \theta], \quad (C57)$$

$$B = \omega' y [-2\omega'^2 + \omega^2 + 3\omega'\omega - \omega'\omega \cos \theta + 3\omega^2 \cos \theta], \quad (C58)$$

$$C = y [\omega'^2 + \omega^2 - 3\omega'\omega - \omega'\omega \cos \theta], \quad (C59)$$

$$y = \frac{\omega'^2 \omega^2 (1 - \cos \theta)^2}{[\omega'^2 + \omega^2 + 2\omega\omega' \cos \theta]^{5/2}}, \quad (C60)$$

$$D = 4E_e^2 \omega^2 \sin \theta^2 \omega \omega' (1 - \cos \theta) [-2E_e^2 + 2E_e(\omega + \omega') - \omega \omega' (1 - \cos \theta)]. \quad (C61)$$

The Θ -function arises from the requirement that $|\cos \beta| \leq 1$ in the argument of the energy-conserving δ -function, where β is the angle of \bar{p}_e to the plane defined by \bar{q} and \bar{q}' .

The Legendre coefficients of the production and absorption kernels (eq. [C56]) are defined in equation (A42) and are given by

$$\Phi_{l,\text{TP}}^{\left\{ \begin{matrix} p \\ a \end{matrix} \right\}} = \int_{-1}^1 R_{\text{TP}}^{\left\{ \begin{matrix} p \\ a \end{matrix} \right\}} P_l(\mu) d\mu = \frac{2G^2}{2\pi} \int_0^{\omega + \omega'} dE_e \left\{ \frac{F_e(E_e) F_{e+}(\omega + \omega' - E_e)}{[1 - F_e(E_e)][1 - F_{e+}(\omega + \omega' - E_e)]} \right\} \Phi_l(\omega, \omega', E_e), \quad (C62)$$

where $\mu = \cos \theta$, and where

$$\Phi_l(\omega, \omega', E_e) = (C_V + C_A)^2 J_l^I(\omega, \omega', E_e) + (C_V - C_A)^2 J_l^{\text{II}}(\omega, \omega', E_e), \quad (C63)$$

$$J_l^{\text{II}}(\omega, \omega', E_e) = J_l^I(\omega', \omega, E_e), \quad (C64)$$

$$\begin{aligned} J_l^I(\omega, \omega', E_e) &= \frac{1}{\omega \omega'} \Theta(\omega + \omega' - E_e) \int_{-1}^1 (A + BE_e + CE_e^2) P_l(\mu) d\mu \Theta(D) \\ &= \frac{1}{\omega \omega'} \Theta(\omega + \omega' - E_e) \left[\Theta(\omega - E_e) \int_{\mu_0}^1 f(E_e, \mu) d\mu + \Theta(E_e - \omega) \Theta(\omega' - E_e) \int_{-1}^1 f(E_e, \mu) d\mu \right. \\ &\quad \left. + \Theta(E_e - \omega') \int_{\mu_0}^1 f(E_e, \mu) d\mu \right] \quad (\omega < \omega'), \end{aligned} \quad (C65)$$

where $f(E_e, \mu) = (A + BE_e + CE_e^2) P_l(\mu)$ and $\mu_0 = 1 - 2E_e(\omega + \omega' - E_e)/\omega\omega'$. The expression for J_l^I when $\omega > \omega'$ is obtained from equation (C65) by the substitutions $\omega \leftrightarrow \omega'$ in the Θ -functions. With the substitution $x^2 = \omega^2 + \omega'^2 + 2\omega\omega'\mu$ (cf. Yueh and Buchler 1976b, Appendix A) the integrations can be performed, and after tremendous cancellation of terms the result for J_0^I is

$$\begin{aligned} J_0^I(\omega, \omega', E_e) &= \frac{1}{\omega \omega'} \Theta(\omega + \omega' - E_e) \{ [\Theta(\omega - E_e) \Theta(\omega' - \omega) + \Theta(\omega' - E_e) \Theta(\omega - \omega')] a_0(\omega, \omega', E_e) \\ &\quad + [\Theta(E - \omega) \Theta(\omega - \omega') + \Theta(E - \omega') \Theta(\omega' - \omega)] \\ &\quad \times b_0(\omega, \omega', E_e) + \Theta(E_e - \omega) \Theta(\omega' - E_e) c_0(\omega, \omega', E_e) \\ &\quad + \Theta(E_e - \omega') \Theta(\omega - E_e) d_0(\omega, \omega', E_e) \}, \end{aligned} \quad (C66)$$

where

$$a_0(\omega, \omega', E_e) = \frac{1}{\omega \omega'} \left[\frac{4}{15} E_e^5 - \frac{4}{3} E_e^4 \omega' + \frac{8}{3} E_e^3 \omega'^2 \right], \quad (C67)$$

$$\begin{aligned} b_0(\omega, \omega', E_e) &= \frac{1}{\omega \omega'} \left[-a_0(\omega, \omega', E_e) + \frac{8}{3} E_e^2 (\omega^3 + \omega'^3) - \frac{4}{3} E_e (\omega + \omega')^2 (\omega'^2 - 2\omega\omega' + 3\omega^2) \right. \\ &\quad \left. + \frac{4}{15} (\omega + \omega')^3 (\omega'^2 - 3\omega\omega' + 6\omega^2) \right], \end{aligned} \quad (C68)$$

$$c_0(\omega, \omega', E_e) = \frac{\omega^2}{\omega'} \left[\frac{8}{3} \omega'^2 + 4\omega\omega' + \frac{8}{5} \omega^2 \right] - E_e \left[\frac{16}{3} \omega^2 + 4 \frac{\omega^3}{\omega'} \right] + \frac{8}{3} E_e^2 \frac{\omega^2}{\omega'}, \quad (C69)$$

$$d_0(\omega, \omega', E_e) = \frac{4}{15} \frac{\omega'^4}{\omega} - \frac{4}{3} \frac{\omega'^3}{\omega} E_e + \frac{8}{3} \frac{\omega'^2}{\omega} E_e^2. \quad (C70)$$

The result for J_1^I is an expression similar to equation (C66) but with the subscripts 0 replaced by 1, and with

$$a_1(\omega, \omega', E_e) = \frac{1}{\omega^2 \omega'^2} \left[\frac{16}{35} E_e^7 - \frac{4}{5} E_e^6 (\omega + 3\omega') + \frac{4}{15} E_e^5 \omega' (13\omega + 18\omega') - \frac{4}{3} E_e^4 \omega'^2 (4\omega + 3\omega') + \frac{8}{3} E_e^3 \omega \omega'^3 \right], \quad (C71)$$

$$\begin{aligned} b_1(\omega, \omega', E_e) = & \frac{1}{\omega^2 \omega'^2} \left[-a_1(\omega, \omega', E_e) - E_e^2 \left(\frac{12}{5} \omega^5 + \frac{4}{3} \omega^4 \omega' + \frac{4}{3} \omega \omega'^4 + \frac{12}{5} \omega'^5 \right) \right. \\ & + E_e \left(\frac{16}{5} \omega^6 + \frac{28}{5} \omega^5 \omega' + \frac{8}{3} \omega^4 \omega'^2 + \frac{28}{15} \omega \omega'^5 + \frac{8}{5} \omega'^6 \right) \\ & \left. - \left(\frac{8}{7} \omega^7 + \frac{16}{5} \omega^6 \omega' + \frac{16}{5} \omega^5 \omega'^2 + \frac{4}{3} \omega^4 \omega'^3 + \frac{8}{15} \omega \omega'^6 + \frac{12}{35} \omega'^7 \right) \right], \end{aligned} \quad (C72)$$

$$c_1(\omega, \omega', E_e) = -\frac{\omega^2}{\omega'^2} \left(\frac{8}{7} \omega^3 + \frac{16}{5} \omega^2 \omega' + \frac{16}{5} \omega \omega'^2 + \frac{4}{3} \omega'^3 \right) + E_e \frac{\omega^2}{\omega'^2} \left(\frac{16}{5} \omega^2 + \frac{28}{5} \omega \omega' + \frac{8}{3} \omega'^2 \right) - E_e^2 \frac{\omega^2}{\omega'^2} \left(\frac{12}{5} \omega + \frac{4}{3} \omega' \right), \quad (C73)$$

$$d_1(\omega, \omega', E_e) = -\frac{\omega'^4}{\omega^2} \left(\frac{8}{15} \omega + \frac{12}{35} \omega' \right) + E_e \frac{\omega'^3}{\omega^2} \left(\frac{28}{15} \omega + \frac{8}{5} \omega' \right) - E_e^2 \frac{\omega'^2}{\omega^2} \left(\frac{4}{3} \omega + \frac{12}{5} \omega' \right). \quad (C74)$$

J_1^{II} is obtained from J_1^I by equation (C64). The constant G^2 in equation (C62) should have the value given by equation (C51) in order that the term B_{TP} given by equation (A9) have the required units of cm^{-1} . The thermal production rates for the $\bar{\nu}_e$'s and the muon and tau neutrinos are obtained by performing the same transformations of C_V and C_A that were described above for NES.

Figure 35 shows the integrated energy production rates, assuming the neutrino occupancy to be zero, for the ν_e 's, $\bar{\nu}_e$'s, and each of the ν_τ 's. (The latter is an average over particle and antiparticle production rates, as described in § IIb of the paper.) The density range of the matter is from 10^{10} to $10^{12} \text{ g cm}^{-3}$, $Y_e = 0.3$, and the dimensionless entropy per baryon of the matter is 8. These states are representative of the postshock conditions of the matter. The figure also shows the $\nu_e - \bar{\nu}_e$ integrated energy production rates as given by the older CVC theory, which were obtained by setting $C_V = C_A = 1$ in equation (C63), and the $\nu_e - \bar{\nu}_e$ integrated energy production rates as given by the fitting formula of Beaudet, Petrosian, and Salpeter (1967).

Figures 36a and 37a show, respectively, the neutrino energy production spectra for matter at $\rho = 10^{11} \text{ g cm}^{-3}$, $s = 1.5$, and $Y_e = 0.4$, which is representative of the infalling matter, and $\rho = 10^{11} \text{ g cm}^{-3}$, $s = 8$, and $Y_e = 0.3$, which is representative of the postshock matter. The neutrino occupancy was taken to be zero. The neutrino production terms are the terms on the right-hand

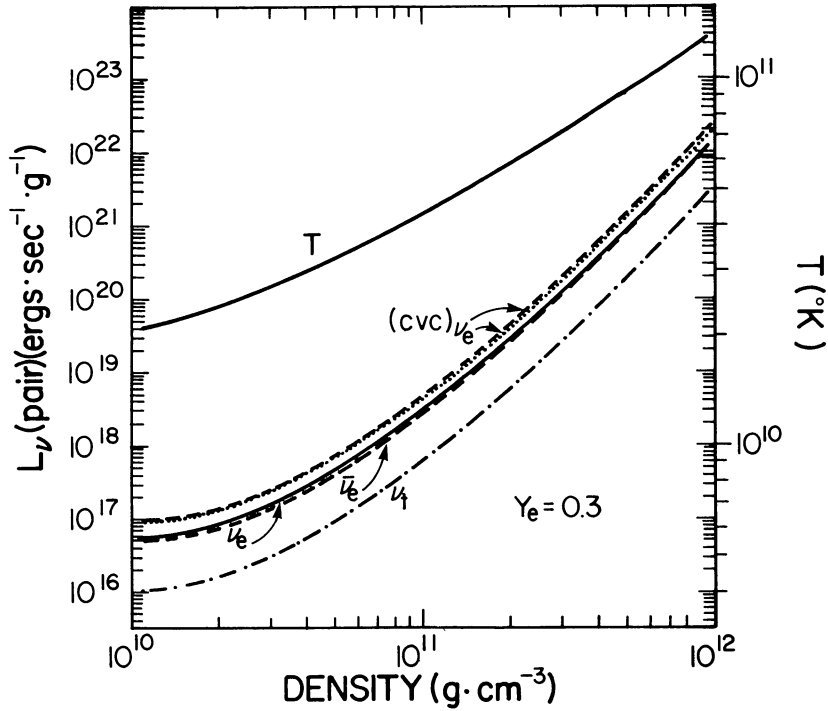


FIG. 35.—Integrated neutrino energy production rates by electron-positron pair annihilation as a function of density for matter at a dimensionless entropy per baryon ($s = S/kN_B$) of 8 and an electron fraction of 0.3. The final-state occupancy of the neutrinos is zero. The energy production rates for the ν_e 's, $\bar{\nu}_e$'s, and ν_t 's (where ν_t represents ν_μ , $\bar{\nu}_\mu$, ν_τ , or $\bar{\nu}_\tau$), are given by the solid line labeled ν_e , the dashed line labeled $\bar{\nu}_e$, and the dot-dash line labeled ν_t , respectively. The dashed line labeled $(CVC)\nu_e$ gives the sum of the energy production rates for the ν_e 's and $\bar{\nu}_e$'s as given by our expressions with the values of the parameters C_V and C_A set in accordance with the older CVC theory. The dotted line labeled $(CVC)\nu_e$ gives the same quantity as computed by the fitting formulae of Beaudet, Petrosian, and Salpeter (1967). The solid line labeled T gives the values of the temperature (right ordinate) as a function of density used to compute the neutrino production rates for this figure.

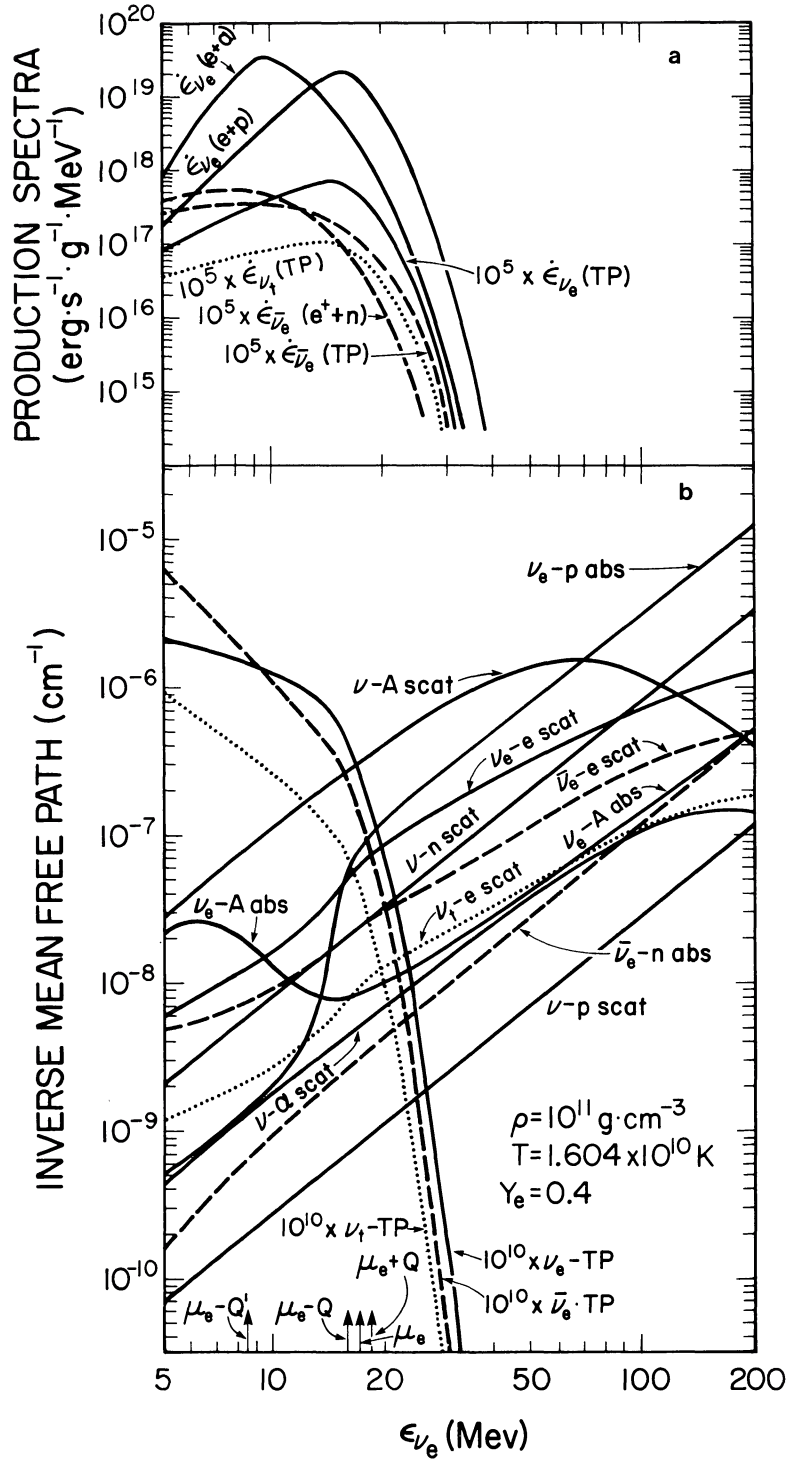


FIG. 36.—(a) Neutrino energy production spectra for matter at $\rho = 10^{11} \text{ g cm}^{-3}$, $T = 1.604 \times 10^{10} \text{ K}$, and $Y_e = 0.4$ ($s = S/kN_B = 1.5$). The final-state occupancy of the neutrinos is zero. The composition of the matter by mass fraction is $X_n = 5.917 \times 10^{-2}$, $X_p = 2.357 \times 10^{-3}$, $X_\alpha = 1.219 \times 10^{-1}$, and $X_A = 8.166 \times 10^{-1}$. The solid lines show the ν_e energy production spectra for electron capture on protons, $\dot{\epsilon}_{\nu_e}(e + p)$; electron capture on heavy nuclei, $\dot{\epsilon}_{\nu_e}(e + A)$; and thermal production (i.e., electron-positron pair annihilation), $\dot{\epsilon}_{\nu_e}(\text{TP})$. The dashed lines show the $\bar{\nu}_e$ energy production spectra for positron capture on neutrons, $\dot{\epsilon}_{\bar{\nu}_e}(e^+ + n)$, and thermal production $\dot{\epsilon}_{\bar{\nu}_e}(\text{TP})$. The dotted lines show the ν_t energy production spectrum for thermal production $\dot{\epsilon}_{\nu_t}(\text{TP})$, where ν_t denotes either ν_μ , $\bar{\nu}_\mu$, ν_τ , or $\bar{\nu}_\tau$. (b) Neutrino transport inverse mean free paths for the neutrino interactions considered in this paper. The final-state occupancy of the neutrinos is zero. The thermodynamic state of the matter is the same as in Fig. 36a. Also shown by the upward-pointing arrows on the abscissa are the values of the quantities $\mu_e - Q'$, $\mu_e - Q$, and $\mu_e - Q'$, where Q and Q' are defined in equations (C13) and (C28), respectively.

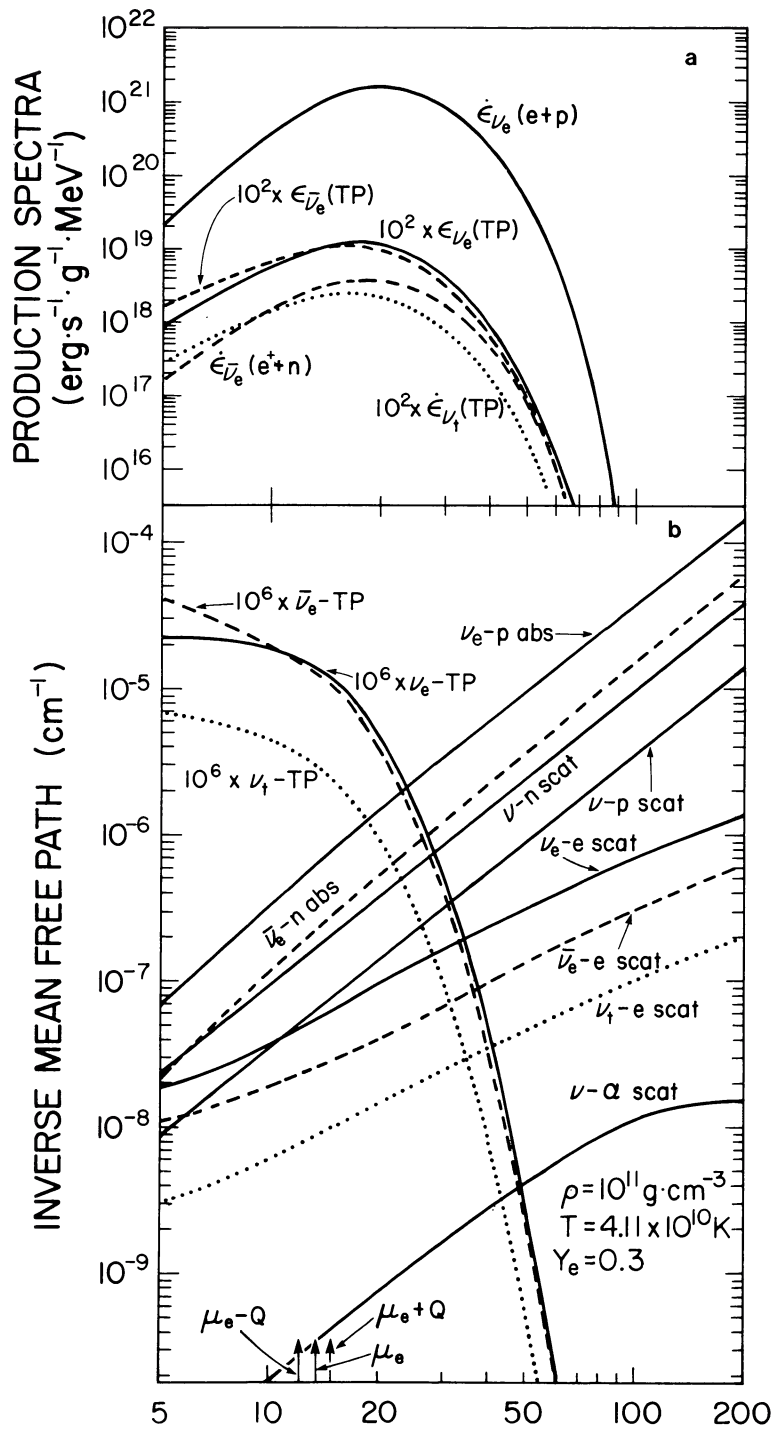


FIG. 37.—(a) Same as Fig. 36a, but for matter at $\rho = 10^{11} \text{ g cm}^{-3}$, $T = 4.11 \times 10^{10} \text{ K}$, and $Y_e = 0.3$ ($s = S/kN_B = 8$). The final-state occupancy of the neutrinos is zero. The composition of the matter by mass fraction is $X_n = 0.6974$, $X_p = 0.2949$, $X_\alpha = 7.638 \times 10^{-3}$, and $X_A = 0$. (b) Same as Fig. 36b, but for matter at the thermodynamic state in Fig. 37a.

side of the neutrino diffusion equation (A27). In the limit of zero neutrino occupancy, the only nonzero production terms are $j(\omega)$ and the thermal production contribution to $C^{(0)}(\omega)$ in equation (A28). Each neutrino energy production spectrum shown in the graphs was obtained by using the appropriate production term from equation (A28) in equation (A53) and dividing by the density. Thus, for electron capture on nuclei, denoted by $\epsilon_{\nu_e}(e + A)$, equation (C27) was used for $j(\omega)$; for electron capture on free protons, denoted by $\epsilon_{\nu_e}(e + p)$, equation (C15) was used for $j(\omega)$; for positron capture on neutrons, denoted by $\epsilon_{\bar{\nu}_e}(e^+ + n)$, equation (C20) was used for $j(\omega)$; for the thermal production rates, denoted by $\dot{\epsilon}_{\nu}(\text{TP})$, where ν refers either to a ν_e , a $\bar{\nu}_e$, or a ν_t , equations (C64) and (C66)–(C70) were used in equation (C62) and the latter used in equation (A45). The thermal neutrino production rate, $\dot{\epsilon}_{\nu}(\text{TP})$, shown in the graphs is for each type of thermal neutrino. Muon and tau neutrinos and their antiparticles were included as “thermal” neutrinos in this paper, so the total thermal neutrino production rate is 4 times the rate shown in the figures for $\dot{\epsilon}_{\nu}(\text{TP})$.

It is interesting to note that while the integrated number production rates for the ν_e 's and the $\bar{\nu}_e$'s are the same, their energy production spectra are different, as are their integrated energy production rates. This difference can be traced to the form of the spin-summed matrix element (eq. [C52]) for the process, and the fact that the average energy of the electrons is greater than that of the positrons. The latter follows from the fact that $N_e - N_{e^+} > 0$, so that $\mu_e > \mu_{e^+}$. In $\nu_e - \bar{\nu}_e$ production, the first term in equation (C62) is about a factor of 10 larger than the second. (The third term is negligible.) In the extreme relativistic limit ($E_e \gg m_e c^2$), the first term can be rewritten as $(C_V + C_A)^2 E_e \omega E_e \omega' (1 - \cos \theta_{e^+ - \nu_e})(1 - \cos \theta_{e - \bar{\nu}_e})$, where $\theta_{e^+ - \nu_e}$ and $\theta_{e - \bar{\nu}_e}$ are the angles between the incoming e^+ and the outgoing ν_e , and the incoming e and the outgoing $\bar{\nu}_e$, respectively. In the center-of-momentum frame the direction of the outgoing ν_e will be correlated with that of the incoming e , and likewise for directions of the $\bar{\nu}_e$ and the e^+ . Because of the greater average energy of the e , the center-of-momentum frame will drift (in the rest frame of the fluid), on the average, in the direction of the incoming e . The ν_e and $\bar{\nu}_e$ energies are, of course, equal in the center-of-momentum frame, but in transforming back to the rest frame of the fluid the energy of the ν_e 's will be increased and that of the $\bar{\nu}_e$'s decreased.

Figures 36b and 37b show the contributions to the inverse neutrino transport mean free path (eq. [A26]) from the various neutrino-matter interactions considered here. The matter is at the same thermodynamic states as specified for Figures 36a and 37a, respectively, and the neutrino occupancy is zero. The contributions to the inverse mean free paths are given by equations (C13) and (C15) for ν_e absorption on free neutrons, (C27) and (C29) for ν_e absorption on nuclei, (C19) and (C20) for $\bar{\nu}_e$ absorption on free protons, (C38) and (C39) in (A40) for ν - p and ν - n scattering, (C44) and (C45) in (A41) for ν - A scattering, (C50) in (A38) for ν_e - e scattering, and (C62)–(C64) with (C67)–(C70) in (A47) for ν - $\bar{\nu}$ thermal production.

Several of the curves in the figures deserve comment. Under conditions of high electron degeneracy (low matter entropy) and with a neutrino occupancy of zero, $1/\lambda$ for ν_e - n absorption is dominated by $j(\omega)$ (eq. [C15]) for $\omega < \mu_e - Q$, and by $1/\lambda^{(a)}(\omega)$ (eq. [C17]) for $\omega > \mu_e - Q$ because of the electron Fermi functions. The ratio of $1/\lambda^{(a)}$ to $j(\omega)$ for this process at $\omega = \nu_e - Q$ is essentially the ratio of the free neutron density to the free proton density (about 25 for the matter at $s = 1.5$), so $1/\lambda$ for ν_e - n absorption in Figure 36b increases by about this ratio near $\omega = \mu_e - Q$. Similarly, $1/\lambda$ for ν_e - A absorption is dominated by $j(\omega)$ (eq. [C27]) for $\omega < \mu_e - Q$, and by $1/\lambda^{(a)}(\omega)$ (eq. [C29]) for $\omega > \mu_e - Q'$. Here the ratio of $1/\lambda^{(a)}$ to $j(\omega)$ is the ratio of the excited daughter nucleus density to the parent nucleus density, or about $e^{-\beta\Delta} \approx 0.11$. Therefore, $1/\lambda$ for ν_e - A absorption decreases by about this ratio near $\omega = \mu_e - Q'$. The quantity $1/\lambda$ for ν - A scattering exhibits a decline at high neutrino energies owing to the composite nature of the target, which causes the scattering to become increasingly forward-peaked as the neutrino energy is increased. A similar effect is beginning to become manifest for ν - a scattering. Because of the absence of neutrino occupancy, the contribution to $1/\lambda$ for thermal production from ν - $\bar{\nu}$ annihilation is zero, so $1/\lambda$ for this process is due entirely to ν - ν production, and thus peaks at $\omega \approx \omega' \approx \mu_e$ for ν_e - $\bar{\nu}_e$ production, and at about $\omega \approx \omega' \approx kT$ for ν_t - $\bar{\nu}_t$ production.

APPENDIX D

HYDRODYNAMICS

Assume a metric having the following spherically symmetric form (e.g., May and White 1967):

$$a^2 c^2 dt^2 - b^2 d\mu^2 - R^2 d\Omega^2. \quad (\text{D1})$$

The energy tensor $T^{\alpha\beta}$ for the system is given by

$$T^{\alpha\beta} = \rho w u^\alpha u^\beta + P g^{\alpha\beta} + t^{\alpha\beta}, \quad (\text{D2})$$

where the first two terms on the right-hand side describe the matter, assumed to be a perfect fluid, with ρ the proper rest-mass density, P the proper matter pressure, and w given by equation (D12). The last term is the contribution of the neutrinos to the energy tensor, given by (Lindquist 1966)

$$t^{\alpha\beta} = c^3 \int d\mathcal{P} p^\alpha p^\beta F(x, p), \quad (\text{D3})$$

where $d\mathcal{P}$ is the invariant energy-momentum volume element and $F(x, p)$ the invariant neutrino distribution function.

In the comoving frame of the fluid (with the first space axis in the radial direction), use of the relation $F = cf/(2\pi\hbar c)^3$, where F is defined below equation (A1), and use of equations (D2) and (A10) in equation (D3) give $t^{00} = g^{00}E_\nu$, $t^{ii} = -g^{ii}P_\nu$, $t^{10} = t^{01} = \sqrt{(-g^{00}g^{11})F_\nu/c}$ for the nonzero $t^{\alpha\beta}$, where E_ν , P_ν , and F_ν are the neutrino energy density, neutrino pressure, and neutrino energy flux, respectively, given by equations (A50)–(A52). From equations (D2) and (D3) the explicit expression for the energy tensor of the system is thus given by

$$T_\alpha^\beta = \begin{pmatrix} \rho c^2 + \epsilon + E_\nu & (a/b)F_\nu & 0 & 0 \\ -(b/ac^2)F_\nu & -P - P_\nu & 0 & 0 \\ 0 & 0 & -P - P_\nu & 0 \\ 0 & 0 & 0 & -P - P_\nu \end{pmatrix}. \quad (\text{D4})$$

The hydrodynamic equations follow from the Einstein field equations, the zero divergence of ρu^ν (rest-mass conservation) and of $T^{\alpha\beta}$ (momentum-energy conservation), and the neutrino diffusion equations. After considerable algebra, they can be cast in a form closely paralleling equations (33)–(41) of May and White (1967), which do not include neutrino diffusion. They are

$$u_t = -a \left[4\pi R^2 \frac{\Gamma}{w} P_\mu + \frac{mG}{R^2} + \frac{4\pi G}{c^2} (P + P_\nu) R - \frac{\Gamma}{\rho w} (F)_{\nu \rightarrow \text{mat}} \right], \quad (\text{D5})$$

$$R_t = au, \quad (\text{D6})$$

$$\frac{(\rho R^2)_t}{\rho R^2} = -\frac{au_\mu}{R_\mu} + \frac{4\pi G}{c^4} \frac{R}{\Gamma} aF_\nu, \quad (\text{D7})$$

$$\epsilon_t = -P \left(\frac{1}{\rho} \right)_t + \frac{a}{\rho} \left(\frac{\partial E}{\partial t} \right)_{\nu \rightarrow \text{mat}}, \quad (\text{D8})$$

$$(aw)_\mu / (aw) = \left[\epsilon_\mu + P(1/\rho)_\mu + (F)_{\nu \rightarrow \text{mat}} / 4\pi R^2 \rho^2 \right] / wc^2, \quad (\text{D9})$$

$$m = 4\pi \int_0^\mu [\rho(1 + \epsilon/c^2) + E_\nu/c^2 + uF_\nu/\Gamma c^4] R^2 R_\mu d\mu, \quad (\text{D10})$$

$$\Gamma \equiv (1/b)R_\mu = 4\pi\rho R^2 R_\mu = 1 + u^2/c^2 - 2mG/Rc^2, \quad (\text{D11})$$

$$w = 1 + \epsilon/c^2 + P/\rho c^2, \quad (\text{D12})$$

where $(F)_{\nu \rightarrow \text{mat}}$ and $(\partial E/\partial t)_{\nu \rightarrow \text{mat}}$ are the negatives of equations (A57) and (A53), respectively; the subscripts μ and t denote $\partial/\partial\mu$ and $\partial/\partial t$, respectively; μ is the total rest mass enclosed in a sphere of “radius” μ ; and ϵ is the proper matter internal energy per unit mass.

The boundary conditions were taken to be $u = 0$, $R = 0$, and $\Gamma = 1$ at $\mu = 0$, and $a = 1$ and $P = P_0$ at the outer boundary of the mass configuration, where P_0 is the initial pressure outside the last mass zone.

Equations (D5)–(D12) were differenced in a manner similar to the scheme applied to equations (33)–(41) of May and White (1967) as described by Van Riper (1979). The pseudoviscosity was chosen so that it vanished automatically during homologous collapse.

APPENDIX E

NUMERICAL TESTS

The computer code was subjected to numerous test problems and self-consistency checks. Some of the more important of these are described briefly below.

I. CONSERVATION OF ENERGY

The numerical solution for the changes in the temperatures, electron fractions, and zeroth moments of the NODs due to neutrino interactions and transport proceeds implicitly. Monitoring the constancy of the quantity $E = E_1 + E_2 + E_3$, where E_1 is the total energy of all the neutrinos that have propagated beyond the computational grid, E_2 is the total work done by the matter on the external pressure, and E_3 is the total gravitational energy of the core, provides a test of the self-consistency and stability of the numerical solution. It was found that whereas the internal energy, gravitational binding energy, neutrino energy, and matter

kinetic energy achieved values of 8×10^{52} , 8×10^{52} , 8×10^{51} , and 10^{52} ergs, respectively, during the course of a calculation, E varied by only 3×10^{49} ergs up to core bounce. This appears to be a rather sensitive test. Any numerical instability or inconsistency in the numerical treatment of the matter and neutrinos immediately manifests itself by a large change in E . Even removing the neutrino-matter decoupling algorithm for neutrino-transparent regimes resulted in an order of magnitude larger variation in E .

II. CONSERVATION OF ENTROPY FOR ADIABATIC, DISSIPATIONLESS FLOW

Since shocks are absent during the core infall, the entropy change of the matter in the core during this stage is due entirely to the weak interactions. (The matter has been assumed to be equilibrated with respect to electromagnetic and strong interactions.) It is essential that this entropy change be computed accurately, since the entropy change has a sensitive influence on the core composition and therefore on the β -rates and the core deleptonization. A necessary condition for an accurate computation is that there be no change in the core entropy during infall if the weak interactions are turned off. As a test of code, the infall of the core was computed with all weak interactions turned off. The results are given in Figure 23 (model AD). Although the hydrodynamic equations were not differenced to conserve entropy explicitly under nondissipative conditions, it was found that the entropy varied by at most 2% about a constant value during infall.

III. LEPTON CONSERVATION

Another sensitive test for the consistency and stability of the solution for the Y_e 's and the neutrino variables is the local conservation of leptons. To test for this, the number of leptons (electrons + neutrinos – antineutrinos) currently residing in each mass zone was added to the total net lepton transport through the zone boundaries for comparison with the incident number of leptons residing in that zone. It was found that by core turnaround the final lepton number differed by 0.01%–0.1% in the inner zones to about 1% in the outer zones. Globally, the total lepton number was conserved to within 0.01%.

IV. NEUTRINO-ELECTRON SCATTERING

An accurate computation of NES is essential because of its important role in the core deleptonization, as discussed in §§ IIIc(i) and IIIc(iii). A direct and implicit solution of the MGFLDA with the NES terms included was obtained as described in Appendix B. This numerical scheme was tested by comparing the results of test problems with the Monte Carlo simulations of NES by Tubbs *et al.* (1980). These comparisons are shown in Figures 38 and 39. Except for model HC at $\rho = 10^{10}$ g cm $^{-3}$ (which neither the Fokker-Planck nor the thermal relaxation schemes tested by Tubbs *et al.* 1980 was able to track), the numerical scheme used here gave results that closely approximated the Monte Carlo results.

V. NEUTRINO PRODUCTION BY ELECTRON-POSITRON PAIR ANNIHILATION

A direct solution of the MGFLDA with the pair annihilation terms included was obtained, as described in Appendix B, which was fully implicit for the ν_μ and ν_τ neutrino pairs, and partially implicit for the ν_e 's and $\bar{\nu}_e$'s (i.e., the ν_e and $\bar{\nu}_e$ fields were separately solved for). No rigorous, dynamic results are known which could be used to test all aspects of the process. In lieu of such a comparison, the integrated production rates are shown in Figure 35, and a comparison is made of these rates as computed with the older CVC parameters, with the rates given by the fitting formula of Beaudet, Petrosian, and Salpeter (1967). The figure shows these rates to be very close to each other. Some differential production rates for the process are shown in Figures 36a and 37a, and their contributions to the inverse neutrino transport mean free paths are shown in Figures 36b and 37b.

VI. NEUTRINO TRANSPORT WITHOUT SCATTERING; BOUNDARY CONDITIONS

To test the numerical scheme for neutrino transport and the choice of the outer boundary condition, a test for which an “analytic” solution could be obtained from the neutrino Boltzmann equation was considered. (“Analytic” in this context means that the solution could be reduced to one straightforward numerical integration over angle.) A static stellar core of radius $R = 4.9 \times 10^8$ cm was constructed with density and temperature profiles

$$\rho = \begin{cases} 10^{12} \text{ g cm}^{-3}, & r < r_0 \\ 10^{11} \text{ g cm}^{-3}, & r_0 < r < R, \end{cases}$$

$$T = \begin{cases} 3 \times 10^{10} \text{ K}, & r < r_0 \\ 2 \times 10^{10} \text{ K}, & r_0 < r < R, \end{cases}$$

and $Y_e = 0.4$ in both regions. The material was assumed to be in nuclear statistical equilibrium corresponding to the local values of the three parameters ρ , T , and Y_e . Values of 4×10^7 , 9×10^7 , and 1.9×10^8 cm were chosen for r_0 . To further increase the contrast between the two regions, the absorption and emission rates of ν_e 's on free nucleons, which was the only ν_e -matter interaction considered, were multiplied in the outer region by 10^{-2} . The calculation was begun with the ν_e distribution equal to zero and continued until it became stationary.

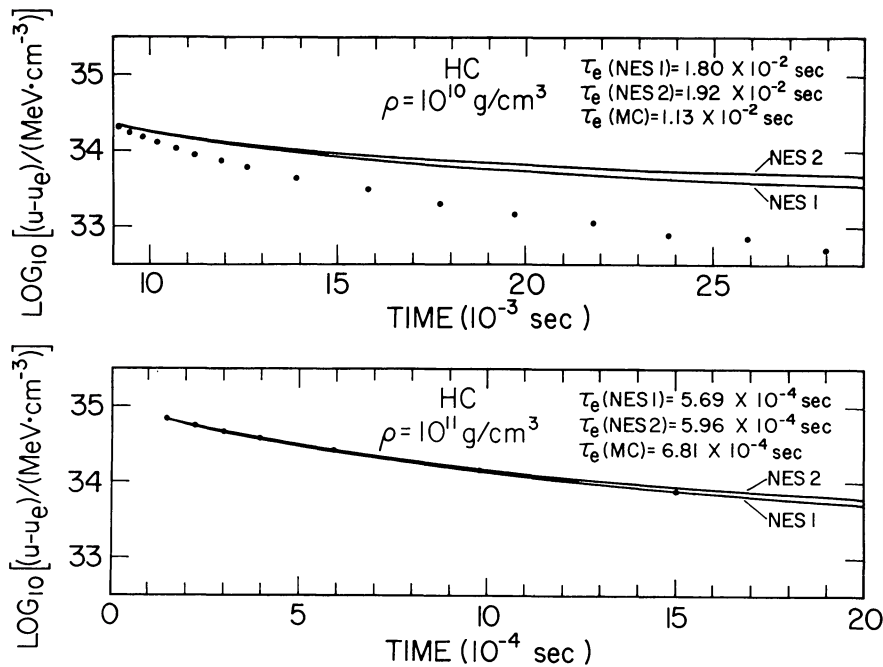


FIG. 38.—Neutrino thermalization for models HC described in Tubbs *et al.* (1980). The graphs show the results from the onset of neutrino-electron scattering (NES). Monte Carlo data are shown as solid dots. The solid lines are obtained from the numerical treatment of NES described in §§ IIb and IIc, and Appendices A, B, and C of this paper. The results labeled *NES1* and *NES2* were obtained using 10 energy zones with zone-centered energies in geometric progression from 2 to 45.25 MeV, and from 4 to 220 MeV, respectively. The former distribution of zone energies was optimized from the Tubbs *et al.* (1980) neutrino thermalization problems; the latter distribution of zone energies was that used in the collapse calculations. The quantities u and u_e are the instantaneous and equilibrated neutrino energy density (MeV cm^{-3}), respectively. The time τ_e (measured from zero) is the time at which the neutrino energy density achieves the value $u_e + (u_0 - u_e)/e$, where u_0 is the neutrino energy density at the onset of NES.

The results are compared with the “analytic” solutions in Figures 40–42. Three different outer boundary conditions were tried: (1) the boundary condition used in the collapse calculation and described by equations (B27)–(B31); (2) a simpler version of this boundary condition (referred to as “linear”) with K_k in equation (B29) linearly interpolated in d_k/R between the values of 0.5774 and 0.3333; and (3) a “zero” boundary condition in which $\psi^{(0)}$ was set to zero in an auxiliary zone just outside the outer boundary. A glance at Figures 40–42 reveals that the solutions for $\psi^{(1)}$, shown in Figure 41, and therefore for the number luminosity L_N , the energy luminosity L_E , and the stress F_ν , shown in Figure 42, are so close for the different outer boundary conditions that they cannot be distinguished in the figures. The solutions for $\psi^{(0)}$ differed from one another only near the surface. The choice of the outer boundary condition is therefore not critical.

The solutions for $\psi^{(1)}$, L_N , L_E , and F_ν are quite close to the analytic solutions in the important transport regime in the vicinity of and outward from the discontinuity. The solutions for $\psi^{(0)}$ were close to the analytic solutions for low neutrino energies, but deviated from them significantly in the vicinity of the discontinuity for high neutrino energies.

VII. NEUTRINO TRANSPORT WITH ISOENERGETIC AND NEUTRINO-ELECTRON SCATTERING

Bruenn and Ballester (1980) obtained accurate solutions to steady state, bigroup neutrino transport with isoenergetic and neutrino-electron scattering for idealized conditions representative of the outer core or envelope of a star whose inner core is undergoing gravitational collapse. These solutions were compared, in that paper, with solutions obtained with an earlier version of the neutrino transport code, and the results of the latter agreed well with the accurate solutions in all cases of relevance to gravitational collapse. The solutions given by the present version of the neutrino transport code were compared with the accurate solutions. Again, the agreement was good in all cases of relevance to gravitational collapse. The results obtained were similar to those shown for the flux-limited diffusion approximation in Figures 1–8 of Bruenn and Ballester (1980).

VIII. HYDRODYNAMICS

Tests involving the collapse of a pressure-free, uniformly dense sphere (May and White 1967) and the propagation of a plane shock into an exponentially decreasing density gradient (Grover and Hardy 1966) were performed, and the numerical results agreed well with the analytical solutions. In addition, the calculation described above in § II of this appendix was continued through core turnaround and the propagation of the shock to the core edge. The total gravitational energy was never found to fluctuate from a constant value by more than 3×10^{49} ergs, although individual contributions to this energy approached 10^{53} ergs.

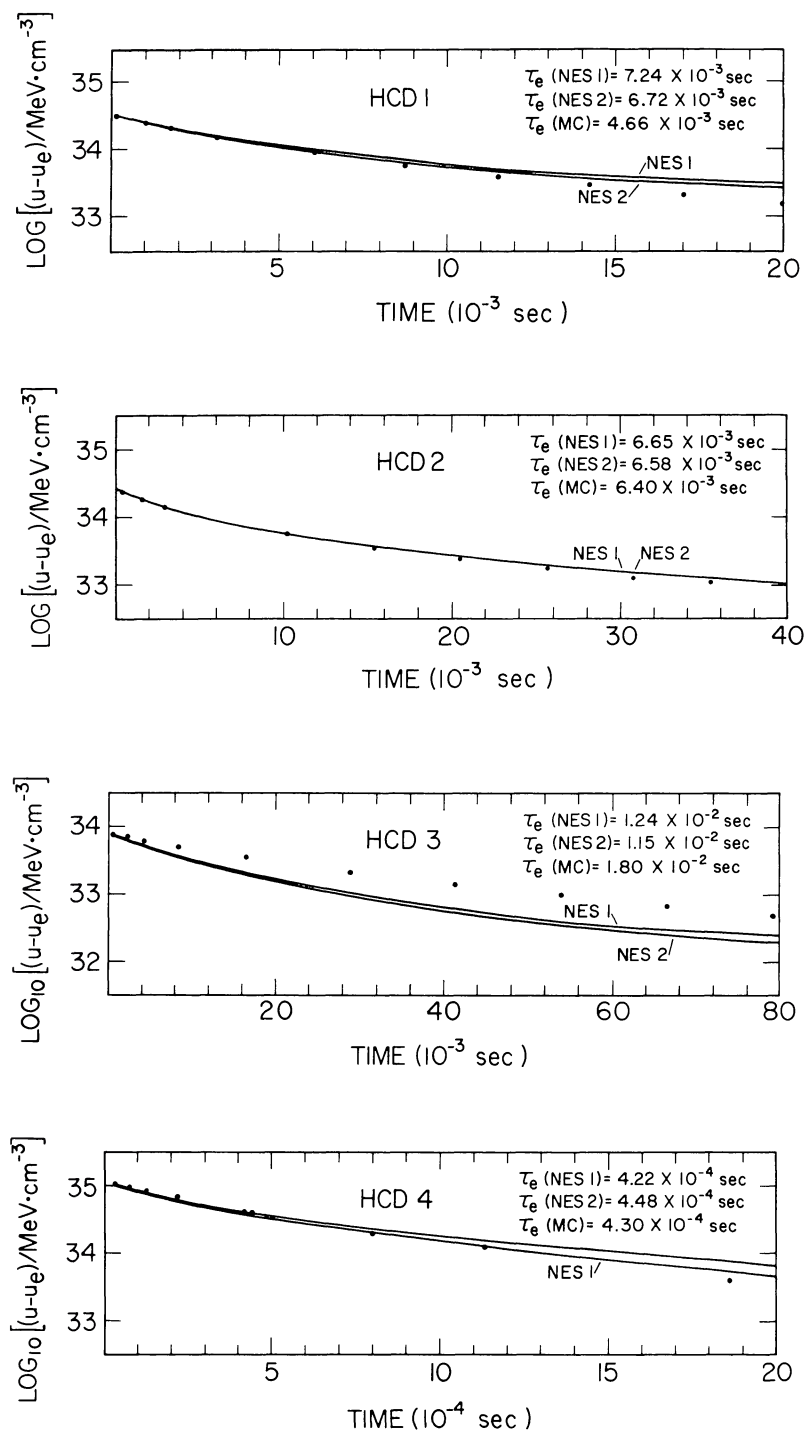


FIG. 39.—Same as Fig. 38, but for the neutrino thermalization models HCD described in Tubbs *et al.* (1980)

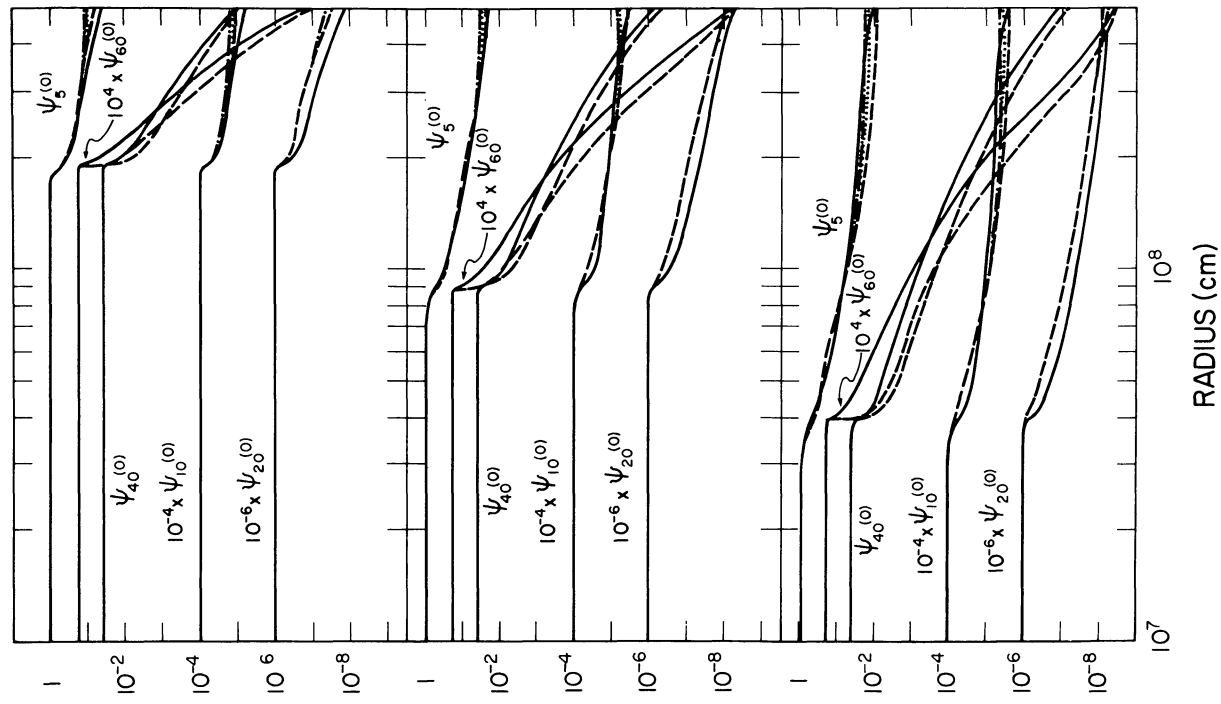


FIG. 40

FIG. 40.—Comparisons of $\psi_w^{(0)}$, the zeroth moment of the ν_e occupation distribution, as computed by our MGFLDA with “analytic” solutions for $\psi_w^{(0)}$ (solid lines) for the test problem described in Appendix E. The subscript affixed to $\psi^{(0)}$ in the figure is the ν_e energy in MeV. The dashed, dotted, and dot-dash lines represent the MGFLDA results with the outer boundary condition described in Appendix B, the “linear” outer boundary condition, and the “zero” outer boundary condition, respectively. Where only the solid line is drawn, all results are essentially identical. Where the solid and dashed lines only are drawn, the three MGFLDA results are essentially identical and are given by the dashed line. Values of r_0 are (a) 1.9×10^8 cm, (b) 9×10^7 cm, and (c) 4×10^7 cm.

FIG. 41.—Same as Fig. 40, but for $\psi_w^{(1)}$, the first moment of the ν_e occupation distribution

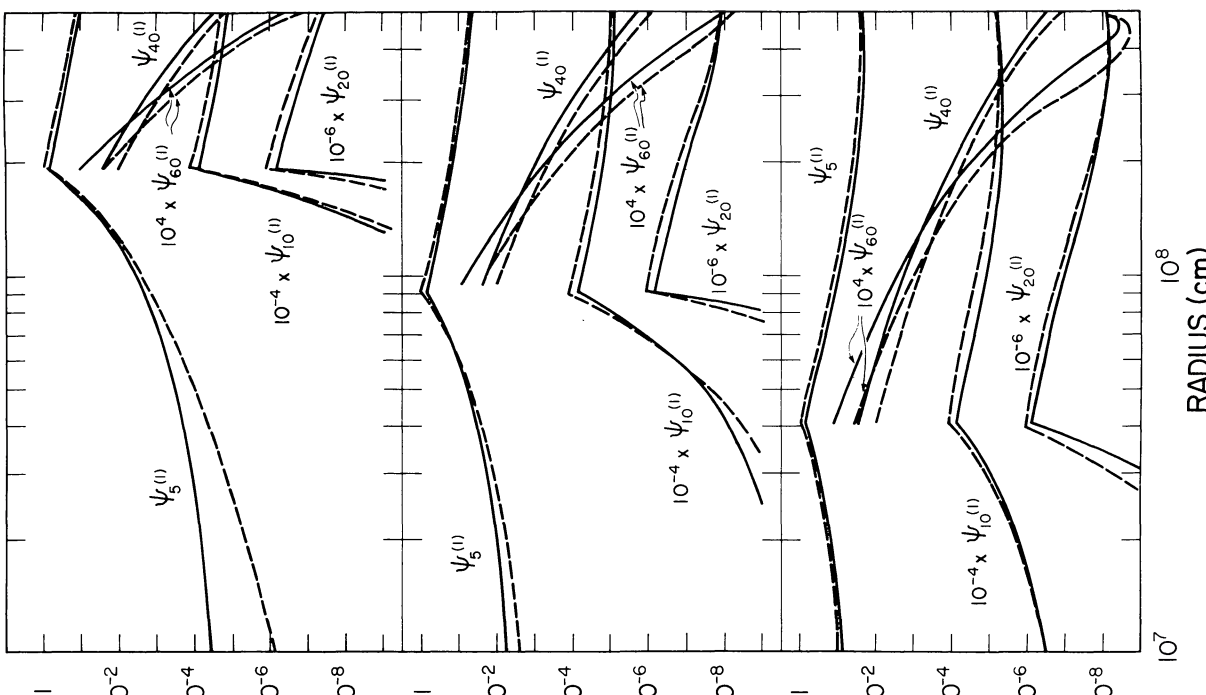


FIG. 41

FIG. 41.—Comparisons of $\psi_w^{(1)}$, the zeroth moment of the ν_e occupation distribution, as computed by our MGFLDA with “analytic” solutions for $\psi_w^{(1)}$ (solid lines) for the test problem described in Appendix E. The dashed, dotted, and dot-dash lines represent the MGFLDA results with the outer boundary condition described in Appendix B, the “linear” outer boundary condition, and the “zero” outer boundary condition, respectively. Where only the solid line is drawn, all results are essentially identical. Where the solid and dashed lines only are drawn, the three MGFLDA results are essentially identical and are given by the dashed line. Values of r_0

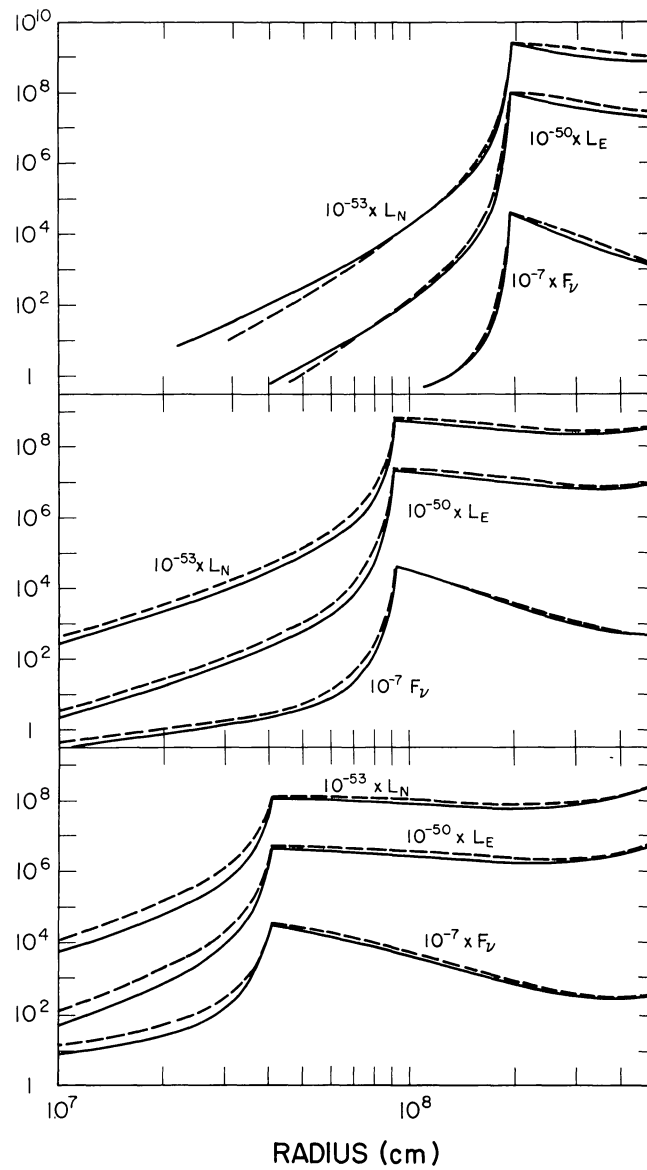


FIG. 42.—Same as Fig. 40, but for the ν_e number luminosity L_N (s^{-1}), the ν_e energy luminosity L_E (ergs s^{-1}), and the ν_e -matter stress F_ν (dynes g^{-1})

REFERENCES

- Arnett, W. D. 1967, *Canadian J. Phys.*, **45**, 1621.
 _____. 1977a, *Ap. J. Suppl.*, **35**, 145.
 _____. 1977b, *Ap. J.*, **218**, 215.
 _____. 1978, *Ap. J.*, **219**, 1008.
 _____. 1980, *Ap. J.*, **237**, 541.
 _____. 1981, in *Essays in Nuclear Astrophysics*, ed. C. A. Barnes, D. D. Clayton, and D. N. Schramm (Cambridge: Cambridge University Press).
 _____. 1982a, *Ap. J. (Letters)*, **263**, L55.
 _____. 1982b, in *Supernovae: A Survey of Current Research*, ed. M. J. Rees and R. J. Stoneham (Dordrecht: Reidel), p. 221.
 Arnett, W. D., and Falk, S. W. 1976, *Ap. J.*, **210**, 733.
 Arnett, W. D., and Schramm, D. N. 1973, *Ap. J. (Letters)*, **184**, L47.
 Baade, W., and Zwicky, F. 1934, *Proc. Nat. Acad. Sci.*, **20**, 254.
 Barkat, Z. 1977, in *Supernova*, ed. D. N. Schramm (Dordrecht: Reidel), p. 131.
 Beaudet, G., Petrosian, V., and Salpeter, E. E. 1967, *Ap. J.*, **150**, 979.
 Berestetskii, V. B., Lifshitz, E. M., and Pitaevskii, L. P. 1971, *Relativistic Quantum Theory* (New York: Pergamon).
 Bethe, H. A., Applegate, J. H., and Brown, G. E. 1980, *Ap. J.*, **241**, 343.
 Bethe, H. A., Brown, G. E., Applegate, J., and Lattimer, J. M. 1979, *Nucl. Phys. A*, **324**, 487.
 Bilenki, S. M. 1982, *Introduction to the Physics of Electroweak Interactions* (New York: Pergamon).
 Bjorken, J. D., and Drell, S. D. 1964, *Relativistic Quantum Mechanics* (New York: McGraw-Hill).
 _____. 1965, *Relativistic Quantum Fields* (New York: McGraw-Hill).
 Bludman, S. A., Lichtenstadt, I., and Hayden, G. 1982, *Ap. J.*, **261**, 661.
 Bludman, S. A., and Van Riper, K. A. 1978, *Ap. J.*, **224**, 631.
 Bowers, R., and Wilson, J. R. 1982a, *Ap. J. (Suppl.)*, **50**, 115.
 _____. 1982b, *Ap. J.*, **263**, 366.
 Brown, G. E. 1982, in *Supernovae: A Survey of Current Research*, ed. M. J. Rees and R. J. Stoneham (Dordrecht: Reidel), p. 13.
 Brown, G. E., Bethe, H. A., and Baym, G. 1982, *Nucl. Phys. A*, **375**, 481.
 Bruenn, S. W. 1975, *Ann. NY Acad. Sci.*, **262**, 80.
 Bruenn, S. W., Arnett, W. D., and Schramm, D. N. 1977, *Ap. J.*, **213**, 213.

- Bruenn, S. W., and Ballester, J. L. 1980, *Ap. Space Sci.*, **78**, 247.
- Bruenn, S. W., Buchler, J. R., and Yueh, W. 1978a, *Ap. Space Sci.*, **59**, 261.
- _____. 1978b, *Ap. J. (Letters)*, **221**, L83.
- Buchler, J. R. 1979, *J. Quant. Spectrosc. Rad. Transf.*, **22**, 293.
- Burrows, A., and Lattimer, J. M. 1983, *Ap. J.*, **270**, 735.
- Burrows, A., and Mazurek, T. J. 1982, *Ap. J.*, **259**, 330.
- Caster, J. I. 1972, *Ap. J.*, **178**, 779.
- Chandrasekhar, S. 1960, *Radiation Transfer* (New York: Dover).
- _____. 1964, *Ap. J.*, **140**, 417.
- _____. 1965, *Ap. J.*, **142**, 1488.
- Chevalier, R. A. 1976, *Ap. J.*, **207**, 872.
- Chiu, H. Y., and Stabler, R. C. 1961, *Phys. Rev.*, **122**, 1317.
- Clayton, D. D. 1968, *Principles of Stellar Evolution and Nucleosynthesis* (New York: McGraw-Hill).
- Colgate, S. A., and White, R. H. 1966, *Ap. J.*, **143**, 626.
- Cooperstein, J., Bethe, H. A., and Brown, G. E. 1984, *Nucl. Phys. A*, **429**, 527.
- Discus, D. A. 1972, *Phys. Rev. D*, **5**, 1412.
- Eder, G. 1968, *Nuclear Forces* (Cambridge: MIT Press).
- Epstein, R. I., and Pethick, C. J. 1981, *Ap. J.*, **243**, 1003.
- Falk, S. W. 1978, *Ap. J. (Letters)*, **225**, L133.
- Falk, S. W., and Arnett, W. D. 1973, *A. J. (Letters)*, **180**, L65.
- _____. 1977, *Ap. J. Suppl.*, **33**, 515.
- Fowler, W. A., and Hoyle, F. 1964, *Ap. J. Suppl.*, **91**, 201.
- Freedman, D. Z. 1974, *Phys. Rev. D*, **9**, 1389.
- Friedman, B., and Pandharipande, V. R. 1981, *Nucl. Phys. A*, **361**, 502.
- Fuller, G. M. 1982, *Ap. J.*, **252**, 741.
- Fuller, G. M., Fowler, W. A., and Newman, M. J. 1982, *Ap. J.*, **252**, 715.
- Goldreich, P., and Weber, S. V. 1980, *Ap. J.*, **238**, 991.
- Grasberg, E. K., Imshennik, V. S., and Nadyozhin, D. K. 1971, *Ap. Space Sci.*, **10**, 28.
- Grover, R., and Hardy, J. W. 1966, *Ap. J.*, **143**, 48.
- Hillebrandt, W. 1982a, *Astr. Ap.*, **110**, 63.
- _____. 1982b, in *Supernovae: A Survey of Current Research*, ed. M. J. Rees and R. J. Stoneham (Dordrecht: Reidel).
- _____. 1983, preprint.
- Hillebrandt, W., and Müller, E. 1981, *Astr. Ap.*, **103**, 147.
- Hoyle, F., and Fowler, W. A. 1960, *Ap. J.*, **132**, 565.
- Hung, P. Q., and Sakurai, J. J. 1981, *Ann. Rev. Nucl. Particle Sci.*, **31**, 375.
- Imshennik, V. S., and Chechetkin, V. M. 1971, *Sov. Astr.—AJ*, **14**, 747.
- Konopinski, E. J. 1966, *The Theory of Beta Radioactivity* (London: Oxford University Press).
- Lamb, D. Q., Lattimer, J. M., Pethick, C., and Ravenhall, D. G. 1978, *Phys. Rev. Letters*, **41**, 1623.
- _____. 1981, *Nucl. Phys. A*, **360**, 459.
- Lamb, D. Q., and Pethick, C. J. 1976, *Ap. J. (Letters)*, **209**, L77.
- Lattimer, J. M. 1981, *Ann. Rev. Nucl. Particle Sci.*, **31**, 537.
- Levermore, C. D., and Pomraning, G. C. 1981, *Ap. J.*, **248**, 321.
- Lindquist, R. W. 1966, *Ann. Phys.*, **37**, 478.
- Lund, C., and Wilson, J. R. 1980, Lawrence Livermore Lab. Rept. UCRL-84678.
- Marshak, R. E., and Ryan, C. P. 1969, *Theory of Weak Interactions in Particle Physics* (New York: Interscience).
- May, M. M., and White, R. H. 1967, *Meth. Comput. Phys.*, **7**, 219.
- Mazurek, T. J. 1975, *Ap. Space Sci.*, **35**, 117.
- _____. 1976, *Ap. J. (Letters)*, **207**, L87.
- _____. 1982, *Ap. J. (Letters)*, **259**, L13.
- Mazurek, T., Cooperstein, J., and Kahana, S. 1981, in *DUMAND-80*, ed. V. J. Stenger (Honolulu: University of Hawaii DUMAND Center), p. 142.
- _____. 1982, in *Supernovae: A Survey of Current Research*, ed. M. J. Rees and R. J. Stoneham (Dordrecht: Reidel).
- Mazurek, T. J., Lattimer, J. M., and Brown, G. E. 1979, *Ap. J.*, **238**, 139.
- Mihalas, D. 1970, *Stellar Atmospheres* (San Francisco: Freeman).
- Miyaji, S., Nomoto, K., Yokoi, K., and Sugimoto, D. 1980, *Pub. Astr. Soc. Japan*, **32**, 303.
- Nomoto, K. 1982, in *Supernovae: A Survey of Current Research*, ed. M. J. Rees and R. J. Stoneham (Dordrecht: Reidel).
- _____. 1983, preprint.
- Nomoto, K., Miyaji, S., Yokoi, K., and Sugimoto, D. 1979, *IAU Colloquium 53, White Dwarfs and Variable Degenerate Stars*, ed. H. M. Van Horn and V. Weidmann (Dordrecht: Reidel).
- Pomraning, G. C. 1973, *Radiation Hydrodynamics* (Oxford: Pergamon).
- Quigg, C. 1983, *Gauge Theories of the Strong, Weak, and Electromagnetic Interactions* (Reading, Mass.: Benjamin/Cummings).
- Salam, A. 1969, *Elementary Particle Theory*, ed. N. Svartholm (Stockholm: Almqvist & Wiksell).
- Sato, K. 1975a, *Progr. Theoret. Phys.*, **53**, 595.
- _____. 1975b, *Progr. Theoret. Phys.*, **54**, 1325.
- Schramm, D. N., and Arnett, W. D. 1975, *Ap. J.*, **198**, 629.
- Schwartz, R. A. 1967, *Ann. Phys.*, **43**, 42.
- Shalitin, D. 1978, *Ap. Space Sci.*, **53**, 55.
- Sparks, W. M., and Endal, A. S. 1980, *Ap. J.*, **237**, 130.
- Sugimoto, D., and Nomoto, K. 1980, *Space Sci. Rev.*, **25**, 155.
- Tubbs, D. L. 1979, *Ap. J.*, **231**, 846.
- Tubbs, D. L., and Schramm, D. N. 1975, *Ap. J.*, **201**, 467.
- Tubbs, D. L., Weaver, T. A., Bowers, R. L., Wilson, J. R., and Schramm, D. N. 1980, *Ap. J.*, **239**, 271.
- Van Riper, K. A. 1979, *Ap. J.*, **232**, 558.
- _____. 1982, *Ap. J.*, **257**, 793.
- Van Riper, K. A., and Lattimer, J. M. 1981, *Ap. J.*, **249**, 270.
- Weaver, T. A., Axelrod, T. S., and Woosley, S. E. 1980, in *Type I Supernovae*, ed. J. C. Wheeler (Austin: University of Texas Press).
- Weaver, T. A., and Woosley, S. E. 1980a, *Bull. AAS*, **11**, 724.
- _____. 1980b, *Ann. NY Acad. Sci.*, **336**, 335.
- Weaver, T. A., Woosley, S. E., and Fuller, G. M. 1982, *Bull. AAS*, **14**, 957.
- Weaver, T. A., Zimmerman, G. B., and Woosley, S. E. 1978, *Ap. J.*, **225**, 1021.
- Weinberg, S. 1967, *Phys. Rev. Letters*, **19**, 1264.
- _____. 1972, *Phys. Rev. D*, **5**, 1412.
- Wheeler, J. C. 1981, *Rept. Progr. Phys.*, **44**, 88.
- Wilson, J. R. 1971, *Ap. J.*, **186**, 1157.
- _____. 1974, *Phys. Rev. Letters*, **32**, 859.
- _____. 1976, *Varenna Lectures*.
- _____. 1978, *Proc. Internat. School of Physics Enrico Fermi, Course 65* (Amsterdam: North-Holland), p. 644.
- _____. 1980, *Ann. NY Acad. Sci.*, **336**, 358.
- _____. 1983 preprint.
- Wilson, J. R., Couch, R., Cochran, S., and LeBlanc, J. 1975, *Ann. NY Acad. Sci.*, **262**, 54.
- Wolff, R. 1983, thesis, Technische Universität, in preparation.
- Woosley, S. E., and Weaver, T. A. 1981, in *Essays on Nuclear Astrophysics*, ed. C. A. Barnes, D. D. Clayton, and D. N. Schramm (Cambridge: Cambridge University Press).
- _____. 1982, in *Supernovae: A Survey of Current Research*, ed. M. J. Rees and R. J. Stoneham (Dordrecht: Reidel).
- Woosley, S. E., Weaver, T. A., and Taam, R. E. 1980, in *Type I Supernovae*, ed. J. C. Wheeler (Austin: University of Texas Press), p. 69.
- Yahil, A. 1983, *Ap. J.*, **265**, 1047.
- Yahil, A., and Lattimer, J. M. 1982, in *Supernovae: A Survey of Current Research*, ed. M. J. Rees and R. J. Stoneham (Dordrecht: Reidel), p. 53.
- Yueh, W. R., and Buchler, J. R. 1976a, *Ap. Space Sci.*, **39**, 429.
- _____. 1976b, *Ap. Space Sci.*, **41**, 221.
- _____. 1977, *Ap. J.*, **217**, 565.

STEPHEN W. BRUENN: Physics Department, Florida Atlantic University, Boca Raton, FL 33431-3385